UNIVERSITY OF OKLAHOMA

GRADUATE COLLEGE

SATELLITE AND RADAR REMOTE SENSING OF TROPICAL CYCLONES TO QUANTIFY MICROPHYSICAL AND PRECIPITATION PROCESSES

A DISSERTATION

SUBMITTED TO THE GRADUATE FACULTY

in partial fulfillment of the requirements for the

Degree of

DOCTOR OF PHILOSOPHY

By

Noah Brauer

Norman, Oklahoma

2022

Downloaded from SHAREOK. Persistent Handle URL: https://hdl.handle.net/11244/336274

SATELLITE AND RADAR REMOTE SENSING OF TROPICAL CYCLONES TO QUANTIFY MICROPHYSICAL AND PRECIPITATION PROCESSES

A DISSERTATION APPROVED FOR THE

SCHOOL OF METEOROLOGY

BY THE COMMITTEE CONSISTING OF

Dr. Pierre E. Kirstetter, Chair

Dr. Jeffrey B. Basara, Co-Chair

Dr. Cameron R. Homeyer

Dr. Greg M. McFarquhar

Dr. J P. Gibson

© Copyright by Noah Brauer 2022

All Rights Reserved.

Acknowledgements

Oh...where do I even start? First, I would like to thank Dr.Pierre Kirstetter for being a fantastic advisor and mentor throughout my Ph.D. Pierre, you are an inspiration and I have always appreciated how much you care about me and the work that we do. Thank you for having confidence in me and for being a wonderful role model. Dr. Jeffrey Basara, thank you so much for bringing me to the University of Oklahoma, advising me throughout my entire graduate career, being an amazing colleague while teaching, and for being someone I can always come to for advice (both personal and professional). I cannot thank you enough. Dr.Cameron Homeyer, thank you for always providing useful input, for giving me radar data on very short notice for multiple studies, and for introducing me to the incredible world of cloud microphysics. Dr.Greg McFarquhar, I appreciate all the advice and scientific insight that you have provided. Thank you Dr. Phil Gibson for solidifying my love for field work and for providing a new perspective on environmental science. My entire committee has done so much for me throughout these few years and I will forever be grateful for their support and feedback.

I also want to thank my co-authors Dr. Ryann Wakefield, Dr.Addison Alford, Dr. Sean Waugh, Dr. Michael Biggerstaff, Dr. Marshall Shepherd, Dr. Jinwoong Yoo, Dr. Svetla Hristova-Veleva, and Dr. Simone Tanelli. Thank you all for providing such useful feedback and support, and for being crucial resources for my Ph.D. work. Addison, Sean, Mike, and I have deployed to 5 hurricanes together and doing field

work with them has been an invaluable experience and gave me a true appreciation for science.

Greg Jennrich, Tomer Burg, Maddy Howell, Taylor Grace, Jordan Christian, Eric Hunt, Jordan Laser, Trey Greenwood, Ollie Millin, David Nowicki, Alyssa Woodward, and Ty Dickinson (amongst many others), thank you all so much for being so supportive of me throughout my time in Norman. You made Norman feel like home during my graduate studies and I'm so thankful we have these memories together. I also want to thank Randy Chase for always being willing to discuss certain research ideas and for providing help and insight when needed. Randy has truly inspired my PhD research.

My family and friends back home, I could not have done this without you. I would like to thank my mother and father for being supportive of my passion for meteorology and education from day one. Thank you for not going crazy whenever I would obsess over thunderstorms and snow. My sister for always being there in difficult times, and my grandparents for providing moral support and delicious baked goods. I love you all so much. John Cassano, Keah Schuenemann, Sam Ng, and Scott Landolt, thank you for helping me get to where I am today and for the mentorship and friendship. Simon Degroot, Shen Tan, Minh Phan, Andrew Schwartz, Reid Hansen, Dalton Behringer, Audrey Eskrdige, Sam Loob, Daniel Lyon, Hannah Owen, Emily Mohr, Scott Noel, Chris Manlove and Nicole Manlove: You have been there for me throughout this entire experience (and beyond) and I am so happy to be close to you

all again. You made graduate school less painful.

Contents

1 Chapter 1: Introduction **1**

2 Chapter 2: The Inland Maintenance and Re-Intensification of Tropical Storm Bill (2015): Precipitation Microphysics **4**

2.1 Introduction 4

2.2 Data and Methods 9

2.2.1 Event Background 9

2.2.2 Polarimetric Radar Data 9

2.2.3 GPM Dual Frequency Precipitation Radar Data 13

2.2.4 Miscellaneous Data 15

2.3 Results 16

2.3.1 Near Landfall 16

2.3.2 TCMI1: Southern Oklahoma 17

2.3.3 TCMI2: Southern Missouri, Illinois 20

2.3.4 Dynamics 22

2.4 Discussion 24

2.5 Conclusions 27

3 Chapter 3: Hurricane Laura (2020): A Comparison of Drop Size Distribution Moments Using Ground and Radar Remote Sensing Retrieval Methods **42**

3.1 Introduction 42
3.2 Data and Methods 49
3.2.1 Event Background 49
3.3 Ground-Based Radar Observations 50
3.3.1 GPM Dual-Frequency Precipitation Radar 54
3.3.2 Portable In-Situ Precipitation Stations (PIPS) 56
3.4 Results 58
3.4.1 Ground Radar Observations 58
3.4.2 GPM DPR Retrievals 61
3.4.3 Disdrometer Observations 65
3.5 Discussion 67
3.6 Conclusions 72

4 Chapter 4: Precipitation Microphysics in Tropical Cyclones: A Global Perspective 89

4.1 Introduction 89
4.2 Data and Methods 94
4.2.1 IBTrACS and SHIPS 94
4.2.2 GPM DPR 94
4.2.3 ERA-5 96
4.3 Results 97

4.3.1 Large-Scale Environmental Influences on TC Structure and Precipitation Processes 97
4.3.2 Annulus Cases 99
4.3.3 Shear-Relative Analysis 102
4.4 Discussion 106
4.4.1 Limitations and Future Work 111
4.5 Conclusions 112

5 Conclusions **129**

5.1 Summary 129
5.2 Final Remarks and Future Work 131

List of Tables

1 Table with PIPS locations, and starting time 88

2 Cases for each type of analysis in each TC ocean basin 128

List of Figures

1 Hurricane Database (HURDAT2) Best Track plot of Tropical Storm Bill from 16-21 June, 2015. Each point is spaced apart in 6-hour time increments. The green box represents the location of TCMI1 from 1200-1800 UTC 17 June, and the black box represents the location of TCMI2 from 1200 UTC 19 June to 1200 UTC 20 June. 30

2 PRISM daily accumulated precipitation over Texas and Oklahoma from 16-17 June (a. and b.), total accumulated precipitation from 16-20 June (c.), daily accumulated precipitation over Missouri and Illinois from 19-20 June (d. and e.), and total accumulated precipitation from 16-20 June (f.). 31

3 Time-height curtains of Z_H (a), Z_{DR} (b), K_{DP} (c), ρ_{hv} (d), and drop size (e) near the landfall point over El Campo, TX on from 1200 UTC 16 June-0000 UTC 17 June, and images of 2 km Z_H at 1200 UTC and 1800 UTC 16 June. 32

4 Time-height curtains of Z_H (a), Z_{DR} (b), K_{DP} (c), ρ_{hv} (d), and drop size (e) during TCMI1 over Grady, OK on from 1200 UTC 17 June-0000 UTC 18 June, and images of 2 km Z_H at 1200 UTC and 1800 UTC 17 June. 33

5 Contoured Frequency By Altitude Diagrams (CFADs) of Z_H Z_{DR}, K_{DP}, and ρ_{hv} at El Campo, TX on 16 June (a), and Grady, OK on 17 June during TCMI1 (b). 34

6 GPM DPR along-track vertical profiles of $Z_M(Ku)$, D_M, and $log_{10}(N_W)$ at 0538 UTC (a) and 1454 UTC (b) on 17 June, 2015 over Texas. The dashed line represents the 0^oC isotherm. 35

7 Time-height curtains of Z_H (a), Z_{DR} (b), K_{DP} (c), ρ_{hv} (d), and drop size (e) during TCMI2 over Cape Girardeau, MO on from 1800 UTC 19 June-0000 UTC 20 June, and images of 2 km Z_H at 1800 UTC 19 June and 0000 UTC 20 June. 36

8 Time-height curtains of Z_H (a), Z_{DR} (b), K_{DP} (c), ρ_{hv} (d), and drop size (e) during TCMI2 over Cairo, IL on from 1800 UTC 19 June-0000 UTC 20 June, and images of 2 km Z_H at 1200 UTC and 1800 UTC 19 June. 36

9 Contoured Frequency By Altitude Diagrams (CFADs) of Z_H Z_{DR}, K_{DP}, and ρ_{hv} at Cape Girardeau, MO on 19 June (a), and Cairo, IL on 19 June (b) during TCMI 2. 37

10 GPM DPR near-surface reflectivity (a), GPM DPR along-track vertical profiles of $Z_M(Ku)$ (b), surface rainfall rate (c), D_M (d), $log_{10}(N_W)$ (e), and associated regions of stratiform and convective precipitation at 0436 UTC on 20 June, 2015 over Illinois (f). The dashed line represents the 0^oC isotherm. 38

11 Longitude-height cross-sections of potential vorticity (shaded) and potential temperature (contours) along 38^oN from 2100 UTC 19 June to 1200 UTC 20 June. 39

12 Longitude-height cross-sections of vertical velocity (shaded) and potential temperature (contours) along 34^oN from 1200-2100 UTC 17 June during TCMI1 (a), with snapshots of 2 km Z_H and cross-section locations (b). 40

13 Longitude-height cross-sections of vertical velocity (shaded) and potential temperature (contours) along 38^oN from 2100 UTC 19 June to 1200 UTC 20 June during TCMI2 (a), with snapshots of 2 km Z_H and cross-section locations (b). 41

14 Observed soundings from Springfield, MO from 1200 UTC on 18 June to 1200 UTC 19 June. 41

15 Z-Zdr Parameter Space developed by Kumjian et al. (2012) that uses vertical changes in Z_H and Z_{DR} within the warm cloud layer to identify dominant precipitation processes. Positive changes indicate values of Z_H and Z_{DR} increasing towards the surface below the melting layer. . 74

16 Raw image of 0.5^o Z_H at 0553 UTC 27 August, shortly before the KLCH WSR-88D went down. Overlaid are the locations of the 4 PIPS, SR1-P, and the KLCH WSR-88D. Additionally, HURDAT2 best track points are shown in magenta to illustrate the track of Laura (HURDAT). The 100 km and 250 km range rings are centered on the storm center at the time of the PPI. 75

17 PPIs of Z_H from SR1-P at 0230 UTC (a) and 0525 UTC (b) on 27 August during the times of both RHI composites in Figure 4. The black lines denote the locations of each RHI cross-section of 70 km. . 76

18 Time averaged mean Z_H, Z_{DR}, and ρ_{hv} from SR1-P at an azimuth angle of 160° from 0211-0259 UTC on 27 August (a) and at an azimuth angle of 220° at 0510-0541 UTC on 27 August (b). Precipitation processes are inferred from the change in Z_H and Z_{DR} towards the surface below the melting layer. 77

19 Columnar-vertical profiles (CVPs) of Z_H, Z_{DR}, ρ_{hv}, and K_{DP} from SR1-P from 0200-1000 UTC 27 August. Precipitation processes are inferred from the change in Z_H and Z_{DR} towards the surface below the melting layer, with increases towards the surface implying collision-coalescence. 78

20 GPM DPR overpass at 0301 UTC 27 August (pre-landfall) showing attenuation-corrected near surface Ku-band reflectivity and PIPSs locations (a), vertical profiles of Ku-band reflectivity (b), mean drop diameter (c), and normalized intercept parameter (d). Vertical cross-sections are taken along track from the star. The dashed black line represents the 0^oC isotherm. 79

21 GPM DPR overpass at 1246 UTC 27 August (post-landfall) showing attenuation-corrected near surface Ku-band reflectivity and PIPSs locations (a), vertical profiles of Ku-band reflectivity (b), mean drop diameter (c), and normalized intercept parameter (d). Vertical cross-sections are taken along track from the star. The dashed black line represents the 0^oC isotherm. 80

22 Along-track quantiles of KuPR at 0301 UTC 27 August pre-landfall (a) and 1246 UTC 27 August post-landfall (b). The dashed line represents the along-track mean 0^oC isotherm. 81

23 850-200 mb environmental wind shear and 200 mb streamlines from 1800 UTC 26 August to 1200 UTC 27 August. 82

24 Drop diameter and $log_{10}(N_T)$ from PIPS 1A (a), 2A (b), and 2B (c) from 2000 UTC 26 August to 1200 UTC 27 August. The red line represents the separation of the outer core from the inner core while the magenta line represents the time of the pre-landfall GPM DPR overpass (0301 UTC). 83

25 D_M from PIPS 1A (a), 2A (b), and 2B (c) from 2000 UTC 26 August to 1200 UTC 27 August. The red line represents the separation of the outer core from the inner core while the magenta line represents the time of the pre-landfall GPM DPR overpass (0301 UTC). The green cirles represent the near-surface value of D_M from the pre-landfall GPM DPR overpass. 84

26 $log_{10}(N_W)$ from PIPS 1A (a), 2A (b), and 2B (c) from 2000 UTC 26 August to 1200 UTC 27 August. The red line represents the separation of the outer core from the inner core while the magenta line represents the time of the pre-landfall GPM DPR overpass (0301 UTC). The green cirles represent the near-surface value of $log_{10}(N_W)$ from the pre-landfall GPM DPR overpass. 85

27 Z_H from PIPS 1A (a), 2A (b), and 2B (c) from 2000 UTC 26 August to 1200 UTC 27 August. The red line represents the separation of the outer core from the inner core while the magenta line represents the time of the pre-landfall GPM DPR overpass (0301 UTC). The green cirles represents the near-surface value of KuPR from the pre-landfall GPM DPR overpass. The thin red line indicates Z_H from SR1-P over the location of each corresponding PIPS. 86

28 Z_{DR} from PIPS 1A, 2A, and 2B from 2000 UTC 26 August to 1200 UTC 27 August. The red line represents the separation of the outer core from the inner core while the magenta line represents the time of the pre-landfall GPM DPR overpass (0301 UTC). The thin red line indicates Z_{DR} from SR1-P over the location of each corresponding PIPS. 87

29 Histograms of time differences between each GPM DPR overpass and the IBTrACS storm center point for cases with wind shear data available (Fig. 29a) and without wind shear data available (Fig. 29b). Only cases where the difference was < 0.5 hours were retained in this analysis. 115

30 Tropical cyclone locations corresponding to each GPM DPR overpass from 2014-2020. Only overpass match ups between 45^oS and 45^oN were obtained. Points over land were also omitted. 116

31 Seasonal composites of mean boreal winter (DJF) total integrated water vapor from 2014-2020 (a), and mean boreal summer (JJA) total integrated water vapor from 2014-2020 (b). 117

32 Seasonal composites of mean boreal winter (DJF) 850-200 mb vertical wind shear from 2014-2020 (a), and mean boreal summer (JJA) 850-200 mb vertical wind shear from 2014-2020 (b). 118

33 Probability density functions (PDFs) of vertical slopes of attenuation-corrected KuPR in the liquid phase in the eyewall (Fig. 33a) and in the inner core (Fig. 33b), PDFs of vertical slopes of uncorrected KuPR in the liquid phase in the eyewall (Fig. 33c) and in the inner core (Fig. 33d) across all 6 TC ocean basins. 119

34 Probability density functions (PDFs) of vertical slopes of attenuation-corrected KuPR in the ice phase in the eyewall (Fig. 34a) and in the inner core (Fig. 34b), PDFs of vertical slopes of uncorrected KuPR in the ice phase in the eyewall (Fig. 34c) and in the inner core (Fig. 34d) across all 6 TC ocean basins. 120

35 Probability density functions (PDFs) of vertical slopes of attenuation-corrected KuPR in the liquid phase for each shear-relative quadrant across each TC basin that the DPR sampled the eyewall region. . . . 121

36 Probability density functions (PDFs) of vertical slopes of attenuation-corrected KuPR in the liquid phase for each shear-relative quadrant across each TC basin that the DPR sampled the inner core region. . . 122

37 Probability density functions (PDFs) of vertical slopes of attenuation-corrected KuPR in the ice phase for each shear-relative quadrant across each TC basin that the DPR sampled the eyewall region. 123

38 Probability density functions (PDFs) of vertical slopes of attenuation-corrected KuPR in the ice phase for each shear-relative quadrant across each TC basin that the DPR sampled the inner core region. 124

39 Probability density functions (PDFs) of echo top heights for each shear-relative quadrant across each TC basin that the DPR sampled the inner core region. 125

40 Probability density functions (PDFs) of echo top heights for each shear-relative quadrant across each TC basin that the DPR sampled the eyewall region. 126

41 Near-surface attenuation corrected KuPR (Fig. 41a), echo top heights (km) (Fig. 41b), vertical slope of KuPR in the liquid phase (Fig. 41c), and vertical slope of KuPR in the ice phase (Fig. 41d). 127

42 Near-surface attenuation corrected KuPR for a TC with a compact eyewall and inner core region (Fig. 42a) and a TC with a broad eyewall and inner core region (Fig. 42b). The SHIPS 850-200 hPa shear vector is denoted by the arrow whereas the IBTrACS storm center is illustrated by the black dot. 128

Abstract

Precipitation microphysics in tropical cyclones (TCs) are often poorly represented in numerical simulations, which ultimately affects TC structure, evolution, and prediction. This provides a large incentive to better observe and understand the underlying microphysical processes in TCs in order to improve precipitation forecasts and improve warning operations. Recently, ground-based polarimetric radar observations have been able to capture the evolution and structure of precipitation in landfalling TCs in the United States, revealing numerous microphysical processes through the investigation of vertical profiles of dual-polarization radar variables. While ground radars are a useful tool for quantifying precipitation processes in TCs, they are unable to sample precipitation when TCs are over the open ocean. Therefore when ground radar networks are sparse or non-existent, space-borne radar can provide precipitation retrievals of TCs at snapshots in time. This is particularly useful for monitoring the evolution of precipitation in TCs prior to landfall. Specifically, this dissertation investigates precipitation microphysics in TCs using the NASA Global Precipitation Measurement (GPM) mission dual-frequency precipitation radar (DPR) on a global scale, and is complimented by polarimetric ground radar observations, disdrometer data, and reanalysis data when available.

1 Chapter 1: Introduction

This work seeks to address two major science questions and objectives that were listed in the National Academy of Sciences Decadal Survey (2017). First, this dissertation aims to quantify rates of precipitation and its phase worldwide at convective and orographic scales in order to capture flash flooding events, particularly in tropical cyclones (TCs) (science question H-1b). Further, the following research characterizes microphysical processes and interactions of hydrometeors by measuring the precipitation distribution and rate to within 5% (science question W-9a).

TCs play an important role in the Earth's water cycle and radiation budget (e.g., Gray 1968; Franco-Díaz et al. 2019; Smith and Toumi 2020) and are known to produce excessive precipitation when making landfall (e.g., Rappaport 2000; Brauer et al. 2020; Martinaitis et al. 2021). For this reason it is critical to not only understand the drivers of heavy precipitation in TCs, but also the underlying precipitation microphysics and processes as these are key towards estimating rainfall at the surface (e.g., Ulbrich and Atlas 2007; Carr et al. 2017; Porcacchia et al. 2019). Further, it is known that microphysics are often poorly represented in numerical simulations of TCs, therefore it is important to understand observations of precipitation in order to improve microphysical parameterization schemes (Hristova-Veleva et al. 2021).

Recently, the WSR-88D network has been upgraded with polarimetric radar capabilities which have been shown to be useful in cases of landfalling TCs as they provide observations at a high temporal resolution and give insight into microphysical and

preciptiation processes (e.g., Didlake and Kumjian 2017a; Didlake Jr. and Kumjian 2018; Brauer et al. 2020; Laurencin et al. 2020a; Homeyer et al. 2021a). Further, vertical profiles of polarimetric radar variables such as the horizontal radar reflectivity factor (Z_H) and differential reflectivity (Z_{DR}) can be investigated by looking at their vertical slopes to infer precipitation processes such as collision-coalescence (CC), drop breakup, evaporation, and size-sorting in different portions of TCs (e.g., Carr et al. 2017; Porcacchia et al. 2019; Brauer et al. 2022). As ground radars have limitations such as beam broadening with increasing range, coarse vertical sampling, and the inability to sample TCs over the open ocean, the NASA Global Precipitation Measurement (GPM) mission dual-frequency precipitation radar (DPR) is a useful supplemental remote sensing platform that can be used to sample precipitation in TCs.

The GPM DPR has the capability of sampling precipitation in TCs at snapshots in time and in areas where ground radar and disdrometer networks are sparse or non-existent (Hou et al. 2014; Skofronick-Jackson et al. 2017). Further, the DPR has a vertical resolution of 250 meters, making it more useful for sampling the vertical structure of precipitation compared to ground radars. For these reasons, the DPR is a useful platform for analyzing precipitation processes in TCs on a global scale.

Broadly speaking, the hypothesis of this dissertation is that precipitation and microphysical processes will vary in points in space and time in TCs on the storm-scale in addition to the global scale. Further, ground

radar observations and space-borne radar retrievals will be capable of capturing the evolution of cloud properties, which can be used to infer precipitation microphysical processes in TCs. This dissertation is structured as follows:

• Chapter 2 (Brauer et al. 2021) of this dissertation discusses the inland maintenance and re-intensification of Tropical Storm Bill (2015) through ground radar observations, GPM DPR retrievals, and reanalysis data to investigate primary precipitation microphysical processes and dynamics relating to TC structure such as potential vorticity and vertical velocity. The underlying hypothesis was that **precipitation processes such as CC and drop breakup were maintained as Bill tracked over anomalously moist soils.** This chapter is also the continuation of a study (Wakefield et al. 2021) that investigated the role of surface fluxes and boundary layer characteristics on the evolution of Tropical Storm Bill.

• Chapter 3 (Brauer et al. 2022) compares mobile ground radar observations, space-borne radar retrievals, and disdrometer observations collected in Hurricane Laura (2020) to quantify particle size distribution moments and precipitation processes at various points in time and space throughout the storm. The primary hypothesis of this study was that **precipitation processes and microphysical footprints will vary at different portions of the storm's evolution and that there will be differences between each remote sensing retrieval method**.

• In order to provide a robust analysis with a larger sample size, Chapter 4 involved constructing a global database of GPM DPR retrievals of TCs from 2014-2020 and investigated how vertical slopes of Ku-band reflectivity (KuPR) vary by shear-relative quadrant and distance from the storm center. Each distribution of KuPR profiles were then partitioned into different TC ocean basins to determine how precipitation and microphysical processes vary globally. Other features such as bright-band depth and echo top height were also analyzed. This work hypothesized that **inferred precipitation processes from slopes of vertical profiles of KuPR would vary by TC shear-relative quadrants, radial distance from the storm center, and by ocean basin due to global variability in total column integrated water vapor and 850-200 mb wind shear.**

2 Chapter 2: The Inland Maintenance and Re-Intensification of Tropical Storm Bill (2015): Precipitation Microphysics

2.1 Introduction

Landfalling TCs can produce significant destruction and mortality, and have been estimated to kill upwards of 500 million people since 1492 (Rappaport 2000). While

damaging winds pose a threat to life and property near the TC landfall point, freshwater flooding can result in human fatalities hundreds of kilometers inland (e.g., Rappaport 2000; Jarrell et al. 2001). Thus, it is important to understand the characteristics of excessive precipitation in landfalling TCs well away from coastal regions.

May and June 2015 produced unprecedented rainfall in portions of Oklahoma and Texas, including an all-time high rainfall total of 594 mm for the month of May at the Norman Mesonet site (e.g., Brock et al. 1995; McPherson et al. 2007; Duchon et al. 2017). As a result, catastrophic urban and river flooding occurred during this period due to excessive precipitation, runoff, and saturated soils, resulting in 11 fatalities. Tropical Storm Bill further contributed to the excessive precipitation event over the region as it tracked over Texas and Southern Oklahoma in June 2015.

Previous studies (e.g., Clark and Arritt 1995; Lynn et al. 1998) have shown the importance of soil moisture on generating deep convection through enhanced latent heat fluxes which serves to increase boundary layer moisture. The influence of soil moisture on local weather and climate extremes is most pronounced in continental regions characterized by a transition zone from humid to drier climates (e.g., Guo et al. 2006; Koster et al. 2006), such as the Southern Great Plains (SGP). In this region, evapotranspiration displays a greater sensitivity to changes in both soil moisture and atmospheric demand (e.g., Guo et al. 2006; Koster et al. 2011; Wei et al. 2015). The connection between these continental land-atmosphere feedbacks and TCs is not entirely obvious at first. However, observations of TC re-intensification over land have

recently given rise to the concept of the "Brown Ocean Effect", which hypothesizes that anomalously moist soils can mimic an oceanic surface by providing fluxes of heat and moisture to the TC (e.g., Emanuel et al. 2008; Andersen and Shepherd 2014a).

The first paper of this study (Wakefield et al. 2020) found that the brown ocean effect played a role in maintaining Tropical Storm Bill over land through above average latent heat fluxes which increases total precipitable water and vertically integrated relative humidity. The re-intensification of Tropical Storm Erin (2007) over Oklahoma has been attributed to this particular phenomenon (e.g., Arndt et al. 2009; Monteverdi and Edwards 2010; Evans et al. 2011; Kellner et al. 2011; Andersen and Shepherd 2014a). Nair et al. (2019) recently attributed the historic flooding in Louisiana associated with an unnamed tropical system to the "Brown Ocean Effect". TC maintenance and/or re-intensification events, otherwise known as TCMI events, have been observed globally (Andersen and Shepherd 2014a), and are typically associated with above normal latent heat flux in the 3-weeks prior to the TC's landfall.

Andersen and Shepherd (2014b) used a 900-600 mb thermal wind calculation to categorize landfalling TCs after progressing inland as having a warm core, neutral (hybrid), or cold core. From the 227 cases examined, 45 TCs were found to have re-intensified over land, primarily due to large positive heat fluxes over a warm and moist land surface. Other important factors that were found to be conducive to TCMI over land are weak deep-layer wind shear and a lack of a horizontal temperature gradient. While synoptic-scale features and land surface characteristics were found to dictate

TCMIs over land (e.g., Andersen and Shepherd 2014a; Yoo et al. 2020), the microphysical precipitation processes remain to be explored in these events. Specifically, the evolution and quantification of microphysical processes have yet to be systematically analyzed in cases of inland TC re-intensification or maintenance. Griffin et al. (2014) performed an in-depth ground-based polarimetric radar analysis of Tropical Storm Erin's re-intensification over central Oklahoma. Didlake and Kumjian (2017b) examined the interaction between storm asymmetries, vertical wind shear, and precipitation processes using polarimetric radar observations in Hurricane Arthur (2014), and found that vertical profiles of Z_H and Z_{DR} in the downshear half of the eyewall exhibited signatures associated with collision-coalescence. Feng and Bell (2019) performed a similar analysis in Hurricane Harvey (2017) and discussed size-sorting signatures in the eyewall as the maximum in K_{DP} and Z_H remained downwind from the maximum in Z_{DR}. Polarimetric radar observations from the WSR-88D network (Crum and Alberty 1993) provide additional insight into the evolution of precipitation processes, and for example can be used to diagnose the extent of the low-echo centroid, warm rain processes (i.e., collision-coalescence and drop breakup) that are expected in a TC environment (e.g., Ryzhkov et al. 2005c; Vitale and Ryan 2013; Kumjian and Prat 2014; Didlake and Kumjian 2017b).

Polarimetric radar observations at essentially unattenuated frequencies provide physical insight into precipitation processes at a high temporal resolution (e.g., Medlin et al. 2007; Didlake Jr. and Kumjian 2018), and can provide valuable insight into pre-

cipitation microphysics and drop size distribution characteristics that can ultimately improve the accuracy of quantitative precipitation estimation (e.g., Seliga and Bringi 1976; Herzegh and Jameson 1992; Zrnić and Ryzhkov 1996; Ryzhkov et al. 2005b; Giangrande and Ryzhkov 2008; Cifelli et al. 2011). However, ground-radars are often limited in sampling the vertical dimension that is critical for precipitation microphysics, due to discrete elevation angles and increasing beam elevation with range, combined with beam broadening and non-uniform beam filling (Kirstetter et al. 2013). Other limitations include calibration uncertainty (e.g., Gorgucci et al. 1992; Bechini et al. 2008), the presence of mixed-phase precipitation (e.g., Gray et al. 2006; Kumjian 2013a), and partial beam filling (e.g., Ryzhkov 2007; Zhang et al. 2013). On the other hand, satellite-based radars provide a more regular and a finer vertical sampling as well as calibration stability, but they operate at attenuated frequencies. Thus, it is useful to jointly examine ground-based radar observations and satellite-borne radar retrievals to quantify microphysical processes (e.g., Smalley et al. 2017; Porcacchia et al. 2019). The synergy between ground-based radar observations and space-borne radar retrievals provide a novel framework for identifying instances of TCMI in Tropical Storm Bill by identifying profiles of collision-coalescence processes hundreds of kilometers inland from the landfall point. The objective of this study is to identify whether warm rain processes that are commonly observed in TCs existed well away from the landfall point during the periods of TCMI.

2.2 Data and Methods

2.2.1 Event Background

Tropical Storm Bill made landfall at 1645 UTC 16 June 2015 near Matagorda Island, TX with an estimated maximum sustained wind speed of 26 ms^{-1} (50 knots) and a minimum central pressure of 997 mb. Bill then progressed north over north Texas and into southeastern Oklahoma while maintaining tropical depression status before being classified as an extratropical cyclone as it moved east into Arkansas, Missouri, and Kentucky (Fig.1). Bill produced three distinct maxima in rainfall, with accumulations near the landfall point over south Texas near 300 mm, and a secondary maximum over north Texas and southern Oklahoma of 400 mm, and a third maximum over southern Illinois of 225 mm (Fig.2). From hereon, TCMI1 will refer to the period of tropical cyclone maintenance over north Texas and southern Oklahoma from 1200-1800 UTC 17 June, and TCMI2 will refer to the re-intensification of Bill over southern Missouri, Illinois, and western Kentucky from 1200 UTC 19 June to 1200 UTC 20 June (Wakefield et al. 2020).

2.2.2 Polarimetric Radar Data

Tropical Storm Bill offers the first opportunity to examine TCMI over land and the entire microphysical evolution of the cyclone using polarimetric radar observations since the WSR-88D network was upgraded with dual-polarization technology in 2010. Thus, Tropical Storm Erin (2007) was not captured due to a limited radar

network that contained dual-polarization capabilities. This study uses Level-II WSR-88D data from the National Centers for Environmental Information (NOAA National Weather Service (NWS) Radar Operations Center 1991), which are then processed using the Gridded NEXRAD WSR-88D (GridRad) software (Bowman and Homeyer 2017). These data have a temporal resolution of 5 minutes and have an azimuthal resolution of 0.5^o for the lowest four elevation angles, and a 1° azimuthal resolution for other angles (Crum and Alberty 1993).

The polarimetric radar variables that are analyzed include the horizontal reflectivity factor (Z_H), differential reflectivity (Z_{DR}), specific differential phase (K_{DP}), and the co-polar correlation coefficient (ρ_{hv}). Z_H is proportional to the integration of the diameter of scatterers raised to the sixth power and provides information regarding the size and concentration of precipitation-sized hydrometeors that satisfy the Rayleigh regime (e.g., Austin 1987; Herzegh and Jameson 1992; Zrnic and Ryzhkov 1999; Vitale and Ryan 2013). Z_{DR} is defined as the difference between the horizontal and vertical reflectivity factors, and provides information about the size, shape, and orientation of hydrometeors (e.g., Seliga and Bringi 1976; Herzegh and Jameson 1992). Z_{DR} observations can be biased if mixed-phase precipitation is present within a resolution volume which can lead to non-uniform beam filling (e.g., Bringi et al. 1990; Testud et al. 2000; Ryzhkov 2007; Giangrande and Ryzhkov 2008), or if the radar is miscalibrated (e.g., Gorgucci et al. 1992; Bechini et al. 2008). K_{DP} is influenced by the number concentration of hydrometeors within a volume (e.g., Kumjian

2013b). This is because large drops are oblate spheroids, therefore the horizontal polarization will encounter more of a phase shift compared to the vertical polarization, resulting in positive K_{DP} (e.g., Herzegh and Jameson 1992; Zrnic and Ryzhkov 1999; Ryzhkov et al. 2005c; Kumjian 2013a). Thus, one advantage of using K_{DP} is that it is independent of radar calibration and is immune to propagation attenuation, which makes it useful for estimating heavy rainfall (e.g., Seliga and Bringi 1978; Jameson 1985; Wang and Chandrasekar 2009). ρ_{hv} is a measure of the similarity of scatters in a resolution volume (e.g., Herzegh and Jameson 1992; Zrnic and Ryzhkov 1999; Ryzhkov et al. 2005c; Ryzhkov et al. 2005b; Kumjian 2013a). A homogeneous particle size distribution will yield a ρ_{hv} close to 1, whereas mixed-phased precipitation will result in a ρ_{hv} <0.9 (e.g., Herzegh and Jameson 1992; Zrnic and Ryzhkov 1999; Ryzhkov et al. 2005c; Ryzhkov et al. 2005b; Kumjian 2013a).

Rainfall in TCs are characterized by a larger concentration of smaller drops (e.g., Cao et al. 2008; Brauer et al. 2020; DeHart and Bell 2020). Thus, Z_H tends to be lower than that of rainfall in the mid-latitudes due to the dependence of Z_H on drop size (e.g., Austin 1987; Herzegh and Jameson 1992; Zrnic and Ryzhkov 1999). Further, due to the large number concentration of small drops found in TCs (e.g., Squires 1956; Ulbrich and Atlas 2007; Xu et al. 2008), Z_{DR} tends to range from 0-1 dB and K_{DP} tends to be positive (e.g., Brown et al. 2016; Didlake and Kumjian 2017b). In terms of vertical structure, the warm rain events associated with TCs that are characterized by the aforementioned polarimetric radar signatures are

typically dominated by collision-coalescence (CC) below the -10^oC isotherm because supercooled liquid water can still contribute to drop growth via the CC mechanism (e.g., Vitale and Ryan 2013; Schroeder et al. 2016). Signatures of CC below the -10^oC isotherm are identified by Z_H and Z_{DR} increasing towards the surface (e.g., Xu et al. 2008; Kumjian and Prat 2014; Carr et al. 2017; Porcacchia et al. 2019).

Time-height curtains of the polarimetric radar variables were plotted on from 1200 UTC 16 June to 0000 UTC 17 June near the landfall point at El Campo, TX (29.20^oN, -96.27^oW) and from 1200 UTC 17 June to 0000 UTC 18 June approximately 600 km inland at Grady, OK (35.05^oN, -97.87^oW) using a 5-point spatial mean surrounding the point of interest, similar to the quasi-vertical profile methodology in Ryzhkov et al. (2016). Additionally, vertical profiles of drop size were plotted to identify regions of drop growth and CC below the -10^oC isotherm. To estimate drop size, a Z_{DR} and K_{DP}-weighted relationship for tropical rainfall was used (Gorgucci et al. 2002) and is expressed in Equation 1. An identical framework was used to plot time-height curtains from 1800-0000 UTC 19-20 June over Cape Girardeau, MO (37.30^oN, -89.53^oW) and 1200-0000 UTC 19-20 June over Cairo, IL (37.00^oN, -89.18^oW) to gain insight into dominant microphysical processes during TCMI2.

$$\hat{D}_o = 1.155(K_{DP})^{0.076}(Z_{DR})^{1.164} \tag{1}$$

Contoured Frequency by Altitude Diagrams (CFADs) were plotted at each of the four locations using the ground-based radar observations of Z_H, Z_{DR}, K_{DP}, and

ρ_{hv}. Histograms were calculated at each level of constant altitude and plotted on a reflectivity versus height grid, with only values of Z_H, Z_{DR}, and K_{DP} where ρ_{hv} >0.97 were retained.

2.2.3 GPM Dual Frequency Precipitation Radar Data

The Global Precipitation Measurements (GPM) mission was launched in 2014 as a successor to the Tropical Rainfall Measurement Mission (TRMM) which ended in 2015 (e.g., Hou et al. 2014; Skofronick-Jackson et al. 2017). Onboard the GPM core observatory is the active dual-frequency precipitation radar (DPR). The GPM DPR is generally well-calibrated, has a higher sensitivity than S-band radars such as the WSR-88D network, and can provide snapshots of vertical profiles of reflectivity at a high vertical resolution and a low temporal resolution (e.g., Kozu et al. 2001; Hou et al. 2014). The GPM DPR is also capable of estimating precipitation at the surface when rainfall rates exceed 0.5 mm $hour^{-1}$ (e.g., Kozu et al. 2001; Hou et al. 2014). Although the GPM DPR is specifically prone to attenuation, it allows for a complementary source of identification and quantification of precipitation processes in addition to the ground-based radar network.

Alternatively, the GPM DPR operates at both Ku and Ka bands (13.6 GHz), which allows for the detection of lighter rainfall and ice hydrometeors due to the higher sensitivity of the Ka-band (12 dBZ). This is particularly useful for precipitation estimation at higher latitudes where frozen precipitation and stratiform systems are

more common (e.g., Skofronick-Jackson et al. 2017; Porcacchia et al. 2019). The GPM DPR has a horizontal resolution of 5 km and a vertical resolution of 250 m. In 2015, the swath widths were 245 km at Ku-band and 120 km at Ka-band (e.g., Hou et al. 2014; Skofronick-Jackson et al. 2017).

The GPM DPR alogirthm interprets the radar signal and estimates drop size distribution moments such as the mass-weighted mean drop diameter (D_M) and the generalizaed intercept parameter ($log_{10}(N_W)$), which is directly related to the number concentration of drops (GPM DPR Algorithm Theoretical Basis Document (ATBD)). These quantities are estimated assuming a gamma distribution function shown in equation (2), and computes D_M using the equation (3), where N_m is the corresponding scale factor and μ is the shape factor (Iguchi et al. 2018). The precipitation category algorithm identifies the presence of a bright-band, which is a signature in stratiform precipitation, and is used to partition areas into stratiform, convective, and other precipitation categories. More information regarding the algorithms used to calculate D_M and $log_{10}(N_W)$, and precipitation category can be found: (`https://gpm.nasa.gov/sites/default/files/document_files/ATBD_DPR_201811_with_Appendix3b_0.pdf`). Further, the 0^oC isotherm was also extracted from the GPM DPR and was plotted on the along-track cross-sections to quantify the melting layer height.

$$N(D) = N_m D^{\mu} exp\left[-\frac{(4+\mu)D}{D_M}\right] \tag{2}$$

$$D_M = \frac{\int D^4 N(D) dD}{\int D^3 N(D) dD} \tag{3}$$

Two GPM overpasses occurred over Texas and Oklahoma on 17 June at 0538 UTC and 1454 UTC as Tropical Storm Bill progressed inland over the region. Along-track vertical profiles of attenuation-corrected reflectivity at Ku-band were extracted through the inner core of Bill to identify regions of CC below the melting level. Regions of CC were identified in regions where reflectivity increases towards the surface below the melting level, which indicates drop growth and a resulting increase in reflectivity (Porcacchia et al. 2019). This reflectivity enhancement can also be caused by other factors such as the the height of the melting layer and the environmental lapse rate (Grams et al. 2014). Vertical profiles of D_M and $log_{10}(N_W)$ were also examined along the same ray to quantify drop size and drop number concentration variation with height. An additional GPM overpass occurred over southern Illinois at 0436 UTC on 20 June which provided an additional opportunity to quantify the extent of warm rain processes and TCMI as Bill progressed inland.

2.2.4 Miscellaneous Data

The Hurricane Database (HURDAT2) best-track data was used to plot the track of Tropical Storm Bill from 16-21 June, 2015 (Science Applications International Corporation and National Hurricane Center 1993). The ECMWF ERA-5 dataset has a horizontal grid spacing 31 km, 137 vertical levels, and a 3 hour temporal resolution

(Hersbach et al. 2019a), and was used to generate longitude-height cross-sections of potential vorticity, potential temperature, and vertical velocity during both periods of the TCMIs (i.e., TCMI1 and TCMI2). The Parameter-elevation Regressions on Independent Model (PRISM; Daly et al. 1994) which uses a 4 km grid resolution was used for daily precipitation accumulation from 16-20 June over Oklahoma and Texas. Additionally, the University of Wyoming sounding database was used to plot skew-T-log-P diagrams using MetPy plotting software (May et al. 2008 - 2017) at Springfield, Misourri from 1200 UTC on 18 June to 1200 UTC on 19 June.

2.3 Results

2.3.1 Near Landfall

Figure 3 displays vertical profiles of Z_H, Z_{DR}, K_{DP}, ρ_{hv}, and drop size on 16 June over El Campo, TX as Tropical Storm Bill made landfall. Because the ρ_{hv} field provides information regarding hydrometeor diversity, regions of reduced ρ_{hv} can be used to detect the melting layer (e.g., Herzegh and Jameson 1992; Zrnic and Ryzhkov 1999; Ryzhkov et al. 2005c; Ryzhkov et al. 2005b; Kumjian 2013a). In this case the melting layer was located between 4.5-5 km, which is consistent with polarimetric radar observations of other landfalling tropical cyclones such as Hurricane Harvey in 2017 (Brauer et al. 2020). Values of Z_H ranged from 25-45 dBZ in the liquid phase after 1500 UTC, with the highest values occurring after 2000 UTC. Z_{DR} of 1-1.5 dB existed from 1500-1700 UTC, implying a slightly larger drop size when compared to

the values of Z_{DR} of 0.5-1 dB that were observed later in the day after 1800 UTC. From the same 1500-1700 UTC period, values of K_{DP} were less than 0.25 degrees/km, whereas later in the day values ranged from 0.25-0.5 degrees/km. When combining the Z_H and Z_{DR} observations with K_{DP}, it can be seen that a small number concentration of larger drops existed from 1500-1700 UTC, whereas after 2000 UTC, there was a larger number concentration of smaller drops, consistent with tropical rainfall driven by CC (e.g., Squires 1956; Ulbrich and Atlas 2007; Carr et al. 2017). While the drop size appears to have increased towards the surface throughout the entire period (consistent with CC), the largest increase in drop size occurred after 2100 UTC on 16 June.

2.3.2 TCMI1: Southern Oklahoma

After Tropical Storm Bill progressed inland across north Texas and southern Oklahoma, it maintained its tropical precipitation characteristics. Figure 4 displays time-height curtains of the polarimetric radar variables and drop size at Grady, OK, which is near the time and location of TCMI1. The drop size was similar to that over El Campo, with values of Z_{DR} ranging from 1-1.5 dB in the liquid phase after 1800 UTC, and smaller values before this time. Similarly, values of K_{DP} of 0-0.25 degrees/km for the majority of the period, with higher values close to 0.5 degrees/km around 2200 UTC. At this time, Z_{DR} values were largest and Z_H was approximately 45 dBZ, implying that convection was responsible for the larger number concentration

of larger drops. The ρ_{hv} field suggests that the melting layer height decreased slightly from the previous day over El Campo, ranging from 3.5-4.5 km, with an upward displacement during the period of convection at approximately 2200 UTC. This may be due to stronger updrafts inducing latent heat release which subsequently increased the height of the 0^oC isotherm. The drop size profile over Grady was similar to that over El Campo, with drop size that increased towards the surface below the melting layer, indicative of CC and warm rain. This can also be seen via Figure 5 which shows that the vertical distributions of Z_H and Z_{DR} over El Campo and Grady were consistent with low-echo centroid precipitation systems and are characterized by the majority of reflectivity remaining within the warm cloud layer (e.g., Vitale and Ryan 2013; Schroeder et al. 2016). Similarly, Z_{DR} also increased towards the surface at both locations below the melting layer which is indicative of CC. The Z_{DR} distribution was also shifted towards values between 0-1 dB, implying a small mean drop size at El Campo and Grady (e.g., Squires 1956; Ulbrich and Atlas 2007; Carr et al. 2017) Figure 5 also illustrates the frequency of K_{DP} and ρ_{hv} values with height at the same two locations. K_{DP} values from 0-0.5 degrees/km occurred below the melting layer at El Campo between 30-40 different radar scans, indicating a large concentration of small drops (e.g., Brown et al. 2016; Didlake and Kumjian 2017b; Brauer et al. 2020). Lastly, the high frequency of ρ_{hv} <0.98 between 4.5-5.5 km ASL implies mixed-phase precipitation and the approximate location of the melting layer.

Figure 6 shows along-track vertical profiles of reflectivity at Ku-band from the

GPM DPR at 0538 UTC and 1454 UTC on 17 June. Although no additional overpass was available further north and east over Oklahoma, the 1454 UTC overpass provides a sense of the evolution of the reflectivity field as Bill progressed inland post-landfall. The DPR retrievals confirm the findings with the ground-based polarimetric radar observations. At 0538 UTC, a bright-band signature was evident at approximately 4.5-5 km, which is indicative of a melting layer at this altitude and is consistent with the 0^oC isotherm that was extracted from the GPM DPR. Below this level, the reflectivity increased towards the surface consistent with CC occurring within the warm cloud layer. Further, the retrieved D_M generally increases towards the surface, consistent with Porcacchia et al. (2019). As Bill tracked inland over north central Texas, the melting level was located slightly lower near 4.5 km, however there were upward displacements evident in the melting layer collocated with convection and associated values of reflectivity near 50 dBZ. Similarly, reflectivity predominantly increased below the melting layer, implying the maintenance of CC-dominant precipitation after Bill progressed hundreds of kilometers inland from the landfall point. Mean drop sizes (D_M) ranged from 0.75-1.5 mm, with higher values of 2 mm in regions of convection, Such observations were consistent with larger values seen in convection in other TCs such as Hurricane Harvey (2017) (Brauer et al. 2020; DeHart and Bell 2020). Finally, high drop number concentrations ($log_{10}(N_W)$) between 3-5 mm m^{-3} occurred during both times, with the highest values occurring in convective cores.

2.3.3 TCMI2: Southern Missouri, Illinois

As Bill continued to move north and east over southern Missouri, Illinois, and Kentucky from 19-20 June, the second TCMI occurred (TCMI2) at approximately 0000 UTC 20 June. Figures 7 and 8 show time-height curtains of Z_H, Z_{DR}, K_{DP}, ρ_{hv}, and drop size from the WSR-88D network at Cape Girardeau, MO and Cairo, IL on 19 June, respectively. Z_H values at the surface ranged from 30-40 dBZ after 2100 UTC at Cape Girardeau, with slightly lower values of 25-35 dBZ at Cairo, with distinctive bursts of weak convection after 1200 UTC, which explains the gaps in meteorological scatterers as $\rho_{hv} \leq 0.9$. Values of Z_{DR} were considerably lower than TCMI1, with values ranging from 0-1 dB at Cape Girardeau and 0-0.5 dB at Cairo, compared to 0.5-1.5 dB at El Campo and Grady. These lower values of Z_{DR} translate to a smaller drop size (e.g., Brown et al. 2016; Didlake and Kumjian 2017b) and were likely due to CC or a balance between CC and drop breakup, as expected in a tropical environment (e.g., Kumjian and Prat 2014; Didlake and Kumjian 2017b; Brauer et al. 2020). Additionally, signatures with an enhancement in hydrometeor number concentration in areas of weak convection (K_{DP} values near 0.25 degrees/km) occurred after 2100 UTC at both Cape Girardeau and Cairo. The vertical profiles of ρ_{hv} indicated that the melting layer height ranged from 4.0-5.5 km at both locations, and was located higher in altitude than Grady, OK.

Figure 9 illustrates the frequency of Z_H, Z_{DR}, K_{DP}, and ρ_{hv} with height at Cape Girardeau and Cairo to provide information regarding the dominant precipitation

processes during TCMI2. From the framework used in Kumjian and Prat (2014), Carr et al. (2017), and Porcacchia et al. (2019), Z_H increased towards the surface while Z_{DR} decreased towards the surface below the melting layer at both locations. Such results indicate size-sorting and evaporation, which may be due to enhanced vertical wind shear, leading to more dry air entrainment into the core of Bill, which is known to disrupt the structure of tropical cyclones (e.g., Gray 1968; Knaff et al. 2004; Hanley et al. 2001; Corbosiero and Molinari 2002). Although size-sorting and evaporation were likely the dominant processes, the drop size distribution was still skewed towards a smaller drop size as Z_{DR} remained below 1 dB at both locations for the majority of the event. Similarly, echo tops associated with the weak convection were below 12 km ASL, and similar features are known to produce the most extreme rainfall rates rather than deep convection with high values of Z_H(Hamada et al. 2015). There were also instances where locations saw an enhancement in drop concentration as K_{DP} between 0.25-0.5 degrees/km were observed.

Although ground-based radar observations show evidence of size-sorting and evaporation being the dominant processes, retrievals from the GPM DPR during an overpass at 0436 UTC 20 June show evidence of CC or a balance between CC and drop breakup below the melting layer (Fig. 10). The melting layer was identified between 4 and 5 km on the cross-section of Ku-band reflectivity and denoted by the enhancement of reflectivity due to melting hydrometeors. Further, the 0^oC isotherm was also located at 5 km, indicating a deep warm cloud layer. Below this level, reflectivity

increased from 25 dBZ to 35 dBZ at an along-track distance of 100 km, which is a signal of CC or a CC-breakup balance (Fig. 10b). D_M also increased from 0.75 to 1.2 mm at this location, with a larger mean drop size ranging from 1.25-1.75 mm within the weak convection (Fig. 10c). The vertical profiles of $log_{10}(N_W)$ show a drop concentration of 4.5 mm m^{-3} in the aforementioned region of CC, with slightly lower concentrations of 3.5-4.0 mm m^{-3} in the region of weak convection (Fig. 10d). The GPM DPR estimated a rainfall rate of 5-10 mm $hour^{-1}$ in the stratiform precipitation regions and enhanced rainfall rates of 20-35 mm $hour^{-1}$ in the embedded regions of weak convection (Fig. 10e). Lastly, Figure 10f shows regions of convection embedded in a broader region of stratiform precipitation. The aforementioned bright-band signature is likely a result of an area of stratiform precipitation within areas of weak convection.

2.3.4 Dynamics

While Bill certainly maintained tropical rainfall characteristics during TCMI2 over Southern Missouri and Illinois, the dynamics associated with Bill were investigated to determine how the large scale structure evolved during the re-intensification period. The primary feature of TCs is the presence of a low-level potential vorticity (PV) anomaly due to large amounts of latent heat release in convection (e.g., Möller and Smith 1994; Möller and Montgomery 2000; Trenberth and Fasullo 2007). This PV anomaly in TCs differs from extratropical cyclones, in which positive PV anomalies

are typically found in the upper troposphere (e.g., Hoskins et al. 1985; Hoskins 2006). Figure 11 shows longitude-height cross-sections of PV and potential temperature at a constant latitude of 38^oN using the ERA-5 data from 2100 UTC 19 June to 1200 UTC 20 June during TCMI2 over Southern Illinois and Kentucky. Before the onset of TCMI2, the positive PV anomaly existed in the mid troposphere between 600-400 hPa, with a gradual lowering and intensification of the positive PV anomaly analyzed by 0300 UTC 20 June. By 0600 UTC 20 June, the positive PV anomaly was located in the lower-troposphere between 900-800 hPa, characteristic of low-level positive PV anomalies that are typically found in TCs.

Longitude-height cross-sections of vertical velocity and potential temperature were also plotted using the ERA-5 data along a constant latitude of 34^oN from 1200-2100 UTC 17 June (Fig. 12) during TCMI1, and along a constant latitude of 38^oN from 2100 UTC 19 June to 1200 UTC 20 June (Fig. 13) during TCMI2. Maximum ascent rates of 3 Pa s^{-1} occurred near 600 hPa during TCMI1, whereas maximum ascent rates were considerably stronger during TCMI2, nearing values of 5 Pa s^{-1}. Vertical velocity can be related to convective available potential energy (CAPE) (e.g., List and Lozowski 1970; Blanchard 1998), and the vertical distribution of CAPE can be directly related to updraft speed. Moist adiabatic profiles that are often frequently observed in tropical environments are characterized by "skinny" CAPE profiles and are indicative of slow ascent rates (e.g., Davis 2001; Jessup and DeGaetano 2008; Vitale and Ryan 2013; Schroeder et al. 2016), whereas "fat" CAPE profiles are associated with stronger

updraft speeds and are more common in the midlatitudes. These weaker ascent rates are known to increase in-cloud residence time of hydrometeors, allowing for more efficient growth via CC (e.g., Vitale and Ryan 2013; Schroeder et al. 2016). In the case of Bill during TCMI1 and TCMI2, the magnitude of ascent was considerably less than vertical velocities captured in mid-latitude convection by ERA-5, which could be as high as 15 Pas^{-1} as was seen in a mid-latitude mesoscale convective system prior to Bill over the same region. The combination of low-echo centroid precipitation, shallow echo tops, and weak ascent rates further illustrates that Bill maintained tropical characteristics inland over southern Oklahoma, Missouri, southern Illinois, and Kentucky. Figure 14 shows observed soundings at Springfield, Missouri from 1200 UTC on 18 August to 1200 UTC on 19 August, which displays deep, moist adiabatic profiles and associated "skinny" CAPE which characterized the environment of Bill as it progressed northeast over Missouri and Kentucky. It can also be seen that there is considerable speed and directional shear at all three times, perhaps explaining the dominant presence of size-sorting and evaporation as Bill moved over this region.

2.4 Discussion

Tropical cyclones that maintain their structure over land can cause flooding and damaging winds hundreds of kilometers from the landfall point (e.g., Arndt et al. 2009; Andersen and Shepherd 2014b). Tropical Storm Bill (2015) experienced two distinct TCMI events over (1) southern Oklahoma and (2) Missouri, southern Illinois,

and Kentucky as it produced upwards of 400 mm of precipitation over this region from 16-20 June (Fig. 1). An important aspect of the inland maintenance of warm cloud microphysics and precipitation associated with tropical rainfall is that they are highly efficient processes to convert tropospheric water vapor to precipitation (i.e., precipitation efficiency). Further, these precipitation systems have a deep warm cloud layer (e.g., Davis 2001; Vitale and Ryan 2013; Schroeder et al. 2016; Brauer et al. 2020) dominated by CC or a CC-drop breakup balance and are known to account for excessive precipitation events in the midlatitudes (e.g., Hisham Mohd Anip and Market 2007;Carr et al. 2017; Porcacchia et al. 2019). A novel aspect of TC Bill is that its TCMIs occurred during a period of available polarimetric radar observations from ground-based radars along with observations from the newly launched GPM DPR in 2014 (e.g., Hou et al. 2014; Skofronick-Jackson et al. 2017). Such datasets allowed for a more in-depth analysis and quantification of precipitation processes during the TCMI events that were not possible with prior events. These observational datasets can further benefit and improve the numerical modeling of landfalling TCs since, compared to radiation and PBL/surface schemes, microphysics schemes play the more critical role in the numerical model simulations of TCMIs (Yoo et al. 2020). Yoo et al. (2020) found that the TCMI of TC Kelvin was driven by moisture transport from the intertropical convergence zone, rather than latent heat fluxes from coupling to from warm, sandy soils. Thus, the inferred precipitation microphysics from the polarimetric radar observations and GPM DPR retrievals can be used to adjust the microphysical

parameterization schemes accordingly in numerical simulations of TCMI to deliver model output that is more consistent with observations, and determine the role of precipitation microphysics of TCMI.

While inland over southern Oklahoma, Bill maintained dual-polarization radar signatures consistent with tropical rainfall and characterized by a large number concentration of small drops (Fig.4) (e.g., Squires 1956; Ulbrich and Atlas 2007; Xu et al. 2008; Brauer et al. 2020). Z_{DR} of 0.5-1.25 dB in addition to K_{DP} >0.5 degrees/km allows the classification of tropical rainfall, whereas Z_H alone is more sensitive to hydrometeor size (e.g., Austin 1987; Herzegh and Jameson 1992; Zrnic and Ryzhkov 1999; Kumjian 2013a). GPM DPR observations (Fig.6) during TCMI1 also showed an increase in drop size and Ku-band reflectivity below the melting layer, which is consistent with CC-dominant precipitation (e.g., Huang and Chen 2019; Porcacchia et al. 2019).

As Bill progressed inland over Missouri, southern Illinois, and Kentucky on 19-20 June, signatures of tropical precipitation were maintained during TCMI2, but were not as pronounced as when Bill was closer to the landfall point during TCMI1. Figure 9 illustrates signatures associated with evaporation and size-sorting as Z_H increased towards the surface and Z_{DR} decreased towards the surface (e.g., Kumjian and Prat 2014; Carr et al. 2017; Porcacchia et al. 2019). However, the values of Z_{DR} ranging from 0.5-1 dB, and K_{DP} as high as 0.25 degrees/km (Fig 7, Fig. 8) implies tropical rainfall characteristics similar to TCMI1 and shortly after the landfall point

near El Campo, TX. The GPM DPR overpass over southern Illinois at 0436 UTC 20 June also identified Ku-band reflectivity and drop size increasing towards the surface, indicating CC-dominant precipitation or a balance between CC and drop breakup. These features are consistent with warm rain processes associated with tropical rainfall (Fig. 10). One possible reason for the occurrence of TCMI2 was the presence of anomalous mean latent heat fluxes of 105 Wm^{-2} over the region, with the land surface obtaining oceanic influences on the re-intensification of Bill (Wakefield et al. 2020).

2.5 Conclusions

The inland progression of Tropical Storm Bill over Texas and Oklahoma followed a two month period with record high precipitation throughout the region, which provided a unique opportunity to explore the microphysical evolution using polarimetric radar observations from the WSR-88D network and the GPM DPR. The exceptional precipitation during the 45 days prior to Bill resulted in anomalously high soil moisture and latent heat fluxes over the region, acting to increase boundary layer moisture and increase the warm cloud depth through latent heat release. As a result, Bill maintained tropical, warm rain characteristics as it tracked inland over southern Oklahoma and produced over 400 mm of rainfall in the aforementioned four day period during TCMI1. The polarimetric radar observations and GPM DPR measurements showed increasing reflectivity towards the surface below the melting layer, which is consistent

with CC-dominant precipitation and/or a balance between CC and drop breakup. These signatures are consistent with tropical cyclone environments.

As Bill progressed inland over Missouri, southern Illinois, and Kentucky, an additional TCMI occurred. While dominant precipitation signatures were found to be associated with size-sorting and evaporation below the melting layer, there were still signatures of CC in the WSR-88D observations and the GPM DPR retrievals. Additionally, investigation of atmospheric dynamics during TCMI2 illustrates ascent rates that were similar to those in shallow, tropical convection, and low level positive PV anomalies indicative of low and mid-level latent heat release found in TCs. This further demonstrates that Bill maintained tropical characteristics from a dynamical framework several days post-landfall.

Limitations of this work include that the GPM DPR was only able to extract vertical profiles of reflectivity and drop size distribution moments at snapshots in time, limiting the extent in which a TCMI was observed from spaceborne radar. The echo top heights in the ground-based radar observations were also 2 km higher than the GPM DPR retrievals, which may be due to re-gridding of the WSR-88D data. Additional uncertainties arise with the ERA-5 reanalysis being unable to fully resolve the spatial details in the PV and vertical velocity fields, which may explain the vertical discontinuity in mid level PV as shown in Figure 12.

Future work should examine more places throughout the inland progression of Tropical Storm Bill as it moved into Missouri and northeastern Oklahoma to deter-

mine the temporal extent to which Bill maintained tropical rainfall characteristics. Additionally, it would be useful to compare this event to other less pronounced TCMI cases using the GPM DPR on a global scale and using ground-based radar measurements where available. Future analyses could also incorporate the use of disdrometer data to more precisely quantify the drop size distribution moments to compare to the GPM DPR algorithms that are used to estimate D_M and $log_{10}(N_W)$ from space. Another area that can be explored in future work are the impacts of latent heating on precipitation microphysics during periods of TCMI. Lastly, future research could perform a modeling study of the dynamics and thermodynamics associated with the TCMI periods to account for the uncertainties in the ERA-5 reanalysis.

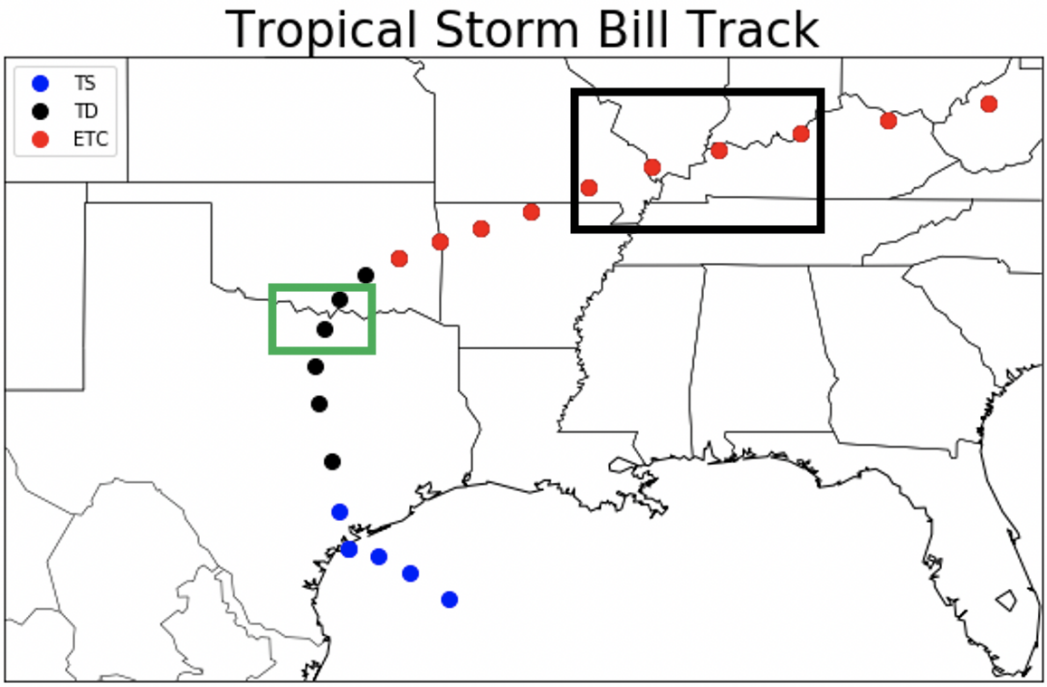

Figure 1: Hurricane Database (HURDAT2) Best Track plot of Tropical Storm Bill from 16-21 June, 2015. Each point is spaced apart in 6-hour time increments. The green box represents the location of TCMI1 from 1200-1800 UTC 17 June, and the black box represents the location of TCMI2 from 1200 UTC 19 June to 1200 UTC 20 June.

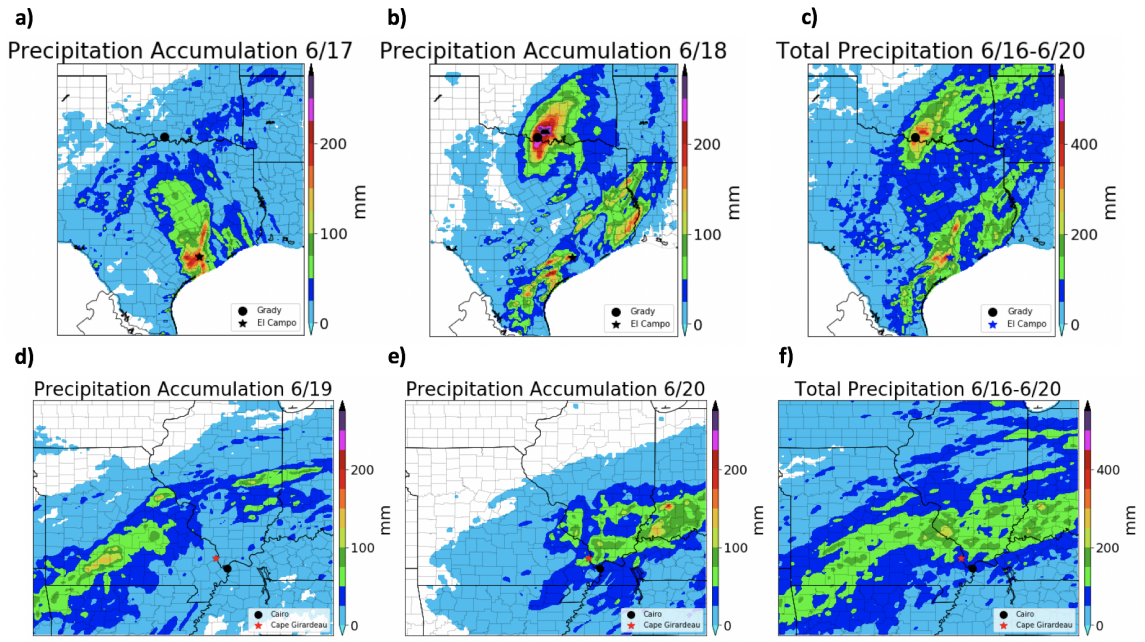

Figure 2: PRISM daily accumulated precipitation over Texas and Oklahoma from 16-17 June (a. and b.), total accumulated precipitation from 16-20 June (c.), daily accumulated precipitation over Missouri and Illinois from 19-20 June (d. and e.), and total accumulated precipitation from 16-20 June (f.).

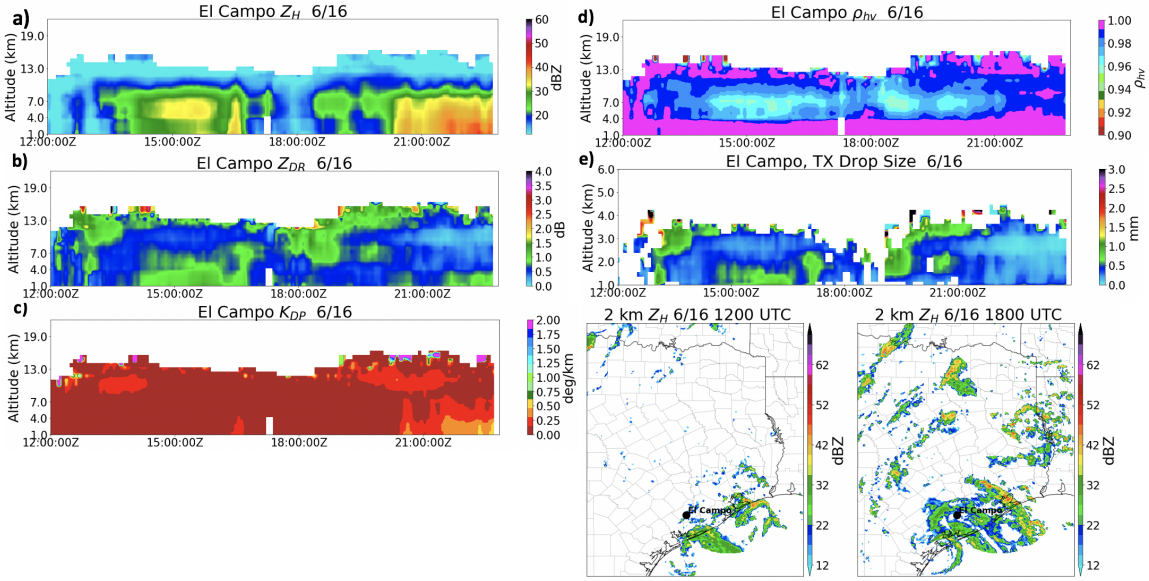

Figure 3: Time-height curtains of Z_H (a), Z_{DR} (b), K_{DP} (c), ρ_{hv} (d), and drop size (e) near the landfall point over El Campo, TX on from 1200 UTC 16 June-0000 UTC 17 June, and images of 2 km Z_H at 1200 UTC and 1800 UTC 16 June.

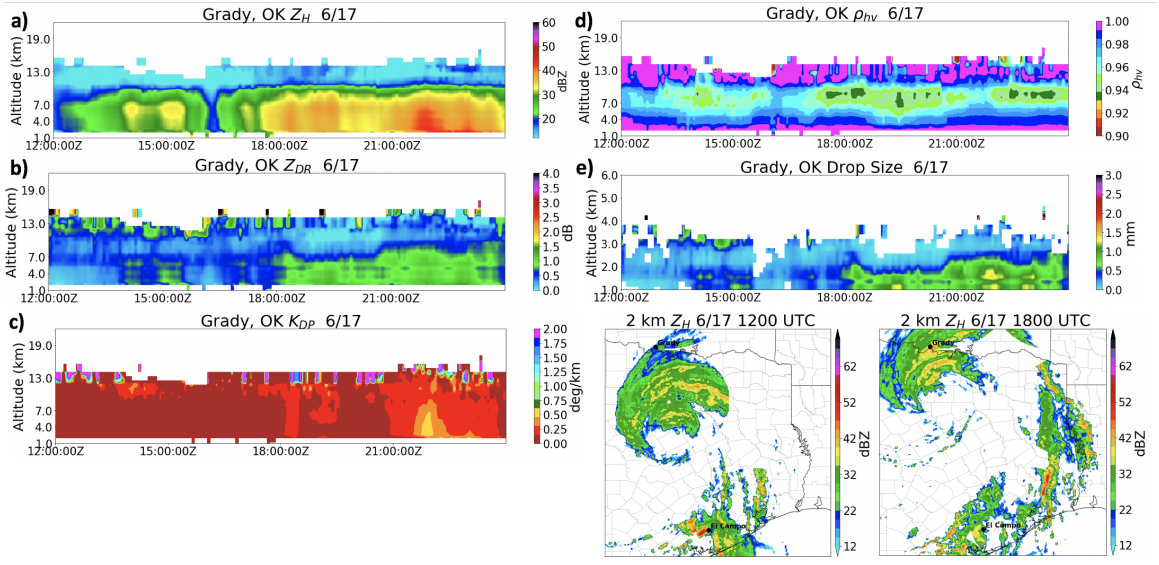

Figure 4: Time-height curtains of Z_H (a), Z_{DR} (b), K_{DP} (c), ρ_{hv} (d), and drop size (e) during TCMI1 over Grady, OK on from 1200 UTC 17 June-0000 UTC 18 June, and images of 2 km Z_H at 1200 UTC and 1800 UTC 17 June.

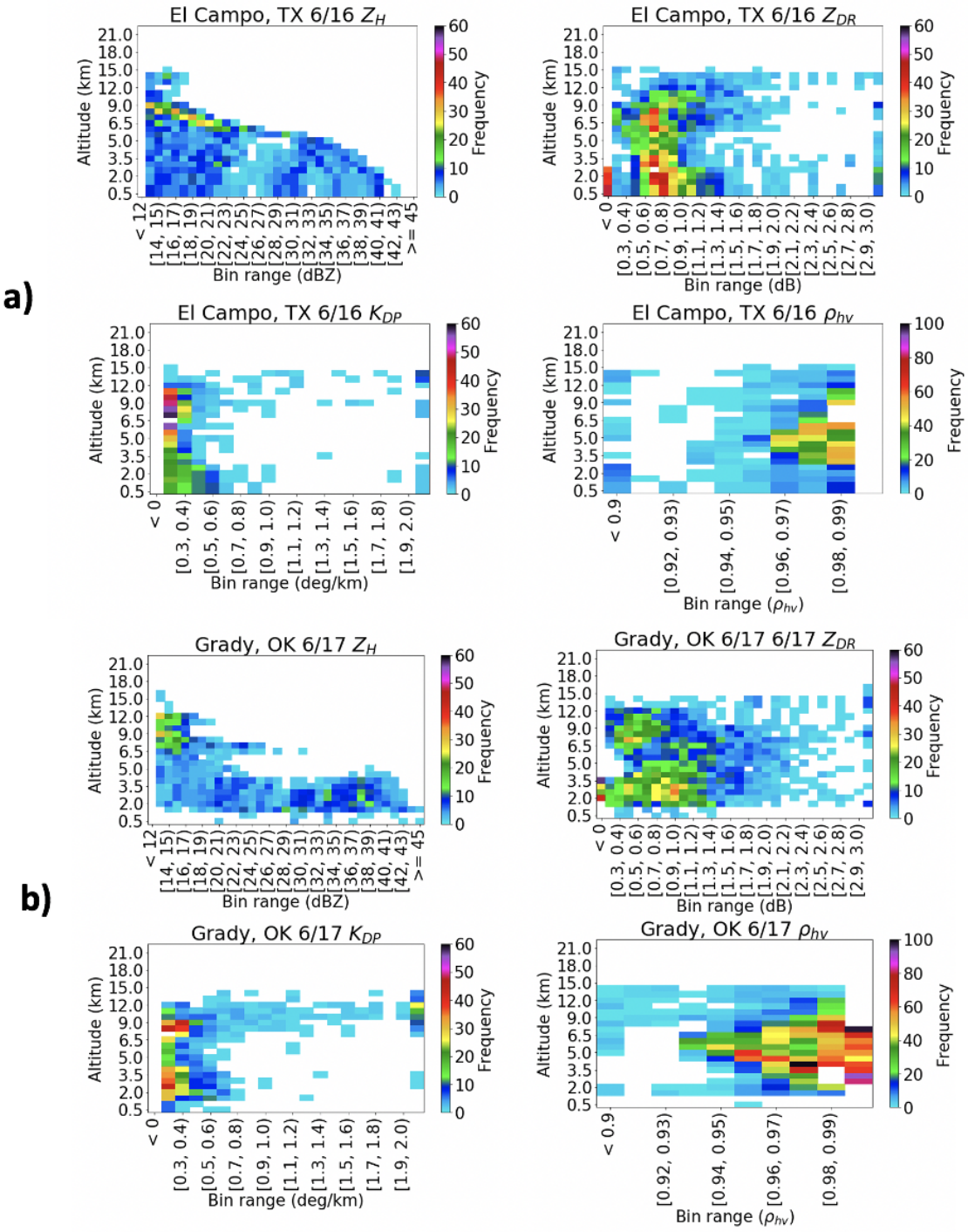

Figure 5: Contoured Frequency By Altitude Diagrams (CFADs) of Z_H Z_{DR}, K_{DP}, and ρ_{hv} at El Campo, TX on 16 June (a), and Grady, OK on 17 June during TCMI1 (b).

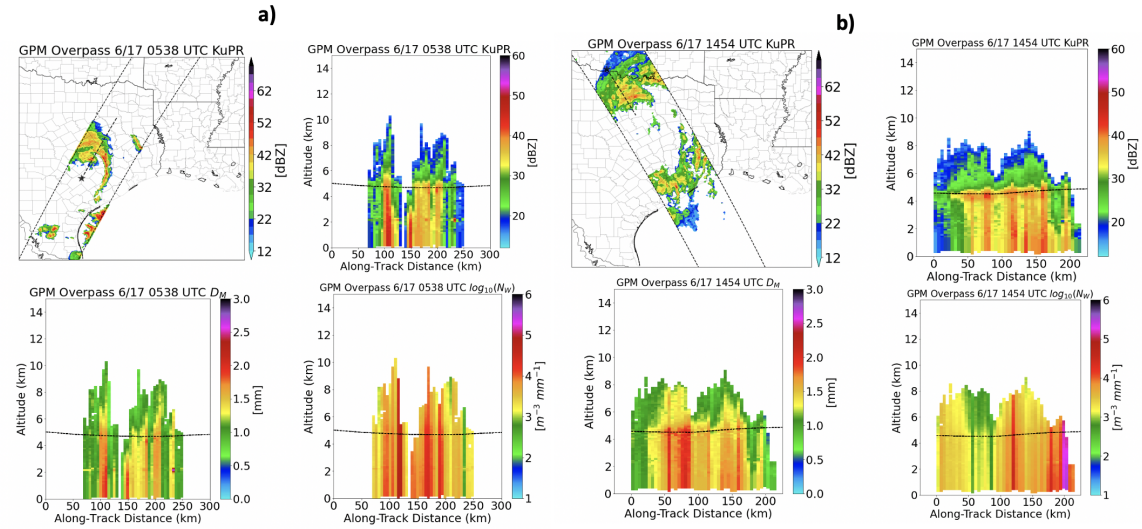

Figure 6: GPM DPR along-track vertical profiles of $Z_M(Ku)$, D_M, and $log_{10}(N_W)$ at 0538 UTC (a) and 1454 UTC (b) on 17 June, 2015 over Texas. The dashed line represents the 0^oC isotherm.

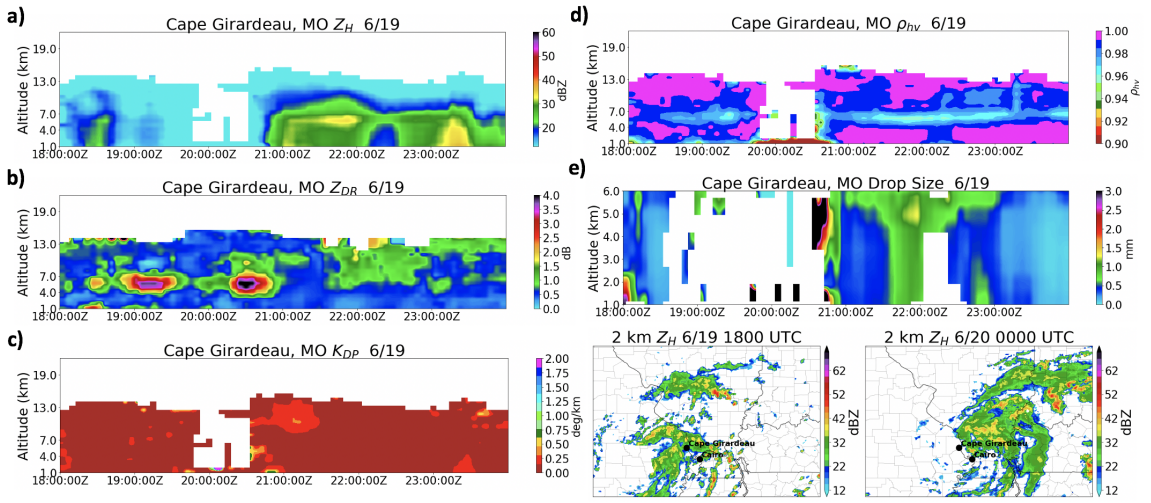

Figure 7: Time-height curtains of Z_H (a), Z_{DR} (b), K_{DP} (c), ρ_{hv} (d), and drop size (e) during TCMI2 over Cape Girardeau, MO on from 1800 UTC 19 June-0000 UTC 20 June, and images of 2 km Z_H at 1800 UTC 19 June and 0000 UTC 20 June.

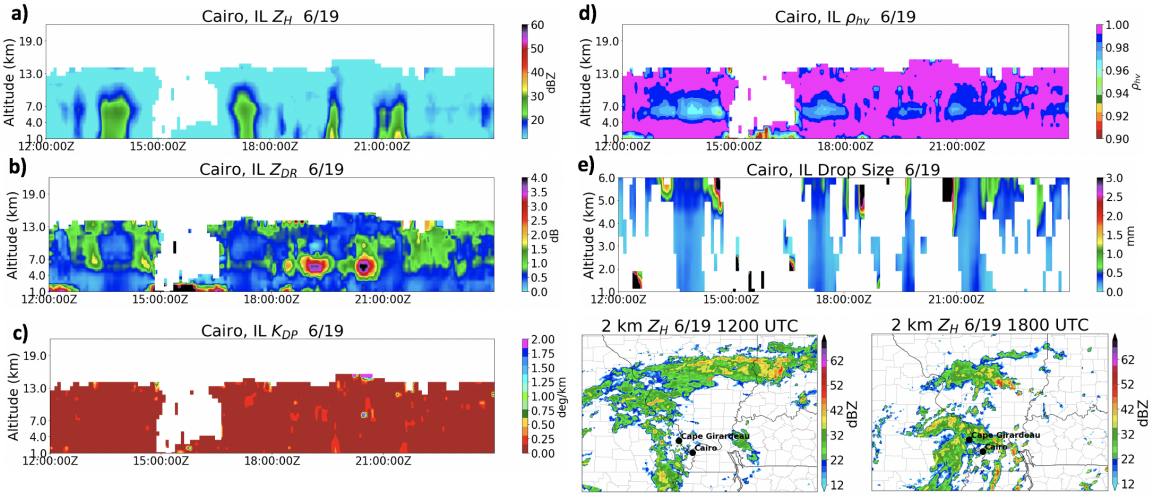

Figure 8: Time-height curtains of Z_H (a), Z_{DR} (b), K_{DP} (c), ρ_{hv} (d), and drop size (e) during TCMI2 over Cairo, IL on from 1800 UTC 19 June-0000 UTC 20 June, and images of 2 km Z_H at 1200 UTC and 1800 UTC 19 June.

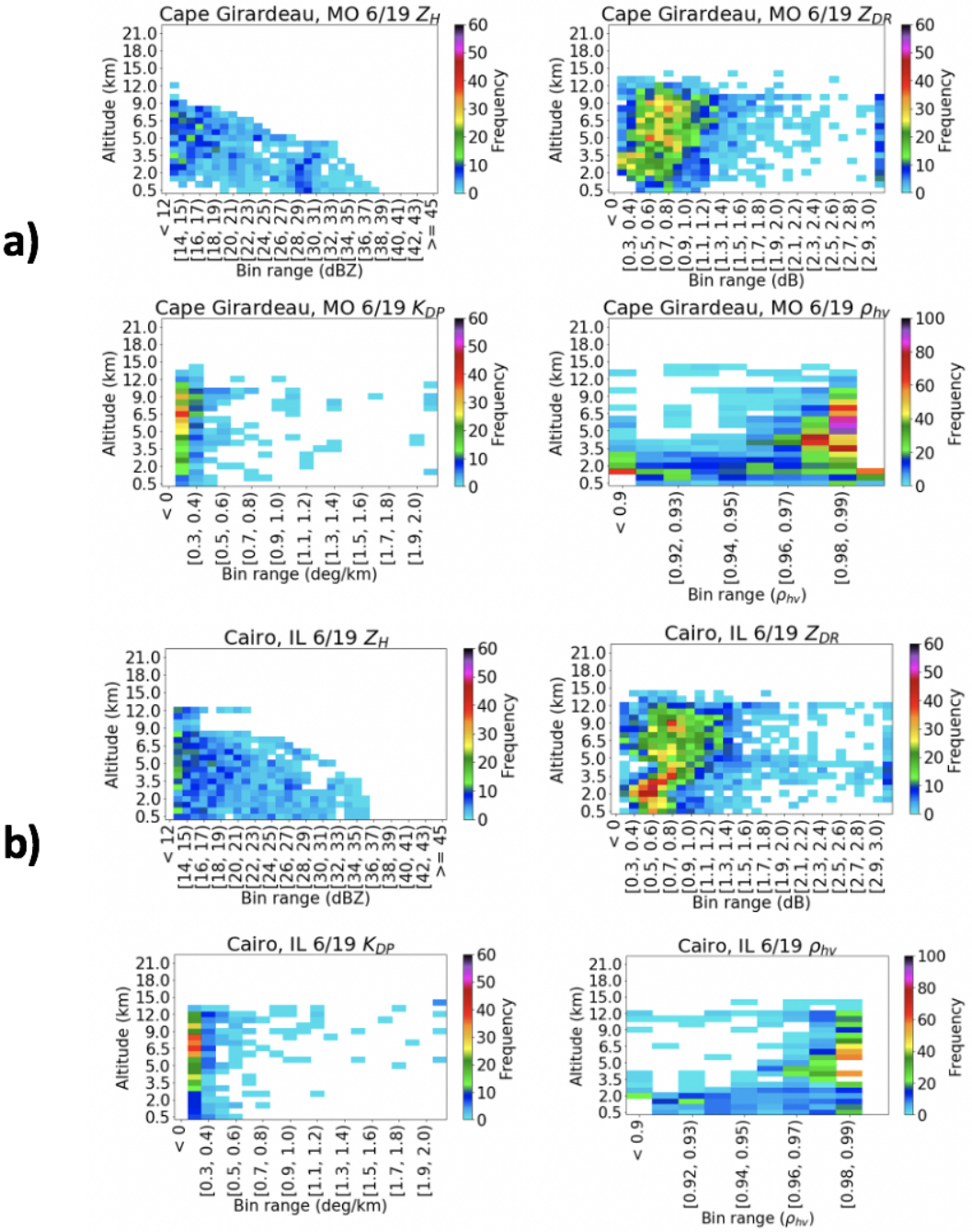

Figure 9: Contoured Frequency By Altitude Diagrams (CFADs) of Z_H Z_{DR}, K_{DP}, and ρ_{hv} at Cape Girardeau, MO on 19 June (a), and Cairo, IL on 19 June (b) during TCMI 2.

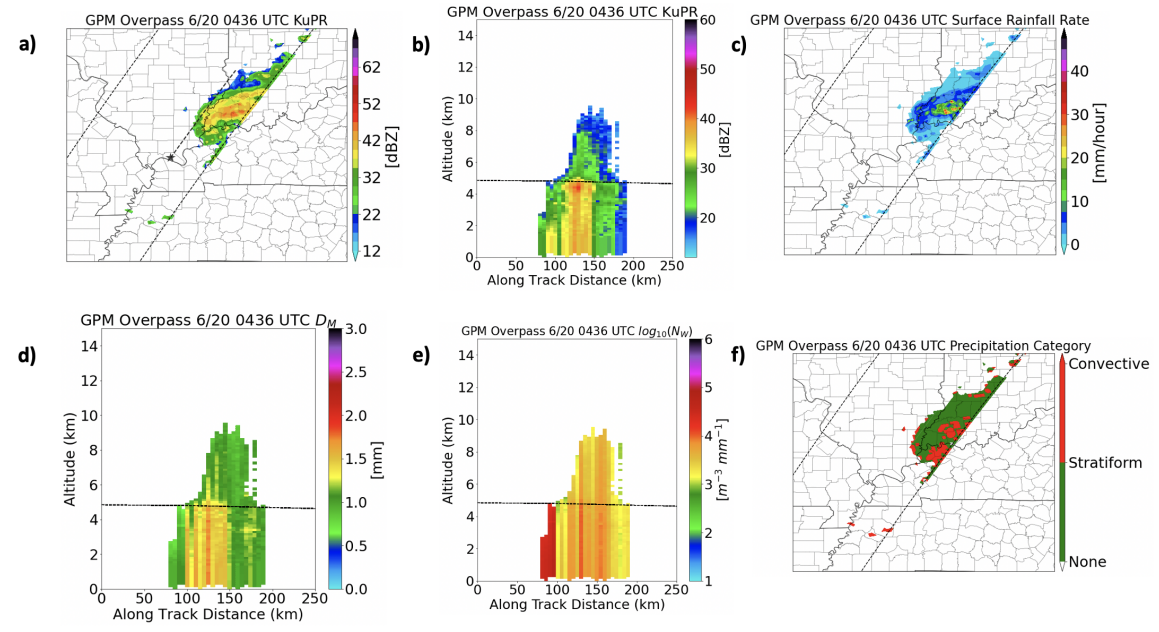

Figure 10: GPM DPR near-surface reflectivity (a), GPM DPR along-track vertical profiles of $Z_M(Ku)$ (b), surface rainfall rate (c), D_M (d), $log_{10}(N_W)$ (e), and associated regions of stratiform and convective precipitation at 0436 UTC on 20 June, 2015 over Illinois (f). The dashed line represents the 0^oC isotherm.

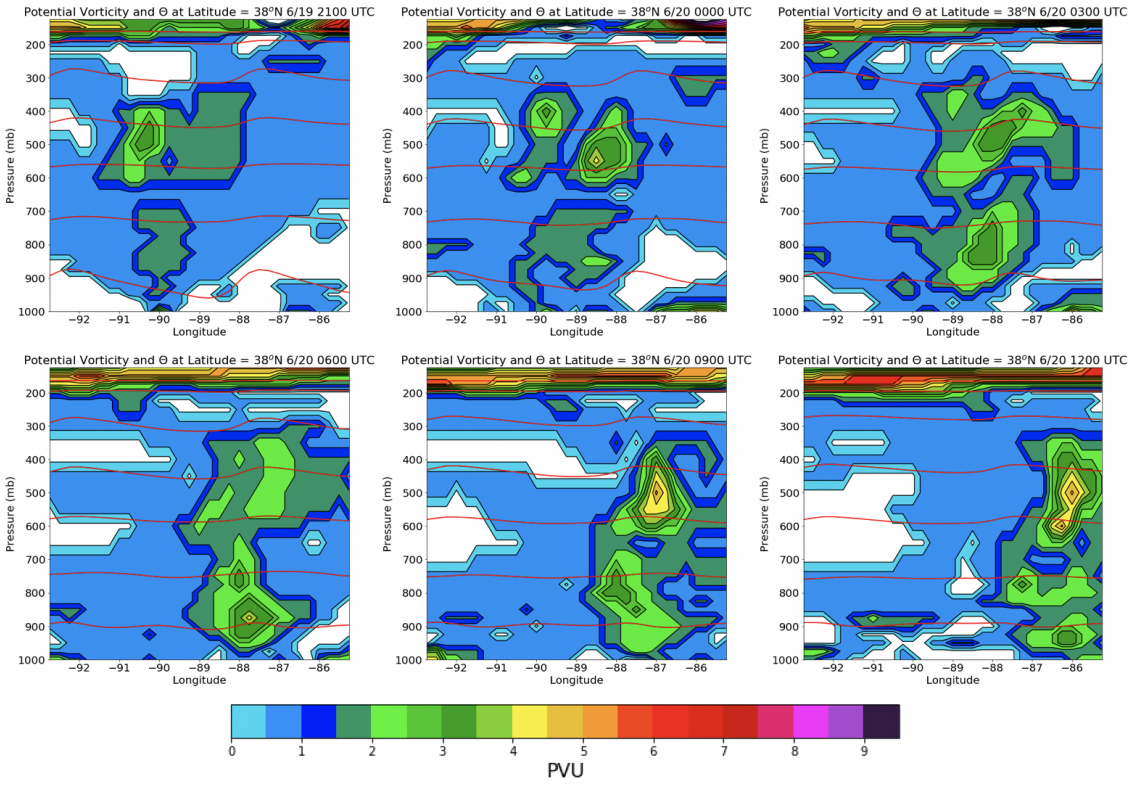

Figure 11: Longitude-height cross-sections of potential vorticity (shaded) and potential temperature (contours) along 38°N from 2100 UTC 19 June to 1200 UTC 20 June.

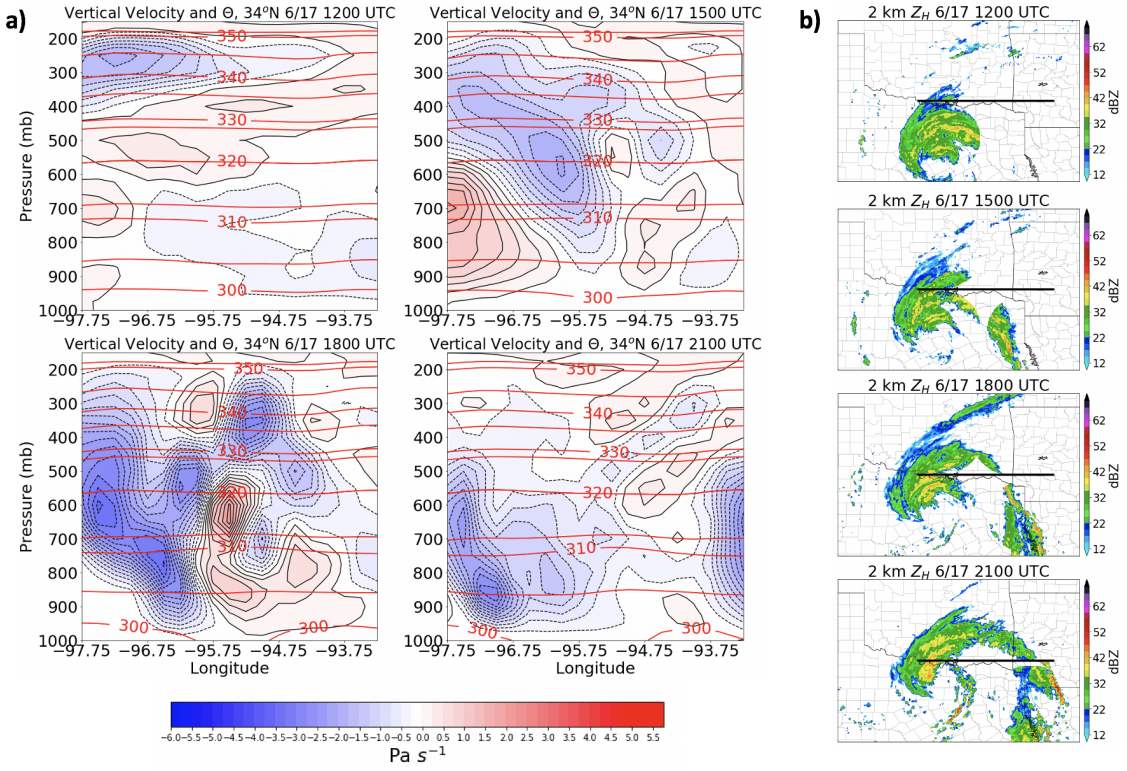

Figure 12: Longitude-height cross-sections of vertical velocity (shaded) and potential temperature (contours) along 34ºN from 1200-2100 UTC 17 June during TCMI1 (a), with snapshots of 2 km Z_H and cross-section locations (b).

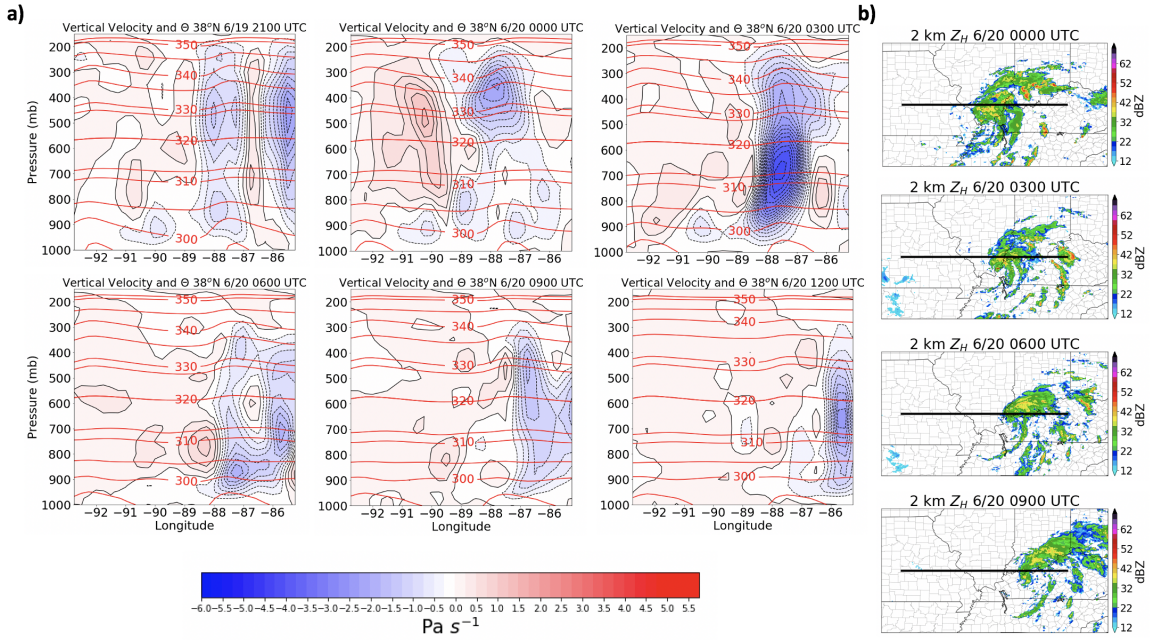

Figure 13: Longitude-height cross-sections of vertical velocity (shaded) and potential temperature (contours) along 38°N from 2100 UTC 19 June to 1200 UTC 20 June during TCMI2 (a), with snapshots of 2 km Z_H and cross-section locations (b).

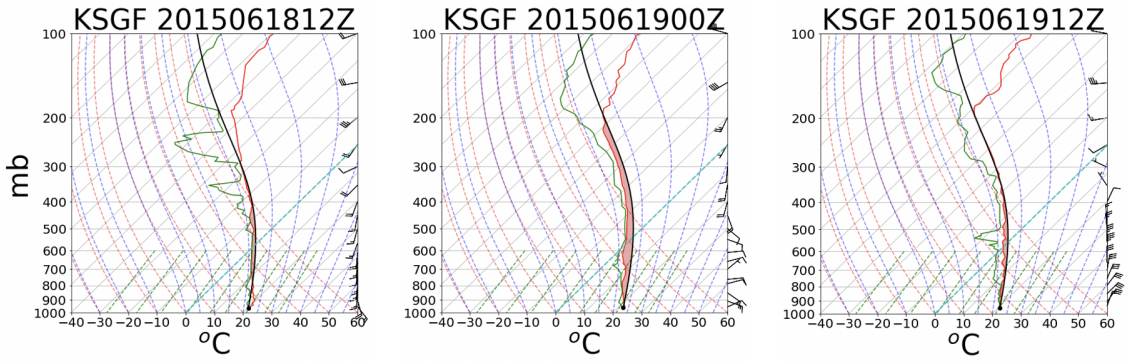

Figure 14: Observed soundings from Springfield, MO from 1200 UTC on 18 June to 1200 UTC 19 June.

3 Chapter 3: Hurricane Laura (2020): A Comparison of Drop Size Distribution Moments Using Ground and Radar Remote Sensing Retrieval Methods

3.1 Introduction

Landfalling TCs are known to produce catastrophic damage from wind, heavy rainfall, and storm surge (e.g., Rappaport 2000,Rappaport 2014). While wind damage is typically the main focus of TCs, Rappaport (2014) found that water-related deaths accounted for 90% of landfalling Atlantic TC fatalities. Therefore it is important to understand and quantify processes associated with excessive precipitation in TCs.

Microphysics in TCs are uncertain and observations often disagree with numerical simulations, which poses a challenge towards understanding TC structure, evolution, and intensity (e.g., Chen and Gopalakrishnan 2014; Hristova-Veleva et al. 2021). Prior observational studies have shown that collision-coalescence and drop breakup are the dominant precipitation processes in warm rain events such as TCs (e.g., List et al. 1987; Atlas and Ulbrich 2000). Polarimetric radar observations are useful in cases of landfalling TCs due to their high temporal resolution and large sampling domain (e.g., Medlin et al. 2007; Didlake Jr. and Kumjian 2018), and can provide useful insight into dominant precipitation processes. This can be particularly

beneficial in forecasting/nowcasting operations (e.g., Straka et al. 2000; Giangrande et al. 2008; Cunha et al. 2013) and can be used for more accurate rainfall rate estimations compared to conventional Z-R relationships (Ryzhkov et al. 2005b; You et al. 2019). Didlake and Kumjian (2017b) analyzed polarimetric radar signatures to infer precipitation microphysical processes in Hurricane Arthur (2014), and determined that the highest values of low-level differential reflectivity (Z_{DR}) occurred in the outer rainbands, whereas the lowest Z_{DR} occurred in the inner rainbands and eyewall. This implies significant changes in the drop size distribution as a function of distance from the hurricane center. It has also been shown that there is typically a maximum in specific differential phase (K_{DP}) displaced downwind from the relative maximum in Z_{DR} that occurs in the eyewall which is indicative of hydrometeor size-sorting (e.g., Feng and Bell 2019; Laurencin et al. 2020b; Homeyer et al. 2021a). This process occurs as smaller drops have a lower terminal velocity and are therefore advected further downwind, whereas larger hydrometeors fall out of the cloud at a faster rate (Kumjian and Ryzhkov 2012). DeHart and Bell (2020) found that polarimetric radar observations in Hurricane Harvey (2017) and Hurricane Florence (2018) exhibited signatures associated with large concentrations of small and medium drops, with Harvey having the greatest particle size distribution (PSD) variability over time. These are similar to the results from Zheng et al. (2021), who also concluded that collision-coalescence and accretion are the dominant processes in mature inner rainbands. Further, Tokay et al. (2008) analyzed landfalling TCs from three disdrometer

sites from 2004-2006 and found that all TCs contained large concentrations of small to medium-sized drops except when each storm had undergone extratropical transition. This is also consistent with Homeyer et al. (2021a), who showed a variation in mass-weighted mean drop diameter (D_M) ranging from 0.5-2.0 mm at various points in time throughout the evolution of Hurricane Harvey (2017) and Hurricane Florence (2018). Last, Brauer et al. (2020) found that training supercell thunderstorms in the outer rainbands of Hurricane Harvey contained large concentrations of medium-sized drops which contributed to the excessive precipitation event over the region.

Spatially within TCs, McFarquhar and Black (2004) analyzed two events and determined that there is a large variation in the drop size distribution from stratiform to convective regions. Prior work from Cecil et al. (2002) showed that Z_H increases towards the surface within the warm cloud layer, particularly in the inner core of TCs. Kumjian and Ryzhkov (2012) and Carr et al. (2017) attributed this decrease in Z_H with height with collision-coalescence or a balance between collision-coalescence and drop breakup depending on the slope of Z_{DR} within the same layer. While dominant precipitation processes can be inferred from ground-based polarimetric radar observations, coarse vertical resolution and beam-broadening at a large range limits the extent in which these signatures can be captured. For this reason, it is useful to complement ground-radar observations with space-borne radar retrievals which have a much finer vertical resolution and can provide vertical profiles of reflectivity and extracted PSD moments at snapshots in time (e.g., Hou et al. 2014; Skofronick-

Jackson et al. 2017; Porcacchia et al. 2019). Additionally, space-borne radars such as the NASA Global Precipitation Measurement (GPM) mission dual-frequency precipitation radar (DPR) tend to be much better calibrated compared to ground radars (Warren et al. 2018).

The Tropical Rainfall Measurement Mission (TRMM) was the first space-borne radar to sample precipitation in TCs after becoming operational in 1997 (Kummerow et al. 1998), and was able to properly identify the spatial and temporal variations in TCs in the low latitudes (Jiang et al. 2011). Since TRMM, the NASA Global Precipitation Measurement (GPM) mission dual-frequency precipitation radar (DPR) was launched in February 2014 and is equipped with both Ku and Ka-band active sensors, and is capable of sampling TCs at higher latitudes whereas TRMM was confined to 35° N/S (Hou et al. 2014; Skofronick-Jackson et al. 2017). Huang and Chen (2019) analyzed 68 TCs in the Western North Pacific using the DPR and determined that the 2 km D_M was larger in regions of convection compared to areas of stratiform precipitation. It was also found that in regions of high precipitation efficiency, KuPR and D_M increased towards the surface below the melting layer in both convective and stratiform areas implying drop growth via collision-coalescence. A similar framework was used in Porcacchia et al. (2019) who investigated the slopes of KuPR and KaPR from the DPR and Z_H and Z_{DR} from ground radars in warm rain events and found that precipitation events that were characterized primarily by collision-coalescence typically have a lower ice content above the 0^oC level than

non-collision-coalescence cases.

Numerical simulations of Hurricane Rita (2005) were compared to TRMM space-borne radar retrievals, and showed that model output overestimated the magnitude of ice content compared to the observations (Hristova-Veleva et al. 2021). They further showed that the assumed PSD algorithm intercept parameter (N_0) used in the Weather Research and Forecasting (WRF) model simulations resulted in differences between the observed and modeled reflectivity. Due to the known differences between PSD estimates from the space-borne radar retrievals in TCs and ground-based radar observations, in-situ disdrometers can be used to calibrate polarimetric radar observations to precipitation moments in order better refine the DPR PSD algorithm (e.g., Liao et al. 2014; Radhakrishna et al. 2016).

Ground-based disdrometer retrievals and aircraft-mounted optical array probe observations have historically been used to empirically derive Z_H-weighted rainfall rate relationships in TCs, commonly known as Z-R relationships (e.g., Wilson and Pollock 1974; Jorgensen and Willis 1982; Ulbrich and Lee 2002). However microphysical and precipitation processes near the surface using ground radars can only be inferred as these retrievals are prone to discrete sampling due to beam broadening, attenuation at higher frequencies such as C-band and X-band, partial beam filling, and increasing beam height with range (e.g., Ryzhkov 2007; Kirstetter et al. 2013; Zhang et al. 2013). Therefore it is important to obtain observations at the ground to more accurately quantify PSD moments. Many field campaigns have compared

mobile radar retrievals to disdrometer observations and have found differences between radar reflectivity and disdrometer-derived reflectivity for these reasons (e.g., Sheppard and Joe 1994; Kalina et al. 2014). Merceret (1974) gathered aircraft foil impactor measurements in Hurricane Ginger (1971), and found that an exponential distribution provided an accurate fit for the PSD, which is also true in other cases as uncertainties are higher when using a gamma distribution to estimate PSD moments (Smith 2003). A network of 2D video disdrometers, a Joss–Waldvogel disdrometer, and OTT Parsivel disdrometers in Huntsville, AL sampled precipitation events over 6 months and found that when $D_M < 0.76$ mm, the Parsivel greatly underestimated drop concentration (Tokay et al. 2013). Further, the same study concluded that PSDs that were skewed by drops > 2.4 mm yields an overestimation of drop concentration. Another study compared OTT Parsivel disdrometers with 2D video disdrometers for 36 rainfall events in South Korea, where the Parsivels were found to overestimate D_M when using a gamma distribution while underestimating the magnitude of $log_{10}(N_w)$ (Park et al. 2017). With the known disadvantages of the Parsivel disdrometers such as a high uncertainty of PSD quantities at a $D_M > 5$ mm in addition to a high bias in $log_{10}(N_w)$ at values of $D_M > 2.4$ mm, these in-situ observations can be used as a benchmark for validation of inferred PSD moments from ground and space-borne radar retrievals (e.g., Lee and Zawadzki 2006; Tokay et al. 2013). GPM DPR retrievals were compared to disdrometer observations in China, and it was shown that stratiform precipitation regions in warm season rainfall events showed the largest val-

ues of N_0, slope parameter (Λ), and shape factor (μ) compared to areas of convection and winter precipitation cases (Wu et al. 2019). Disdrometer observations from 7 Atlantic TCs were collected from 2004-2006 and showed that D_M was largely lower than 4 mm and PSDs consisted of a large concentration of small drops throughout the entire TC evolution before extratropical transition (Tokay et al. 2008). As disdrometer observations frequently suffer from measurement and sampling biases, it is useful to compare the PIPS retrievals to ground and space-borne radar observations to more accurately quantify the evolution and magnitude of PSD moments throughout different portions of Hurricane Laura before, during, and after landfall. While the comparison between remote sensing retrievals and disdrometer observations is useful, the differences in horizontal footprints between the GPM DPR (5 km), SR1-P (37.5 m gates), and point observations from the PIPS must be considered.

Given the importance of accurately predicting the water threat that TCs pose, combined with the uncertainties of radar observations (particularly at the low levels), and the general lack of detailed in situ observations near the surface, a need exists for an in depth look at available remote data sources compared to direct observations. Such a detailed look would provide valuable insight into the Z-R relations used in TC forecasting/nowcasting and allow for a more accurate threat representation when viewing remote sensing observations (such as radar) during events. Further, an improved understanding of TC microphysics would benefit future microphysical parameterization schemes in numerical models to better predict TC structure and

evolution.

The combination of one OU-CIMMS polarimetric C-band Shared Mobile Atmospheric Research and Teaching (SMART) Polarimetric Radar (SR1-P) (Biggerstaff et al. 2005), 4 PIPSs (Dawson et al. 2017) equipped with Parsivel laser disdrometers, and two overpasses from the GPM DPR provides a novel framework for quantifying various drop size distribution characteristics and precipitation microphysics in a landfalling TC. Each retrieval method provides unique advantages such as a high temporal resolution from the ground radar observations and disdrometers in addition to a fine vertical sampling from the GPM DPR. Thus, the disadvantages of each observation platform can be complemented by the aforementioned advantages of all retrieval methods. This study aims to quantify the hypothesized difference in PSD moments that are extracted by the DPR algorithm with the disdrometer observations that were collected before, during, and after the landfall of Hurricane Laura.

3.2 Data and Methods

3.2.1 Event Background

Hurricane Laura developed from an African easterly wave that entered the northeastern Caribbean Ocean on 22 August 2020, and interacted with the higher terrain of Hispaniola and Puerto Rico as a tropical storm before entering the Gulf of Mexico. As Laura moved off Cuba into the Gulf of Mexico on 25 August, the storm began rapid intensification and reached a peak intensity as a Category 4 hurricane with

maximum sustained winds of 130 knots and a minimum central pressure of 937 hPa on 27 August (National Hurricane Center 2021). Laura made landfall near Cameron, Louisiana at 0600 UTC 27 August as a Category 4 major hurricane and caused severe wind damage to the Lake Charles, LA and surrounding area, including the Lake Charles radar (KLCH). Freshwater flooding and storm surge flooding occurred close to the landfall point in Calcasieu Parish, LA where 12" of rain fell. Additional flooding occurred further inland over southern Arkansas as Laura tracked north (National Hurricane Center 2021).

3.3 Ground-Based Radar Observations

The KLCH WSR-88D (30.13^oN, -93.22^oW) operates at S-band (10 cm) and was used in conjunction with a SMART C-band radar (SR1-P, 5 cm) located at 30.36^oN, -92.92^oW in the anticipated landfall zone. SR1-P collected polarimetric radar observations of Z_H, Z_{DR}, K_{DP}, and ρ_{hv} from 1942 UTC 26 August to 1200 UTC 27 August. Due to wind gusts in excess of 120 mph, the KLCH radar stopped operating at 0553 UTC 27 August as the inner core of Laura moved onshore and the radar sustained catastrophic damage.

The radar reflectivity factor at a horizontal polarization (Z_H) provides insight into the size and concentration of hydrometeors within a range bin (e.g., Austin 1987; Herzegh and Jameson 1992; Zrnic and Ryzhkov 1999; Kumjian 2013a; Vitale and Ryan 2013). Differential reflectivity (Z_{DR}) is defined as the logarithmic ratio

of the horizontal reflectivity factor to the vertical reflectivity factor, and provides information regarding the size, shape, and orientation of hydrometeors (e.g., Seliga and Bringi 1976; Herzegh and Jameson 1992; Kumjian 2013a). Specific differential phase (K_{DP}) is defined as one half the range derivative of the propagation differential phase shift, and reveals information about the number concentration of hydrometeors in a sample volume (e.g., Herzegh and Jameson 1992; Zrnic and Ryzhkov 1999; Ryzhkov et al. 2005b; Kumjian 2013b) and is immune to attenuation and radar miscalibration assuming uniformly distributed scatterers (e.g., Seliga and Bringi 1978; Jameson 1985; Wang and Chandrasekar 2009) making it a useful variable for quantitative precipitation estimation. Lastly ρ_{hv} can be used to quantify the diversity of scatterers, to distinguish meteorological versus non-meteorological returns (e.g., Herzegh and Jameson 1992; Zrnic and Ryzhkov 1999; Ryzhkov et al. 2005c; Ryzhkov et al. 2005b; Kumjian 2013a), and identify features such as the melting layer (e.g., Kumjian 2013a; Kumjian 2013b). A uniform particle size distribution will yield a ρ_{hv} near 1 whereas mixed-phase precipitation results in $\rho_{hv} < 0.95$ (e.g., Herzegh and Jameson 1992; Zrnic and Ryzhkov 1999; Ryzhkov et al. 2005c; Ryzhkov et al. 2005b; Kumjian 2013a).

Range height indicator (RHI) scans from SR1-P were collected over the PIPS and plotted from 0211-0259 UTC 27 August at an azimuth angle of 160°, and from 0510-0541 UTC at an azimuth angle of 220°. Time-averaged mean RHIs of Z_H, Z_{DR}, and ρ_{hv} were computed over both time periods and azimuth angles in order to gain insight

into the dominant precipitation processes at different stages in the evolution of Laura shortly before landfall. Further, RHIs provide a high vertical resolution and insight into the connection between precipitation features aloft and near the surface. In order to account for Z_{DR} miscalibration, a bias correction method documented in Sanchez-Rivas and Rico-Ramirez (2021) was employed. "Bird bath" style Z_{DR} calibration requires data to be collected at 90° elevation (Gorgucci et al. 1992), but such data were not collected during the SR1-P observation period in Hurricane Laura. Likewise, the Z_{DR} calibration method of Ryzhkov et al. (2005a) is not applicable, as it requires PPIs between 40 and 60 degree elevation to be utilized. Again, no such data were collected. Thus, the method of Sanchez-Rivas and Rico-Ramirez (2021) is optimal, as their method utilizes quasi-vertical profiles (QVPs) (Ryzhkov et al. 2016) collected in light rain to estimate the Z_{DR} bias. The Sanchez-Rivas and Rico-Ramirez (2021) method utilizes a QVP constructed at the 10° elevation angle and uses data where Z_H is between 0 and 20 dBZ and where $\rho_{hv} > 0.985$. While their method employs the use of data between the first radar range gate and the melting level (characterized by an objective algorithm), we take a simpler approach and only employ QVP data between 1 and 4 km altitude, below the radar bright band. While there was only one QVP where such criteria were met, a bias of -1.7 dB was computed for this case, which is a typical bias for SR1-P (e.g., Biggerstaff et al. 2021). As drops in hurricanes are typically small (as evidenced in this manuscript) and to include a greater number of QVPs to test the sensitivity of the computed bias to the number of observations, we

also extended the method to include data characterized by 0-25 dBZ (0-30 dBZ) and found a similar Z_{DR} bias of -1.7 dB (-1.8 dB). To remain consistent with Sanchez-Rivas and Rico-Ramirez (2021), we add -1.7 dB to all Z_{DR} observations herein. The large calibration bias is due to a bad input parameter that was embedded in the proprietary software during the dual-polarization upgrade. Rather than attempt to find and replace the parameter, we chose to perform the calibration in post-processing.

Additionally, plan position indicator (PPI) scans of Z_H from SR1-P were plotted at 0230 UTC and 0525 UTC on 27 August with the locations of the associated RHI scans. Finally, columnar-vertical profiles (CVPs) of Z_H, Z_{DR}, K_{DP}, and ρ_{hv} from SR1-P were plotted from 0200-1000 UTC 27 August which used the methodology from Murphy et al. (2020). The CVPs were constructed using a Cressman weighting function (Cressman 1959) to transform from an irregular height grid to a regular (50 m) height grid. Further, the CVPs were conducted directly over PIPS 2A and were based on a +/- 10 km (10 degree) range (azimuth), with a Cressman radius limit of 100 m. One potential limitation of the CVP method is that the Cressman weighting function that was used can still resulting in vertical gaps in polarimetric radar data.

Dominant precipitation processes were determined by examining the sign of slopes of vertical profiles of Z_H and Z_{DR} within the warm cloud layer based off the framework from Kumjian and Ryzhkov (2012) (Fig. 15). For example, collision-coalescence dominant precipitation would be identified in vertical profiles where both Z_H and Z_{DR} increase towards the surface below the melting layer, implying the presence of

drop growth.

3.3.1 GPM Dual-Frequency Precipitation Radar

The NASA GPM mission was launched in 2014 and operated similarly to the TRMM, which ended in 2015 (Hou et al. 2014; Skofronick-Jackson et al. 2017). On board the GPM platform is the DPR, which operates at Ku and Ka-bands (35.5 GHz and 13.6 GHz) (Hou et al. 2014; Skofronick-Jackson et al. 2017) and can provide snapshots of the precipitation structure in TCs on a global scale (e.g., Huang and Chen 2019; Marra et al. 2019; Brauer et al. 2021). The radar has a swath width of 245 km, a vertical resolution of 250 m, and a horizontal resolution of 5.2 km (Hou et al. 2014; Skofronick-Jackson et al. 2017). The DPR algorithm extracts PSD moments such as the mass-weighted mean drop diameter (D_M) (mm) and the normalized intercept parameter ($log_{10}(N_w)$) (m^{-3} mm^{-1}) which relates to hydrometeor concentration, and assumes a gamma distribution in liquid phase precipitation (Equation 4), where N_0 (m^{-3} mm^{-1}) is the intercept parameter and D_0 (mm) is the median volume diameter. D_M can then be related to D_0 using equation 5, which can be used to compute $log_{10}(N_w)$. More information regarding the DPR algorithm to estimate PSD moments can be found here: (`https://gpm.nasa.gov/sites/default/files/document_files/ATBD_GPM_DPR_n3_dec15.pdf`). Further, the GPM DPR surface reference for attenuation correction that is used over land is less reliable than over the open ocean, resulting in some uncertainties in near-surface PSD retrievals (Menegh-

ini et al. 2015). However recent advances in the DPR PSD algorithm (version 4) suggests that KuPR has a probability of detection of 0.967 in surface rainfall rates greater than 1 mm h^{-1} over flat terrain (Speirs et al. 2017). Additionally, Liao and Meneghini (2019) determined that D_M biases from the DPR are generally < 0.5 mm across the entire PSD. Cannon et al. (2017) also showed the utility of the DPR in estimating precipitation over the ocean in the eastern North Pacific Ocean, with accurate representations of the bright-band height when compared to reanalysis data and ground radars.

$$N(D) = N_0 D^{\mu} exp\left[-\frac{(3.67+\mu)D}{D_0}\right] \tag{4}$$

$$D_0 = \left(\frac{3.67+\mu}{4+\mu}\right) D_M \tag{5}$$

Along-track cross-sections of Ku-band reflectivity (KuPR), D_M, and $log_{10}(N_w)$ were plotted from the available DPR overpasses that occurred from 0228-0401 UTC and 1144-1316 UTC 27 August (Fig. 20 and Fig. 21). Additionally, attenuation-corrected near-surface KuPR is shown to illustrate the cross-section locations and the spatial distribution of precipitation after Laura made landfall. The DPR-extracted 0^oC isotherm was also included on each cross-section to quantify the height of the melting level and to provide a direct comparison with the ground radar retrievals. The 0^oC level is determined by identifying the location of the bright band in the DPR algorithm. Additionally, vertical profiles of 25th, 50th, 75th, and 95th quantiles

of KuPR were computed to illustrate the slope of reflectivity below the melting level to infer collision-coalescence and/or drop breakup processes (Porcacchia et al. 2019).

3.3.2 Portable In-Situ Precipitation Stations (PIPS)

Four PIPS were deployed to Hurricane Laura which measured temperature, dewpoint temperature, wind speed at 1.2 m AGL, pressure, drop terminal velocity, drop size, and drop concentration, and were strategically placed in different locations relative to the landfall point in order to sample PSDs in different portions of the storm. Efforts were made to ensure that each PIPS was located away from ground clutter such as trees, power lines, and buildings that may contaminate the PSD retrievals. Each PIPS collected data for approximately 17 hours, spanning the before, during, and post-landfall periods of Laura. PIPS1B recorded a minimum pressure of 949.8 mb which experienced the eye and northwestern eyewall. While PIPS1A was close in proximity to PIPS1B, it was far enough west to only experience the western portion of the eyewall. Only PIPS2A sampled the eastern eyewall with PIPS2B sampling the outer edge of the inner core and outer rainbands, with PIPS1A, PIPS1B, and PIPS2A all experiencing peak winds greater than 30 $m\ s^{-1}$ as Laura made landfall. Time series of drop diameter and total drop concentration $log_{10}(N_T)$ were plotted from PIPS1A (0000-0650 UTC 27 August), 2A (0000-1200 UTC 27 August), and 2B (0000-1200 UTC 27 August) as PIPS1B experienced a data corruption issue during landfall. It is important to make the distinction between $log_{10}(N_W)$ and $log_{10}(N_T)$, which

is expressed mathematically below (Eq.6) where N_0 ($m^{-3}mm^{-1}$) is the normalized intercept parameter, Γ is the Gamma function, μ is the shape factor, and Λ is the slope parameter (unitless). Further, the D_M was plotted for the aforementioned PIPS for each time period in order to provide a direct comparison with the D_M that was extracted by the DPR. Time series of D_M were plotted using a Gamma distribution as described in Tokay and Short (1996). $log_{10}(N_W)$ was also computed (Eq.7) to provide a direct comparison with the DPR retrievals, where ρ_w is the density of water ($g\ cm^{-3}$) and W is the liquid water content ($g\ m^{-3}$). For clarification, the PIPS measured $log_{10}(N_T)$ directly whereas $log_{10}(N_W)$ was computed to provide the comparison with the DPR alogirthm dervied $log_{10}(N_W)$. Additionally, Z_H and Z_{DR} were computed from the T-matrix method (Vivekanandan et al. 1991) using a C-band wavelength of 5.34 cm to directly compare the SR1-P radar observations to the disdrometer estimations. These values were then compared to 0.8^o scans from SR1-P where linear spatial means of the nearest 50 range gates of Z_H and Z_{DR} closest to the PIPS were computed and plotted as time series. A 50 range gate average was computed as the Z_H and Z_{DR} field was relatively uniform in close proximity at points in time and data quality decreases with increasing range. As the SR1-P data has a gate spacing of 75 m, the distance from the ground radar to PIPS 1A was 60 km, 12 km to PIPS 2A, and 21 km to PIPS 2B.

$$N_T = N_0 \frac{\Gamma(\mu + 1)}{\Lambda^{\mu+1}} \tag{6}$$

$$log_{10}(N_W) = log_{10}\Big(\frac{4^4 1000^3}{\pi \rho_w}\Big(\frac{W}{(D_M)^4}\Big)\Big) \tag{7}$$

The Parsivel disdrometer data were quality controlled to remove drops affected by splashing of drops off the instrument, and records that contain drops shed from the surrounding instruments on the PIPS following similar methodology to Friedrich et al. (2013). Drops that were +/- 50% of the Atlas et al. (1973) drop fall speed relation were also removed to assure that all drops passing through the disdrometer were falling as rain drops, rather than drops rolling over the edge of the Parsivel. Further quality control was applied by limiting Parsivel records based on the wind direction through the Parsivel opening. Only times when the on board sonic anemometer registered the wind direction being within +/- 45 degrees from the line normal to the plane laser were retained.

3.4 Results

3.4.1 Ground Radar Observations

Figure 17 shows a PPI of 0.5^o Z_H from the KLCH radar at 0553 UTC, as Laura made landfall on the southwestern Louisiana coast shortly before the WSR-88D become non-operational due to strong winds. At this time the PIPS were able to sample the the inner core of Laura, defined as the region between 0-100 km from the TC center (Weatherford and Gray 1988), with corresponding values of Z_H from the WSR-88D ranging from 40-50 dBZ. Before landfall at 0230 UTC 27 August, SR1-P began

sampling the outer core with Z_H values in a similar range of 40-50 dBZ (Fig. 17a). Shortly before landfall at 0525 UTC 27 August, SR1-P was located in the inner core of Laura experiencing Z_H as high as 55 dBZ and sampled the northern half of the eyewall (Fig. 17b). The corresponding black lines represent the orientation of the RHIs that were taken as Laura progressed northward across southwestern Louisiana. Time-averaged RHI scans of Z_H (Fig. 18a), Z_{DR} (Fig. 18b), and ρ_{hv} (Fig. 18c) from SR1-P from 0211-0259 UTC 27 August and 0510-0541 UTC 27 August (Fig. 18d-18f) were also plotted to gain insight into how the polarimetric radar variables changed with height. Between 0211-0259 UTC, SR1-P captured an increase in Z_H from 45 to 50 dBZ towards the surface at a beam height of 2-3 km and distance of 50-60 km from the radar (Fig. 18a). This location from the radar also exhibited a decrease in Z_{DR} towards the surface within the same layer implying a balance between collision-coalescence and drop breakup (e.g., Kumjian and Ryzhkov 2012; Carr et al. 2017; Porcacchia et al. 2019) (Fig. 18b). During this time window, the melting layer was located at a height of 4.5 km as noted by the region of $\rho_{hv} < 0.98$. (Fig. 18c) While the layer of $\rho_{hv} < 0.98$ continued to decrease in elevation beyond 25 km, this is likely an artifact of radar beam broadening rather than a decrease in melting layer height with range.

Shortly before landfall from 0510-0541 UTC 27 August, SR1-P exhibited an increase in Z_H towards the surface below the melting layer throughout the entire depth of the warm cloud layer (Fig. 18d). Subtle increases in Z_{DR} from 0.0 to 0.5 dB towards

the surface were also observed, particularly at a distance of 40-60 km from the radar (Fig. 18e). The combination of both Z_H and Z_{DR} increasing towards the surface within the warm cloud layer implies the dominance of collision-coalescence processes during this time. Additionally, the height of the melting layer also increased to 4.5-5.0 km throughout this time period, which is 0.5 km higher in altitude compared to 3 hours prior (Fig. 18f). This is likely due to latent heat release in convection in the eyewall as it moved within range of SR1-P (Kirstetter et al. 2013).

Columnar-vertical profiles of Z_H (Fig. 19a), Z_{DR} (Fig. 19b), and ρ_{hv} (Fig. 19c) from SR1-P are displayed between 0200-1000 UTC 27 August over PIPS2A. The melting layer is located at 5 km as indicated by the bright-band in Z_H, enhanced positive Z_{DR} near 1.5 dB, and reduced ρ_{hv} ranging from 0.85-0.95 due to mixed-phase precipitation. From 0200-0400 UTC, Z_H was between 25-40 dBZ within the warm cloud layer and primarily decreased towards the surface below the melting layer. During this same time, Z_{DR} varied from 0.0-0.5 dB and exhibited little variation towards the surface below the melting layer. The combination of Z_H decreasing towards the surface and Z_{DR} remaining constant within the same layer translates to inferred dominant precipitation processes of evaporation and/or drop breakup (e.g., Carr et al. 2017; Porcacchia et al. 2019). During this timeframe, ρ_{hv} remained near 1.00 implying a rather uniform size distribution of drops (Herzegh and Jameson 1992; Zrnic and Ryzhkov 1999; Ryzhkov et al. 2005c; Ryzhkov et al. 2005b; Kumjian 2013a).

From 0400-0730 UTC 27 August, near-surface Z_H increased to 35-50 dBZ (Fig.

19a) whereas Z_{DR} also increased to 1.0-1.25 dB (Fig. 19b). Further, both Z_H and Z_{DR} increased towards the surface for most of this period, translating to collision-coalescence dominant precipitation (Carr et al. 2017; Porcacchia et al. 2019), which occurred as the inner core ($<$ 100 km from TC center) moved over SR1-P from 0530-0800 UTC 27 August. There was also a slight upward displacement of the melting layer to 5.5-6.0 km from approximately 0330 UTC until 0800 UTC as latent heat release from convection in the inner core likely resulted in an increase in the height of the 0^oC isotherm (Fig. 19c). While K_{DP} generally ranged from 0.0-0.5 degrees/km before 0400 UTC in the outer core and rainbands (Fig. 19d), values of 1.0-2.0 degrees/km were sampled below 2 km in the inner core and eyewall after 0500 UTC, implying a high number concentration of medium-sized drops as Z_{DR} ranged from 0.75-1.25 dB at this time.

3.4.2 GPM DPR Retrievals

The GPM DPR sampled Laura shortly before it made landfall on the southwest Louisiana coast at 0301 UTC 27 August (Fig. 20). Figure 6 shows near-surface (just above ground level) KuPR, and vertical along-track cross-sections of KuPR, D_M, and $log_{10}(N_w)$ through the inner core and eyewall. The southwestern and northeastern eyewall is characterized by echo top heights $>$ 12 km in the deepest convection, and also experienced an upward displacement of the 0^oC isotherm to 6 km above the surface. This has been found to be associated with latent heat release in strong updrafts

as higher θ_e air is transported from the boundary layer to the mid-troposphere (e.g., Fierro et al. 2012; Kirstetter et al. 2013; McGee and van den Heever 2014). The cross-section illustrates KuPR of 50-55 dBZ in the eyewall with values ranging from 30-45 dBZ in regions of the outer core. D_M values of 2.0-2.5 mm occurred in the outer core at an along-track distance of 200-225 km, with lower values of 1.25-1.5 mm being observed in the eyewall. This differs from the location of maximum $log_{10}(N_w)$ which occurred in the eyewall and exceeded 4.5 m^{-3} mm^{-1} within the deep convection, whereas the outer core had values between 2.75-3.5 m^{-3} mm^{-1}. This suggests that pre-landfall the eyewall had a large concentration of medium-sized drops, while the outer core had a PSD skewed towards smaller concentrations of larger drops. Another possibility for this abrupt transition between D_M and $log_{10}(N_W)$ between the eyewall and outer core is a potential error in the DPR PSD algorithm. At an along-track distance of 70 km, the DPR estimated a D_M of 2.5-3.0 mm and $log_{10}(N_W)$ values of 1-2 $m^{-3}mm^{-1}$, indicating a low concentration of large drops. One potential explanation for this feature is the presence of eyewall size-sorting, similar to how Laurencin et al. (2020b) and Homeyer et al. (2021a) observed offsets in maximum regions of Z_{DR} and K_{DP} using ground radar observations.

The second DPR overpass occurred post-landfall at 1246 UTC 27 August as Laura tracked north over western Louisiana (Fig. 21). Near-surface KuPR illustrates a broader inner core region with concentric spiral rainbands extending outward from the western portion of the center of circulation. The along-track cross-section through

the rainbands shows cores of KuPR between 50-100 km and 150-175 km of 35-40 dBZ with a bright-band located between 4.5-5.0 km. Within the inner core at an along-track distance of 200-275 km, there was a slight increase in the 0^oC isotherm to 5.5 km consistent with weaker convection compared to the pre-landfall case. A region of KuPR increasing towards the surface below 3 km can also be seen at an along-track distance of 250 km, inferring the presence of collision-coalescence processes (Porcacchia et al. 2019). At the same location an increase in D_M towards the surface can be seen which is collocated with maximum values of $log_{10}(N_w)$ of 4.5 m^{-3} mm^{-1} implying the highest hydrometeor concentration in this region of the inner core. The constant values of $log_{10}(N_w)$ with height at this location are likely non-physical and a product of the DPR PSD algorithm as it is known that drop concentration typically changes with height (Carr et al. 2017).

For the aforementioned along-track cross-sections, along-track vertical profiles of 25th, 50th, 75th, and 95th percentiles of KuPR were computed to identify and compare dominant precipitation processes before and after landfall (Fig. 22). The first overpass contained more deep convective features as shown by the higher echo top heights for all percentiles. Further, there is a higher range of near-surface KuPR ranging from 23 dBZ to 50 dBZ at the surface, which is characteristic of convection. Pre-landfall, the region of enhanced KuPR located around the freezing level is deep ranging from 4.5-7.0 km which is anticipated in convection as updrafts loft mixed-phase hydrometeors vertically (e.g., Loney et al. 2002; Kirstetter et al. 2013;

Homeyer and Kumjian 2015). The post-landfall overpass illustrates a lower echo top height and a lower range in near-surface KuPR from 23-43 dBZ all indicating the presence of more stratiform precipitation. This is different from the 25th percentile profile of KuPR which exhibited no bright-band feature in the pre-landfall overpass.

Pre-landfall, the greater negative slope of the 95th and 75th KuPR percentiles between the freezing level and 2.5 km implies a higher magnitude of drop growth via collision-coalescence (Carr et al. 2017; Porcacchia et al. 2019) compared to the post-landfall overpass which illustrates a negative slope of lower magnitude, which is solely confined to the 95th percentile KuPR profile. The 25th percentile profile during this overpass shows a positive slope of KuPR below the melting layer, implying the presence of evaporation in less intense areas of precipitation, while more intense regions of precipitation (i.e. in convection) were dominated by collision-coalescence. The presence of vertical wind shear was unlikely the cause of the inferred evaporation post-landfall as 850-200 mb wind shear was less than 10 knots as Laura progressed inland (Fig. 23), therefore disruption of the inner core likely occurred due to land interaction or dry air entrainment. The longwave 200 mb ridge pattern over the Gulf Coast region that contributed to this low-shear environment was favorable for Hurricane Laura to maintain major hurricane status up to and shortly after landfall.

3.4.3 Disdrometer Observations

Figure 24 displays composite Parsivel disdrometer observations of D_M and $log_{10}(N_T)$ from PIPS 1A, PIPS 2A, and PIPS 2B between 2000 UTC 26 August and 1200 UTC 27 August. PIPS 1A experienced the western portion of the eyewall before becoming non-operational near 0700 UTC 27 August. $log_{10}(N_T)$ ranged from 2.0 to 3.25 m^{-3}, corresponding to a D_M of 0.5-1.5 mm translating to a high concentration of small drops, particularly in the western portion of the inner core. The largest D_M ($>$ 2.0 mm) observed by PIPS 1A occurred as the spiral rainbands embedded in the outer core moved over the disdrometer after 0300 UTC.

PIPS 2A sampled the outer core from 0300-0530 UTC 27 August and primarily measured drop sizes below 1.5 mm, with the greatest $log_{10}(N_T)$ of 2.0-2.5 m^{-3} occurring with D_M less than 1.0 mm. PIPS 2A observed a broader drop size distribution as the inner core moved over the station after 0525 UTC 27 August, with the largest values of $log_{10}(N_T)$ near 3.0 m^{-3} occurring with drop sizes less than 1.0 mm, implying a high total concentration of small drops in the inner core and eastern eyewall. The outer periphery of the inner core was sampled by PIPS 2B after 0430 UTC 27 August, which measured the highest $log_{10}(N_T)$ values of 3.0 m^{-3} coincident with a small drop size of 0.5-1.0 mm. Larger drops of 2.0-2.5 mm were observed at this time in the inner core, but at a lower total concentration of 1.5-2.0 m^{-3}. The drop size distribution was also much broader in the inner core compared to the outer core environment before 0330 UTC.

Figure 25 shows D_M gradually increasing from approximately 0.75 mm around 0100 UTC 27 August to near 1.5 mm at 0300 UTC 27 August as the outer core began to move over PIPS 1A. D_M then rapidly increased to values as high as 4.0 mm within the western portion of the inner core and eyewall. This may be positively skewed towards a higher D_M as a broader drop size distribution was observed after the inner core moved over the observation site. PIPS 2A observed similar values of 0.5-1.5 mm in the outer core environment before measuring D_M values in the 1.0-4.0 mm range in the inner core, which is consistent with a broadening of the drop size distribution after the inner core moved over this disdrometer after 0530 UTC. PIPS 2B observed similar D_M values of 0.5-2.0 mm in the outer core increasing to values of 1.5-4.0 mm after 0430 UTC as the disdrometer began to sample the inner core. Figure 26 illustrates the time series of $log_{10}(N_w)$ from each PIPS, and measured the values as high as 4.0 m^{-3} mm^{-1} in regions of the inner core and eyewall, while the outer core and outer rainbands were characterized by lower values ranging from 2.0-3.75 m^{-3} mm^{-1} implying a lower drop concentration.

Z_H and Z_{DR} were derived from the PIPS PSD moments to provide a direct comparison with the SR1-P observations and the GPM DPR PSD algorithm (Fig. 27 and Fig. 28). PIPS 1A observed Z_H values of 0-30 dBZ and Z_{DR} of 0-1 dB as it experienced the outer rainbands before 0300 UTC 27 August as it experienced periodic precipitation and a $D_M < 2.5mm$. Z_H rapidly increased to 30-45 dBZ and Z_{DR} increased to 1-2 dB in the outer core after 0300 UTC, with the highest values of 50-60

dBZ (Z_H) and 1-2.5 dB (Z_{DR}) occurring in the western eyewall before 0700 UTC. PIPS 2A sampled a Z_H as high as 45 dBZ in the outer core of Laura before measuring peak values of 50-55 dBZ in the inner core and eyewall after 0530 UTC, with Z_{DR} increasing to 1-2.0 dB, indicating an increase in drop size. As PIPS 2B sampled the inner core, the highest Z_H values of 45-55 dBZ were observed until 0730 UTC 27 August. However the larger values of Z_{DR} from all PIPS may be positively-biased by the larger drop sizes of 2.0-3.0 mm at a lower concentration that the disdrometer measured as Z_{DR} is independent of drop concentration (Kumjian 2013a). Further, Z_H from SR1-P is higher than the estimated Z_H from PIPS 2B, which may be due to the radar sampling at a beam height of approximately 0.2 km over the disdrometer. One potential explanation for this difference is larger drops within the broader beam of the radar may not be sampled by the smaller footprint of PIPS 2B, whereas the low concentration of these larger drops acts to positively-bias Z_H from SR1-P.

3.5 Discussion

Hurricane Laura provided a unique opportunity and novel dataset to quantify drop size distribution characteristics in different portions of a landfalling tropical cyclone using ground radar observations, space-borne radar retrievals, and disdrometer measurements. Prior research has examined the microphysical signatures in different regions of landfalling TCs using ground and space-borne radar observations (e.g., Didlake and Kumjian 2017b; Feng and Bell 2019; DeHart and Bell 2020; Homeyer

et al. 2021a; Brauer et al. 2021), however the use of disdrometer observations were not incorporated in order to verify PSD quantities and provide a direct comparison to estimations from remote sensing platforms as these retrievals were unavailable.

Ground radar observations from SR1-P exhibited the greatest increase in Z_H and Z_{DR} towards the surface below the melting layer from 0430-0700 UTC which are signatures of collision-coalescence dominant precipitation (e.g., Carr et al. 2017; Porcacchia et al. 2019). This occurred primarily in the inner core and western eyewall, and can be seen on both the composite RHI scans (Fig. 18d and 18e) and CVPs (Fig. 19a and 19b). Within the outer core and rainbands of Laura before 0330 UTC at the location of SR1-P, Z_H decreased with height below the melting layer while Z_{DR} increased slightly, which is consistent with evaporation and/or drop breakup (Fig. 19a and 19b). The GPM DPR overpass at 0301 UTC 27 August shows KuPR and D_M increasing towards the surface in the eyewall at an along-track distance of 100-175 km which is indicative of collision-coalescence and/or a balance between collision-coalescence and drop breakup (Fig. 20b and 20c). Further, in the region of the outer core at an along track distance of 200-300 km, KuPR remains constant below the 0^oC isotherm, indicating the presence of evaporation or drop breakup (Fig. 20b). PIPS 2B was located in proximity to the location of the along-track cross section from the DPR (Fig. 20a), and measured a D_M near 1.5 mm at the time of the overpass. This value of D_M is similar to the 1.75 mm that the DPR algorithm extracted at an along-track distance of 260 km (Fig. 20c). Further, the DPR algorithm estimated a

$log_{10}(N_W)$ value of 3.5 m^{-3} mm^{-1} at the same along-track distance which is higher than the $log_{10}(N_T)$ value of 2.5-3.0 m^{-3} which was observed at the same drop size of 1.0 mm by the PIPS (Fig. 20d and Fig. 25c), and temporally collocated with a $log_{10}(N_W)$ value of 3.5 m^{-3} mm^{-1} estimated by the PIPS (Fig. 26). This indicates that the DPR may be overestimating the drop number concentration in the outer core of Laura prior to landfall.

The post-landfall DPR overpass occurred at 1246 UTC 27 August (Fig. 21), shortly after PIPS 2A and PIPS 2B stopped operating near 1200 UTC. During this time, the inner core of Laura had progressed inland, with both disdrometers being situated in the outer rainband environment. Figure 21b illustrates that KuPR is primarily constant towards the surface within the warm cloud layer outside of the inner core, with D_M ranging from 1.5 to 2.0 mm (Fig. 21c) and $log_{10}(N_W)$ near 3.5 m^{-3} mm^{-1} (Fig. 21d). At an along-track distance of 200-260 km in the inner core, KuPR increased from 35 dBZ at 0^oC isotherm, to 50 dBZ near the surface, implying collision-coalescence and/or a balance between collision-coalescence and drop breakup. D_M also increased from 1.25-1.50 mm near the melting layer, to 1.75-2.00 mm near the surface with the highest values of $log_{10}(N_W)$ of 4.5 m^{-3} mm^{-1}. While the highest drop concentrations in the eyewall is consistent with prior studies (e.g., Didlake Jr. and Kumjian 2018; Homeyer et al. 2021a), the constant values of $log_{10}(N_w)$ is likely a non-physical assumption of the DPR PSD algorithm as hydrometeor concentration is known to change with height through vertical profiles of Z_H and K_{DP} (e.g., Carr et al.

2017; Brauer et al. 2020). Figure 22 displays the comparison of KuPR percentiles from the pre-landfall overpass and the post-landfall overpass. At the 75th and 95th percentiles, the increase in KuPR towards the surface at 0301 UTC is greater than the slopes at 1246 UTC. This suggests that the magnitude of collision-coalescence dominant precipitation decreased from pre-landfall to post-landfall, which is also reflected in the smaller D_M values < 1.0 mm after 0930 UTC 27 August that were observed by PIPS 2A and PIPS 2B, indicating the increased presence of drop breakup or evaporation (i.e., non-CC processes). Further, the highest values of $log_{10}(N_w)$ of 2.5-4.0 mm^{-3} occurred after 0900 UTC 27 August as well (Fig. 26), which is consistent with a higher magnitude of drop breakup and/or a balance between collision-coalescence and drop breakup, translating to a smaller mean drop size. While dominant precipitation processes in different portions of the storm are known to vary, both along-track cross-sections were computed through regions of the inner core and outer core, therefore the along-track percentiles of KuPR shown are consistent with showing a decrease in the frequency of collision-coalescence processes from pre-landfall to post-landfall (Fig. 22).

While there are limitations when comparing observations of Z_H and Z_{DR} from disdrometers to ground radars (i.e. such as radar beam height increasing with range), disdrometers have been historically used to calibrate remote sensing platforms (e.g., Martner 1977; Lee and Zawadzki 2006). As PIPS 2A was close in proximity to SR1-P, a time series of Z_H and Z_{DR} from the ground radar provides a direct comparison

between both observational platforms (Fig. 27, Fig. 28). As all PIPSs was located in the inner core and eyewall after 0530 UTC 27 August, the disdrometer observations estimated Z_H values of 35-50 dBZ, with the greatest values occurring from 0530-0730 UTC 27 August (Fig. 27). Additionally, SR1-P observed lower values of Z_H by approximately 3-5 dBZ over PIPS 1A, potentially due to additional drop growth via collision-coalescence below radar beam height measured by the PIPS, especially in the inner core region after 0500 UTC. This difference may also be caused by the Z_H T-matrix calculation from the raw PSD retrievals.

A comparison of Z_{DR} between SR1-P and the PIPSs (Fig. 28) illustrates additional differences. Z_{DR} initially ranged from 0.5-1.0 dB after 0330 UTC before increasing to as high as 1.5-2.0 dB at 0500 UTC in the inner core. These values are higher than SR1-P Z_{DR} values which primarily vary from 0.0-1.0 dB. The maximum SR1-P Z_{DR} values of 0.5-1.5 dB occurred after 0500 UTC as SR1-P sampled the eyewall. As Z_{DR} is independent of number concentration, this negative bias from SR1-P may be caused by additional drop growth towards the surface as the beam height from SR1-P is approximately 900 m above the surface from PIPS 1A, 100 m above the surface from PIPS 2A, and 200 m above the surface from PIPS 2B. This is an additional source of uncertainty when computing Z_{DR} from the PIPS observations.

3.6 Conclusions

The mobile ground-radar observations, two GPM DPR overpasses, and three disdrometers were able to sample Hurricane Laura before, during, and after landfall as it impacted southwestern Louisiana from 26-27 August 2020. Both SR1-P and the GPM DPR observed signatures associated with collision-coalescence before and during landfall, with Z_H, Z_{DR}, and KuPR all increasing towards the surface below the melting layer which is indicative of drop growth. The PIPS observed a gradual increase in drop size up to landfall as the inner core moved onshore, as D_M increased from 1.0 mm to as high as 4.0 mm in the eyewall, with values decreasing to below 1.0 mm post-landfall. The GPM DPR observed similar signatures of the magnitude of collision-coalescence decreasing from pre-landfall to post-landfall, with a decreasingly negative slope of KuPR at the 95th percentile within the warm cloud layer towards the surface, implying an increased presence of drop breakup between both overpasses. Additionally, the larger range in KuPR in addition to a deeper bright-band indicates that more convection was present in the pre-landfall overpass, whereas the post-landfall DPR overpass illustrated the presence of more stratiform precipitation with some embedded convection. It was also found that prior to landfall, the DPR algorithm may be overestimating $log_{10}(N_W)$ by 0.5-1.0 m^{-3} mm^{-1} in comparison to the PIPS, resulting in differences in drop number concentration between both retrieval methods. These results are similar to prior work from Huang et al. (2021) who compared DPR retrievals to disdrometer observations during the summer monsoon season in China.

One potential reason for the DPR PSD algorithm overestimating $log_{10}(N_w)$ compared to the PIPS is that the near-surface retrievals have been corrected for attenuation (`https://www.eorc.jaxa.jp/GPM/doc/algorithm/ATBD_DPR_V07A.pdf`). Future work can use disdrometer observations to correct for this assumption made by the DPR PSD algorithm to more accurately quantify D_M and $log_{10}(N_W)$ at the surface in TCs. Last, Z_H and Z_{DR} from the PIPS were larger than the SR1-P retrievals, which may be due to additional drop growth via collision-coalescence below radar beam height.

Although it is a challenging task to deploy a mobile radar and multiple disdrometers in a landfalling TC, future studies should examine similar observations from all retrieval methods in order to determine if similar differences and similarities exist in TCs between ground radars, space-borne radar, and disdrometers to obtain a larger sample size. Further, one could incorporate S-band radar observations if available, as the KLCH WSR-88D become non-operational shortly before landfall. One additional avenue for future work would be to quantify and compare the derived rainfall rates using the polarimetric ground radar observations, the DPR-derived surface rainfall rate, and precipitation rates derived from the PIPS retrievals. This work can also be used to improve the DPR PSD algorithm, particularly in TCs. An additional limitation of this study is that each retrieval method sampled different portions of the TC at different times, therefore a denser observation network would be ideal to collect observations at different locations to provide a more detailed sample of different drop

size distribution moments.

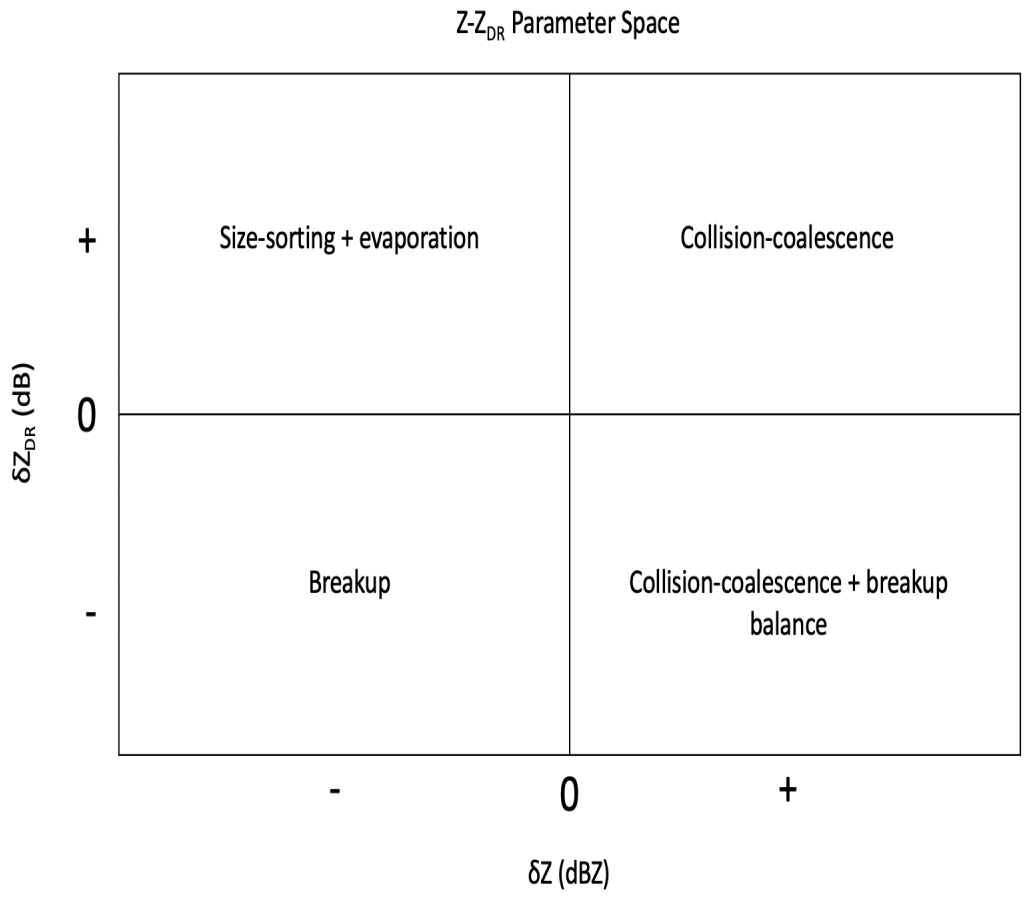

Figure 15: Z-Zdr Parameter Space developed by Kumjian et al. (2012) that uses vertical changes in Z_H and Z_{DR} within the warm cloud layer to identify dominant precipitation processes. Positive changes indicate values of Z_H and Z_{DR} increasing towards the surface below the melting layer.

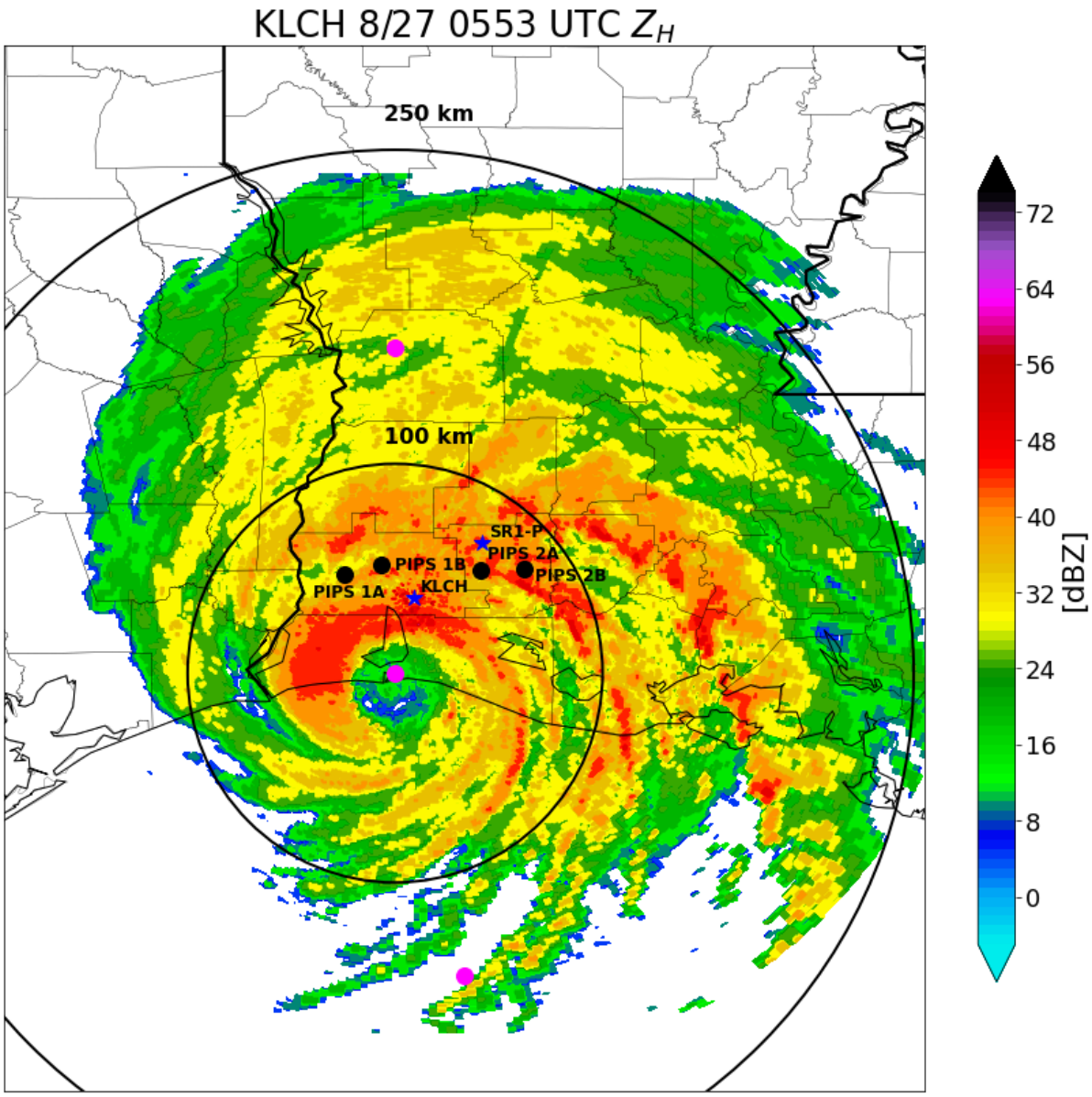

Figure 16: Raw image of 0.5^o Z_H at 0553 UTC 27 August, shortly before the KLCH WSR-88D went down. Overlaid are the locations of the 4 PIPS, SR1-P, and the KLCH WSR-88D. Additionally, HURDAT2 best track points are shown in magenta to illustrate the track of Laura (HURDAT). The 100 km and 250 km range rings are centered on the storm center at the time of the PPI.

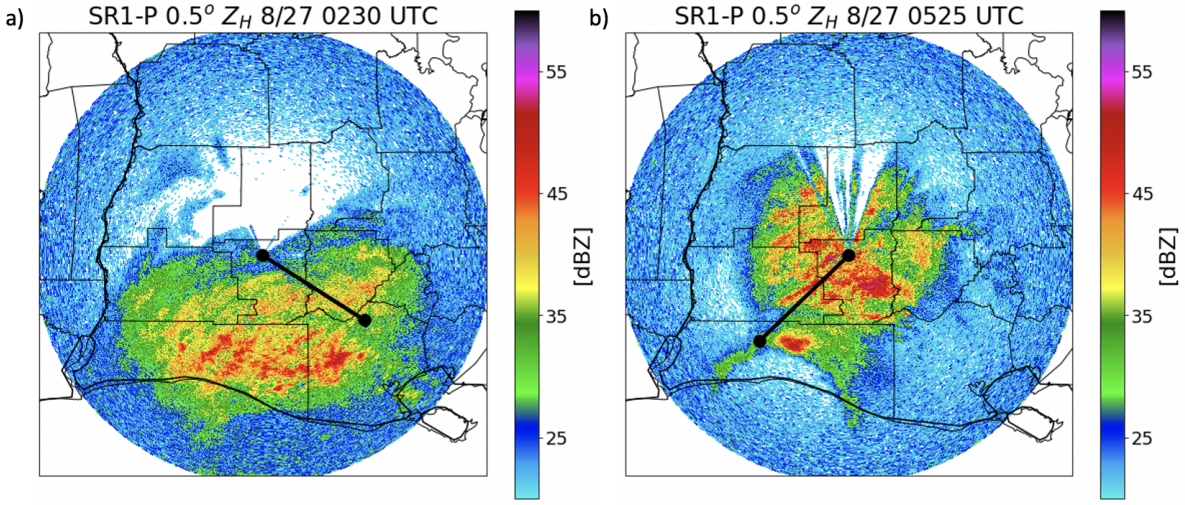

Figure 17: PPIs of Z_H from SR1-P at 0230 UTC (a) and 0525 UTC (b) on 27 August during the times of both RHI composites in Figure 4. The black lines denote the locations of each RHI cross-section of 70 km.

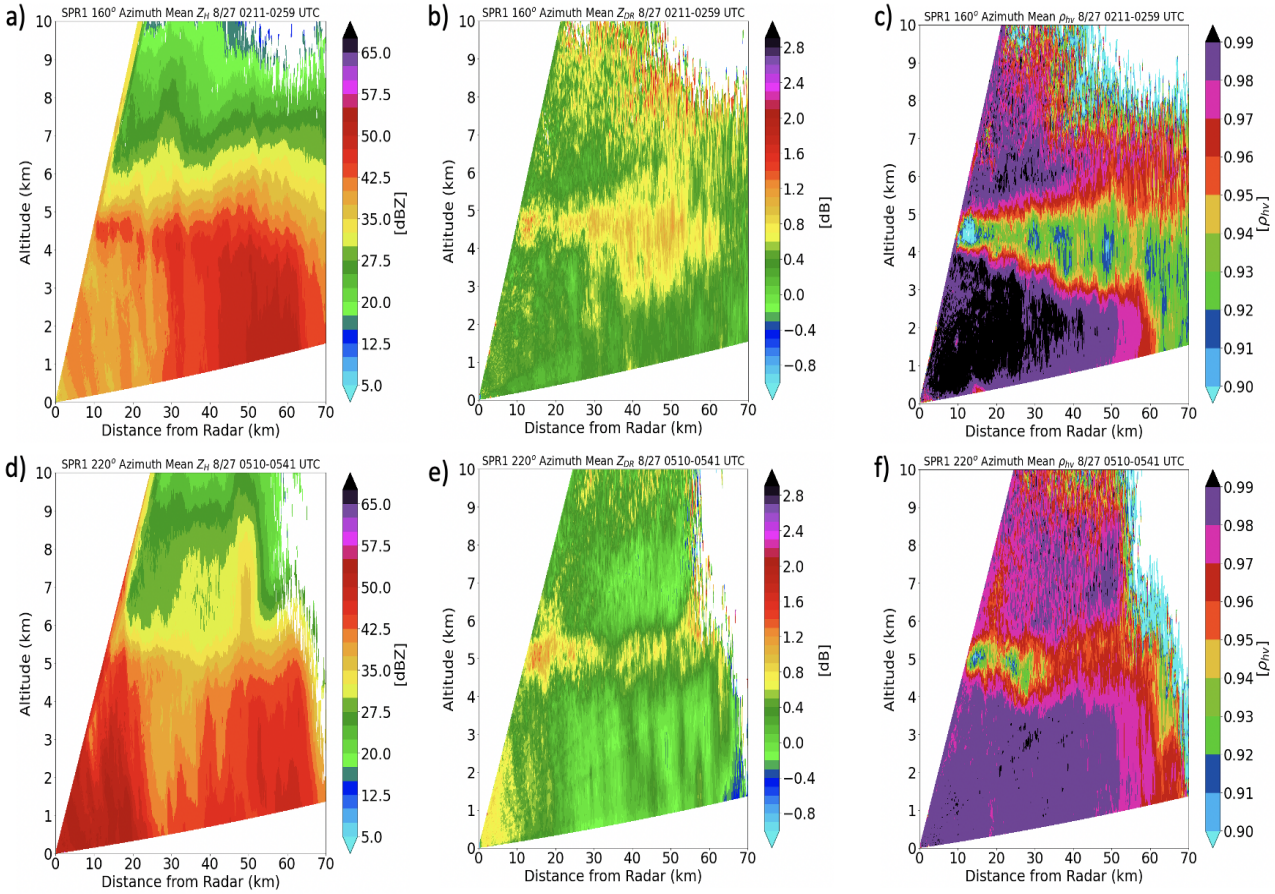

Figure 18: Time averaged mean Z_H, Z_{DR}, and ρ_{hv} from SR1-P at an azimuth angle of 160° from 0211-0259 UTC on 27 August (a) and at an azimuth angle of 220° at 0510-0541 UTC on 27 August (b). Precipitation processes are inferred from the change in Z_H and Z_{DR} towards the surface below the melting layer.

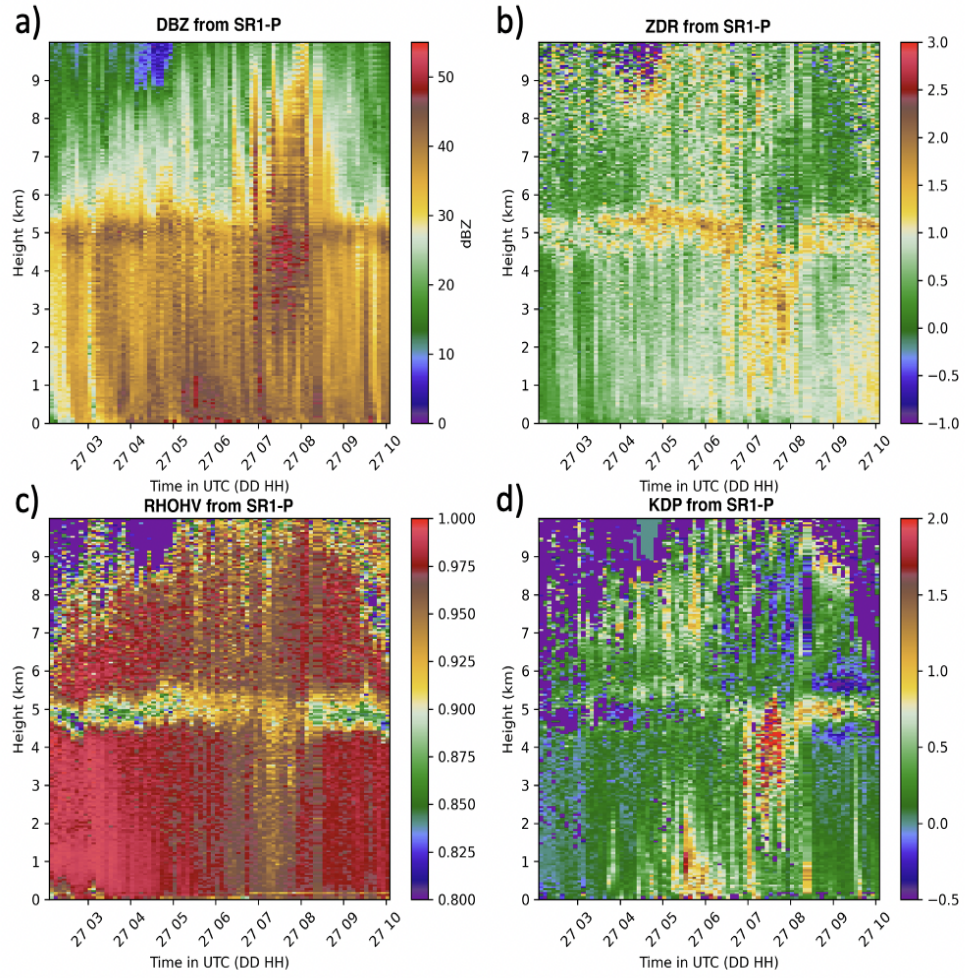

Figure 19: Columnar-vertical profiles (CVPs) of Z_H, Z_{DR}, ρ_{hv}, and K_{DP} from SR1-P from 0200-1000 UTC 27 August. Precipitation processes are inferred from the change in Z_H and Z_{DR} towards the surface below the melting layer, with increases towards the surface implying collision-coalescence.

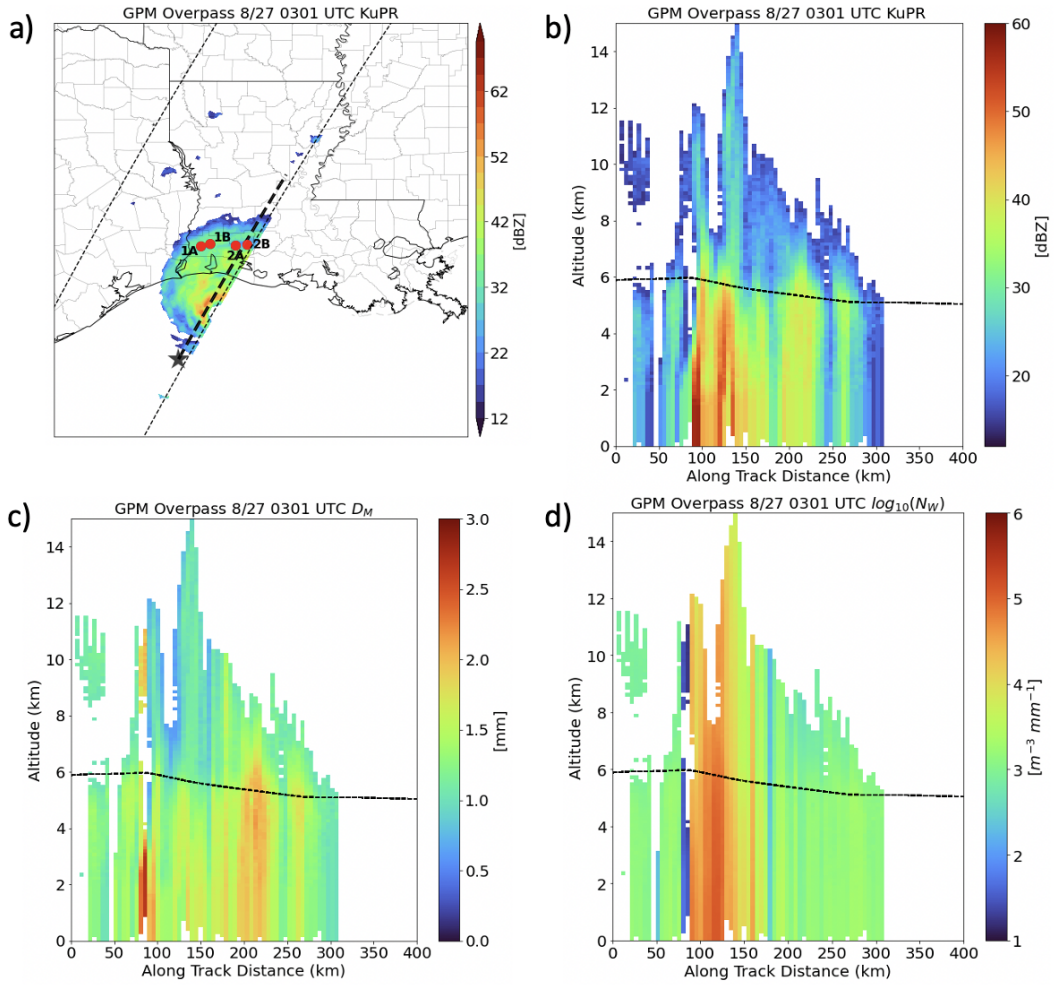

Figure 20: GPM DPR overpass at 0301 UTC 27 August (pre-landfall) showing attenuation-corrected near surface Ku-band reflectivity and PIPSs locations (a), vertical profiles of Ku-band reflectivity (b), mean drop diameter (c), and normalized intercept parameter (d). Vertical cross-sections are taken along track from the star. The dashed black line represents the 0^oC isotherm.

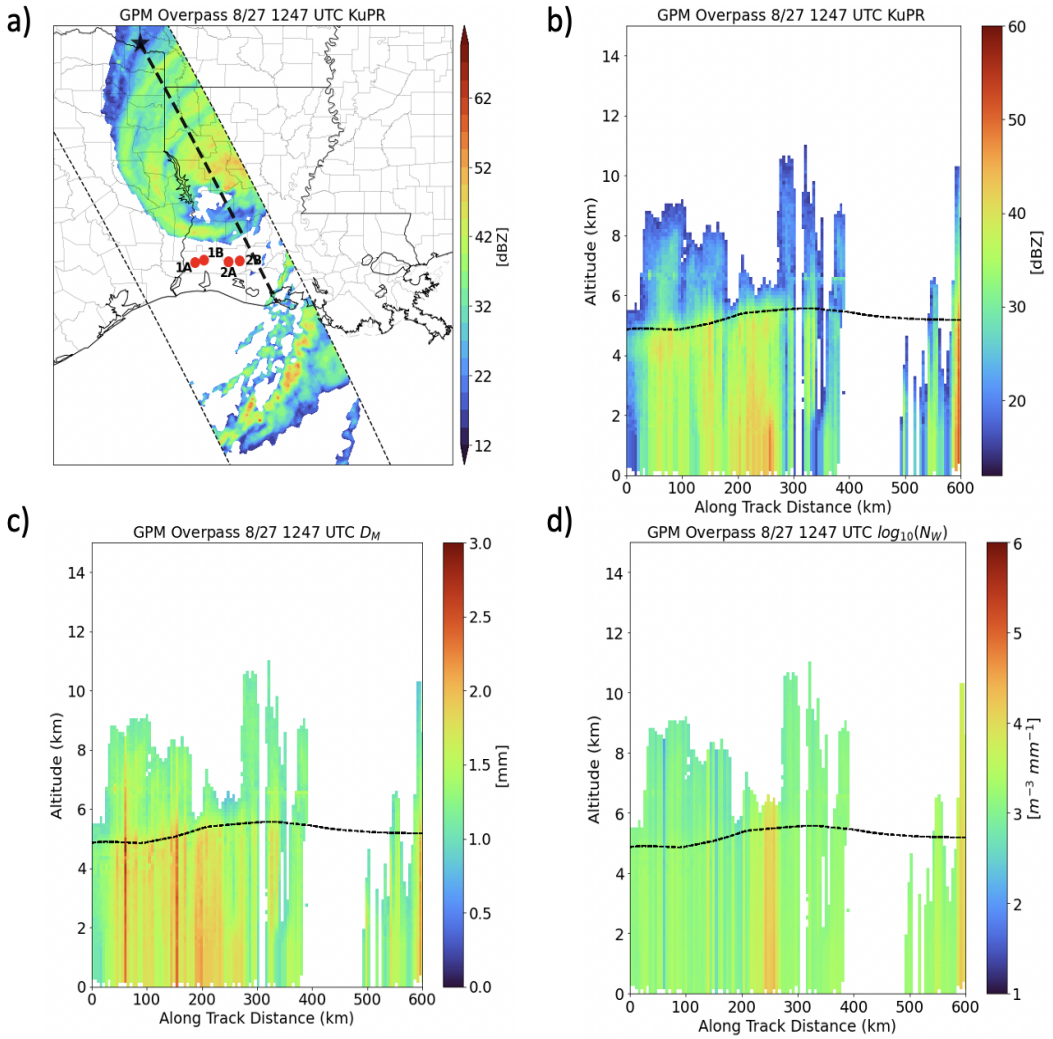

Figure 21: GPM DPR overpass at 1246 UTC 27 August (post-landfall) showing attenuation-corrected near surface Ku-band reflectivity and PIPSs locations (a), vertical profiles of Ku-band reflectivity (b), mean drop diameter (c), and normalized intercept parameter (d). Vertical cross-sections are taken along track from the star. The dashed black line represents the 0^oC isotherm.

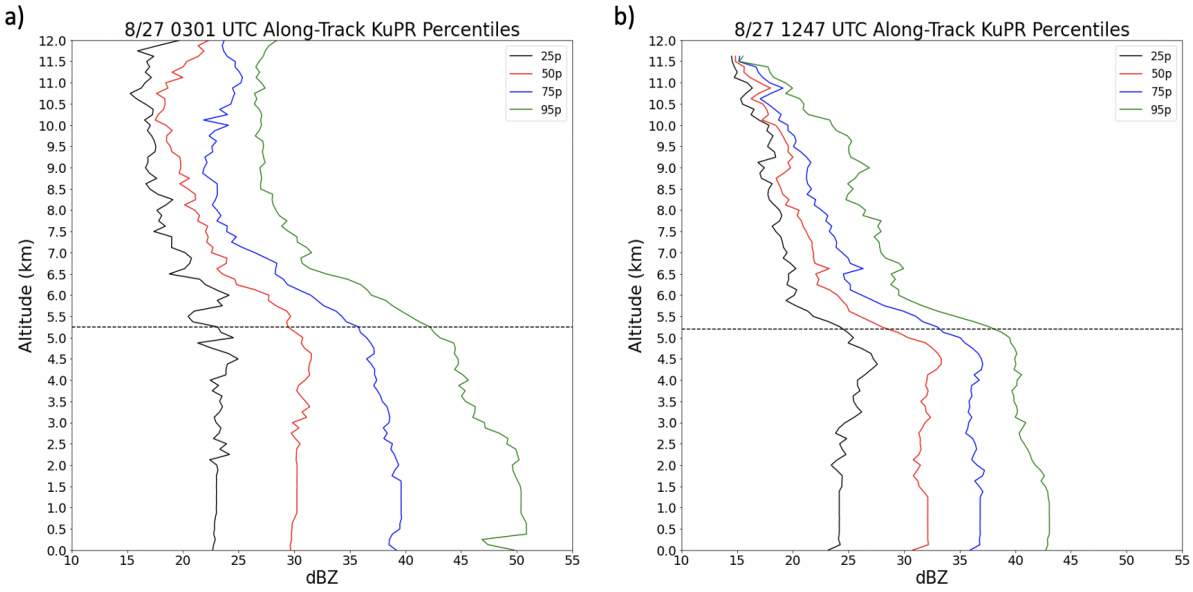

Figure 22: Along-track quantiles of KuPR at 0301 UTC 27 August pre-landfall (a) and 1246 UTC 27 August post-landfall (b). The dashed line represents the along-track mean 0^oC isotherm.

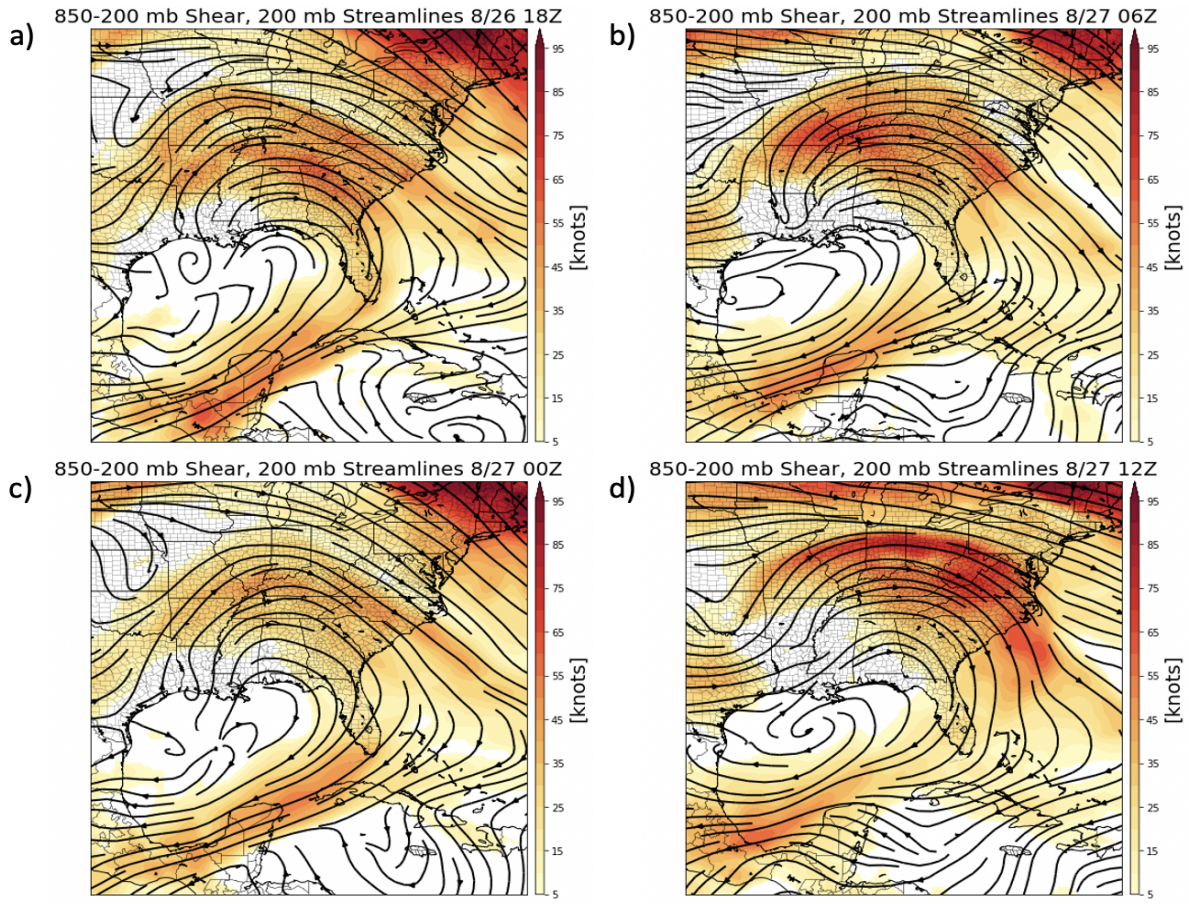

Figure 23: 850-200 mb environmental wind shear and 200 mb streamlines from 1800 UTC 26 August to 1200 UTC 27 August.

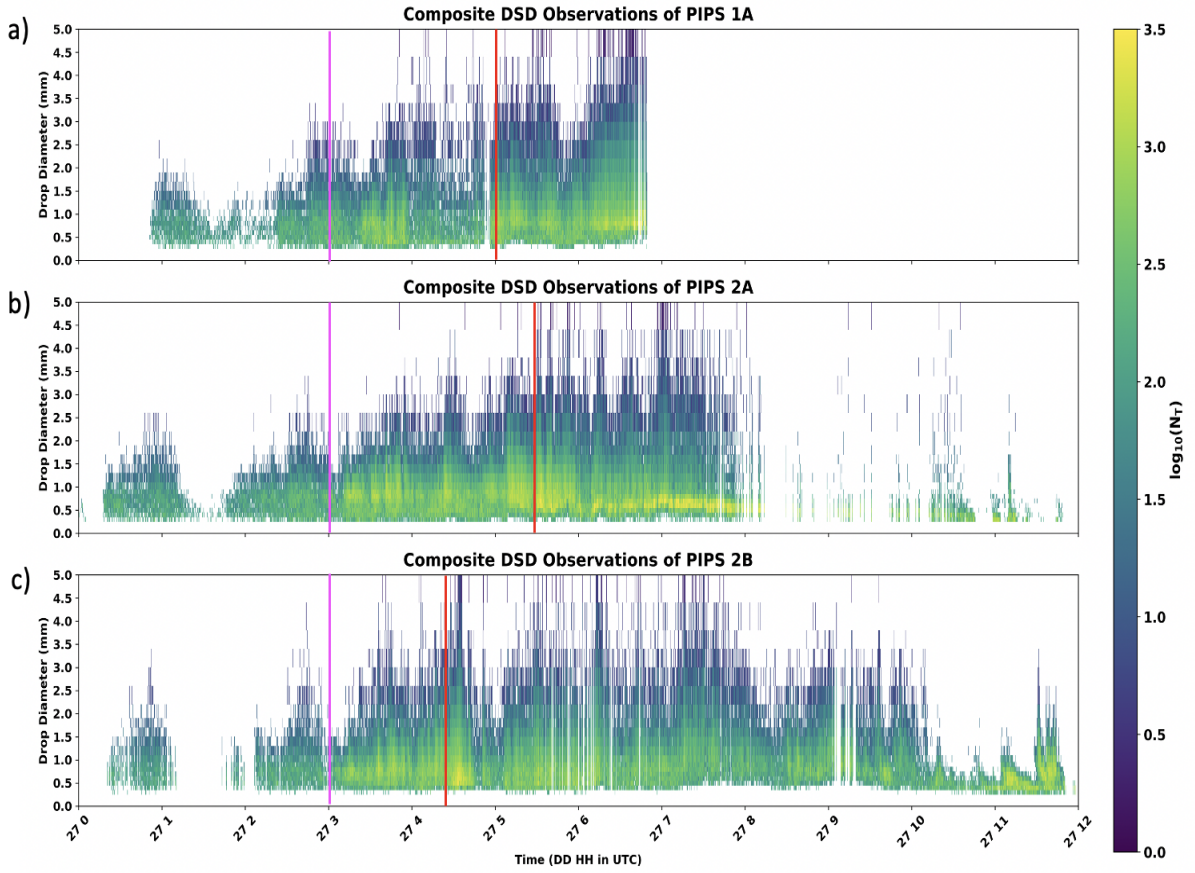

Figure 24: Drop diameter and $log_{10}(N_T)$ from PIPS 1A (a), 2A (b), and 2B (c) from 2000 UTC 26 August to 1200 UTC 27 August. The red line represents the separation of the outer core from the inner core while the magenta line represents the time of the pre-landfall GPM DPR overpass (0301 UTC).

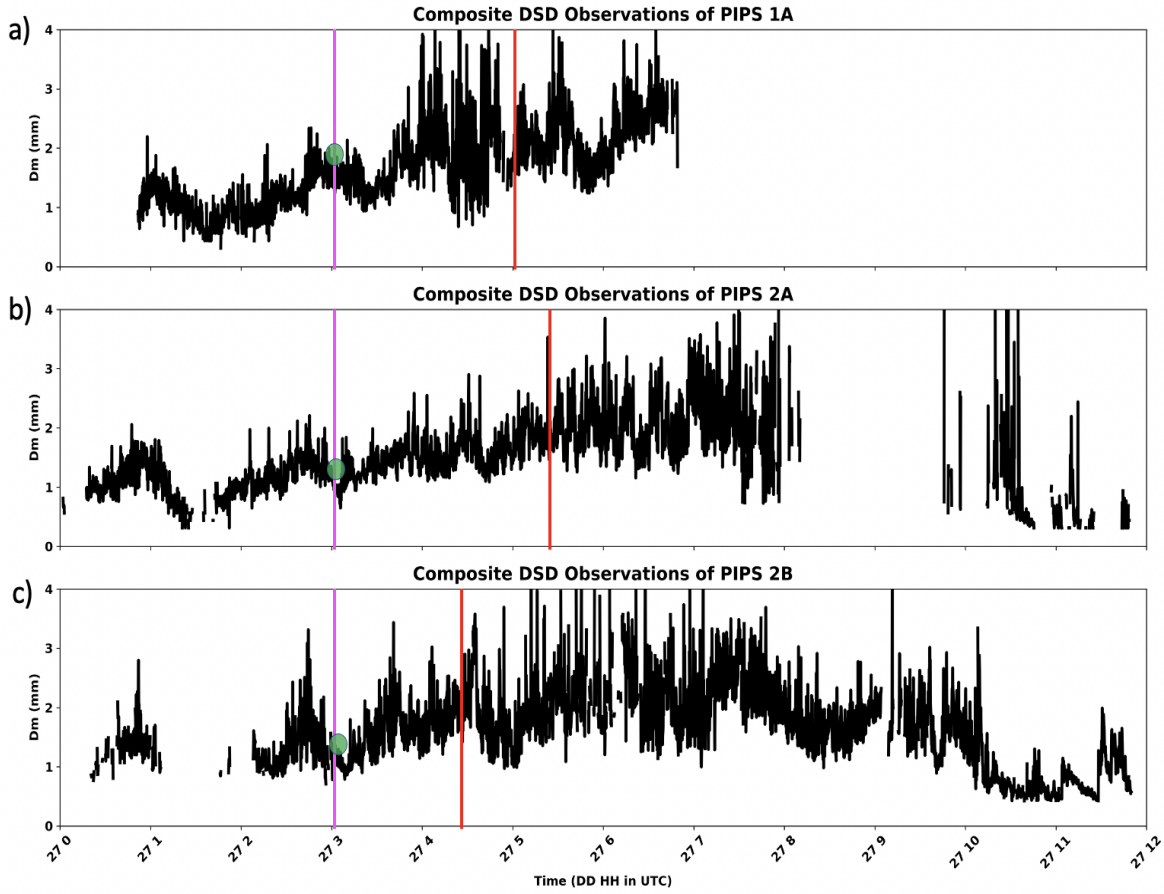

Figure 25: D_M from PIPS 1A (a), 2A (b), and 2B (c) from 2000 UTC 26 August to 1200 UTC 27 August. The red line represents the separation of the outer core from the inner core while the magenta line represents the time of the pre-landfall GPM DPR overpass (0301 UTC). The green cirles represent the near-surface value of D_M from the pre-landfall GPM DPR overpass.

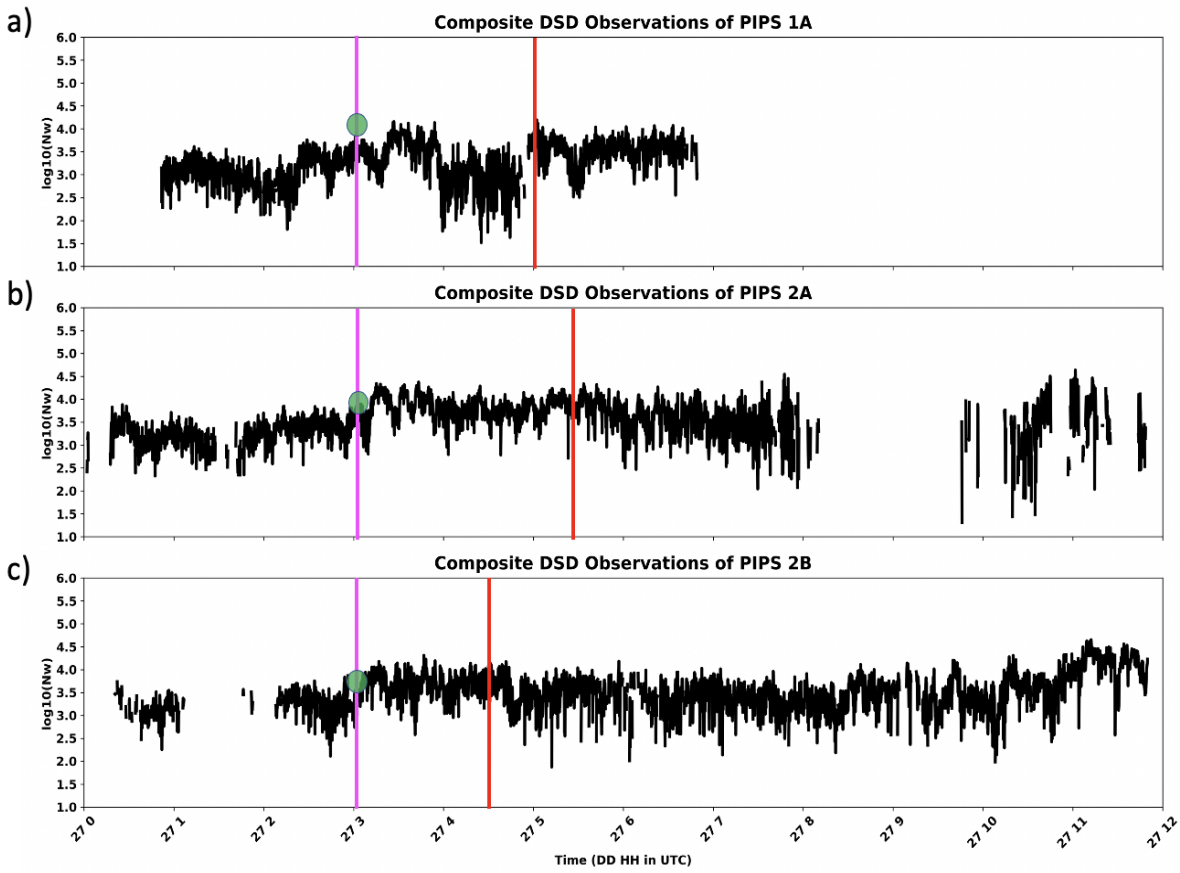

Figure 26: $log_{10}(N_W)$ from PIPS 1A (a), 2A (b), and 2B (c) from 2000 UTC 26 August to 1200 UTC 27 August. The red line represents the separation of the outer core from the inner core while the magenta line represents the time of the pre-landfall GPM DPR overpass (0301 UTC). The green cirles represent the near-surface value of $log_{10}(N_W)$ from the pre-landfall GPM DPR overpass.

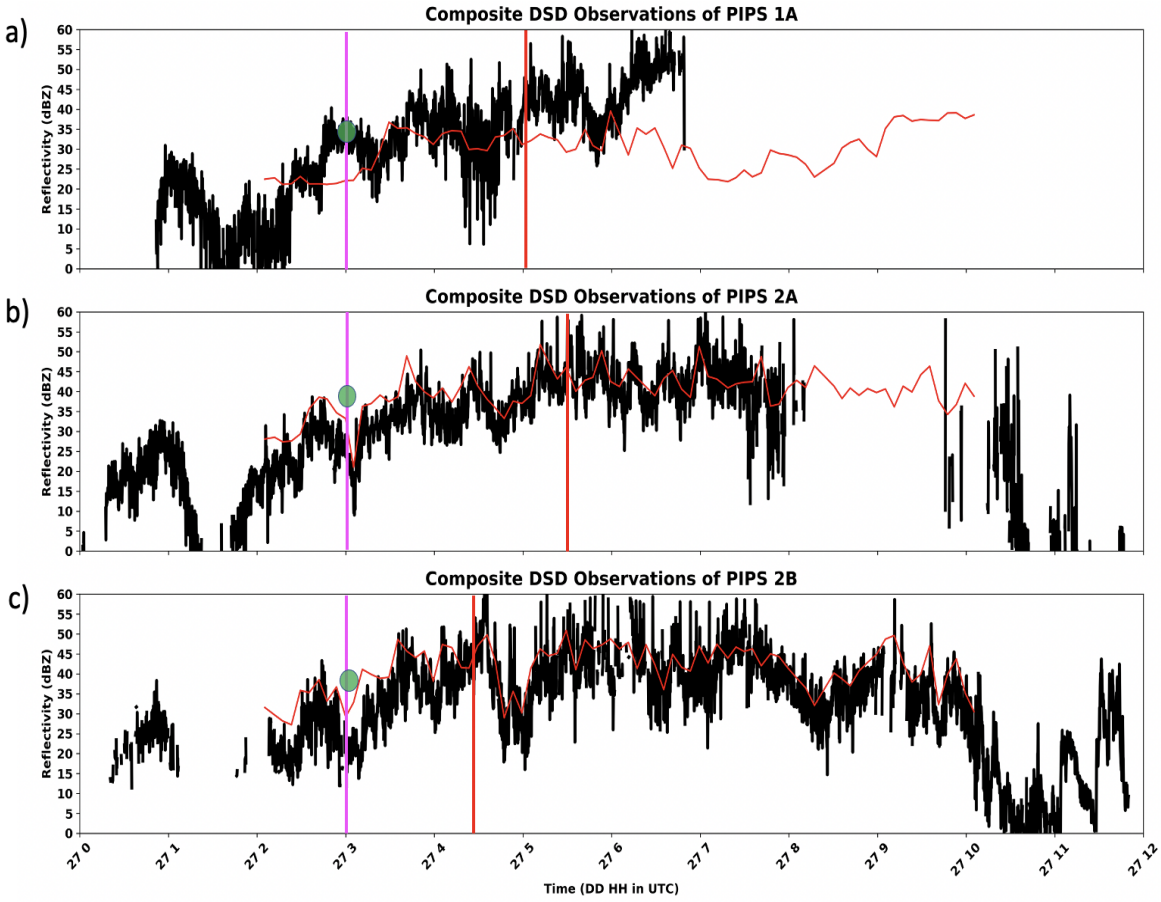

Figure 27: Z_H from PIPS 1A (a), 2A (b), and 2B (c) from 2000 UTC 26 August to 1200 UTC 27 August. The red line represents the separation of the outer core from the inner core while the magenta line represents the time of the pre-landfall GPM DPR overpass (0301 UTC). The green cirles represents the near-surface value of KuPR from the pre-landfall GPM DPR overpass. The thin red line indicates Z_H from SR1-P over the location of each corresponding PIPS.

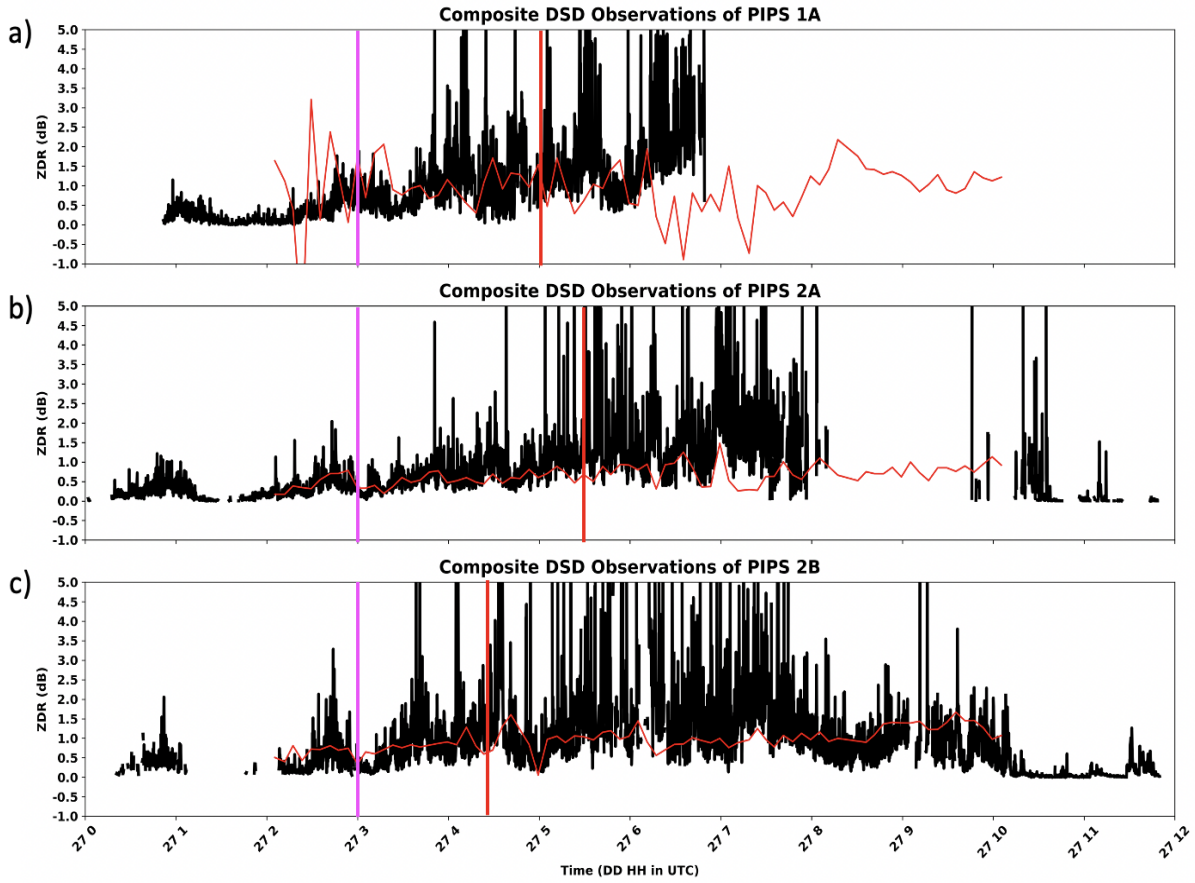

Figure 28: Z_{DR} from PIPS 1A, 2A, and 2B from 2000 UTC 26 August to 1200 UTC 27 August. The red line represents the separation of the outer core from the inner core while the magenta line represents the time of the pre-landfall GPM DPR overpass (0301 UTC). The thin red line indicates Z_{DR} from SR1-P over the location of each corresponding PIPS.

Table 1: Table with PIPS locations, and starting time

PIPS Number	Latitude	Longitude	Starting Time
PIPS1A	30.224910	-93.518746	1942 UTC
PIPS1B	30.26642	-93.359979	2019 UTC
PIPS2A	30.245168	-92.928744	2206 UTC
PIPS2B	30.246739	-92.739726	2148 UTC

4 Chapter 4: Precipitation Microphysics in Tropical Cyclones: A Global Perspective

4.1 Introduction

Excessive precipitation in landfalling TCs poses a threat to life and property (Rappaport 2014), and plays a key role in the Earth's water cycle (Franco-Díaz et al. 2019). TCs can be particularly destructive if landfall occurs in low-lying areas prone to storm surge and long-duration flooding (e.g., Mori et al. 2014; Brauer et al. 2020; Islam Fahim et al. 2021). Further, TCs have an impact on the global radiation budget since they release large quantities of latent heat through deep moist convection (Kuo 1965), resulting in upper-tropospheric outgoing longwave radiation (Smith and Toumi 2020). Last, precipitation processes and structure are often misrepresented in numerical models which poses an additional challenge in forecasting operations (e.g, McFarquhar et al. 2006; Chen and Gopalakrishnan 2014; Hristova-Veleva et al. 2021). Thus, it is important to better understand cloud and precipitation physics in TCs.

Precipitation processes in TCs are largely tied to characteristics of the synoptic-scale environment such as 850-200 mb vertical wind shear, mid-level relative humidity, storm motion, and ocean heat content (e.g., Gray 1968; DeMaria et al. 2001). After tropical cyclogenesis and the formation of a radius of maximum wind, precipitation microphysics in the inner core, principal rainband, and eyewall are dictated by the cyclonic vortex whereas the outer rainband precipitation characteristics are

more dependent on the large-scale ambient environment (Houze 2010). Wingo and Cecil (2010) determined that eyewall asymmetries are dependent on the magnitude of the deep-layer shear vector in addition to TC intensity, with the largest asymmetries occurring in instances of strong shear, with strong TCs being more resilient to environmental vertical wind shear. Additionally, Lonfat et al. (2004) found that TC asymmetries are also a function of geographic location and storm intensity. It has been observed that warm rain processes such as collision-coalescence and drop breakup are most prevalent in the eyewall, where hydrometeors can fall out of the TC before transitioning to the ice-phase aloft (Marks and Houze 1987). However ice-phase processes do exist in this region of the TC, where graupel formation can occur and melt to form rain below the freezing level (Houze 2010). Further, aggregates are also typically present in the eyewall, and can get advected further downwind at greater radii by outflow (Black and Hallett 1986). These ice particles contribute to seeder-feeder processes in areas outside the eyewall, and lead to the presence of a bright-band in stratiform precipitation as they melt below the freezing level (Jorgensen 1984; Black and Hallett 1986). Supercooled liquid water content is typically lower in a TC compared to mid-latitude precipitation systems and is found primarily on the inner edge of the eyewall within the -5^oC - 0^oC layer (e.g., Black and Hallett 1986; Houze 2010; Laurencin et al. 2020a).

Numerous field campaigns have been conducted to better understand precipitation structure and processes in TCs, often using aircraft observations and airborne radar

(e.g., Marks and Houze 1984; Marks and Houze 1987; Aberson et al. 2006). Marks and Houze (1987) analyzed precipitation trajectories in Hurricane Alicia (1983) using airborne radar reflectivity data and determined that 30-50% of the precipitation in TCs is stratiform. Jorgensen and Willis (1982) collected hydrometeor size observations to determine a more representative Z-R relationship in TCs, and found that the most representative expression to estimate rainfall rates in a TC is $Z = 300R^{1.5}$. While in-situ and airborne radar observations of precipitation in TCs are useful for understanding precipitation microphysics, it is expensive and logistically difficult to sample TCs on a global scale using this sampling method, making other remote sensing techniques more practical.

Observing TCs at all phases is a challenge as ground radar networks are non-existent over the open ocean, and can be lacking in spatial coverage over much of the Earth's landmasses, making satellite-borne radar retrievals useful for sampling precipitation globally (Simpson et al. 1996; Hou et al. 2014; Skofronick-Jackson et al. 2017). Prior work from Porcacchia et al. (2019) used vertical profiles of KuPR and KaPR from the NASA Global Precipitation Measurement (GPM) mission dual-frequency precipitation radar (DPR) to diagnose cloud properties to infer the presence of collision-coalescence (CC) or non-collision coalescence dominant precipitation (i.e. drop breakup) below the 0^oC isotherm. They found that CC events are associated with negative slopes of KuPR and KaPR towards the surface, whereas non-CC events are characterized by positive slopes of KuPR/KaPR in the same layer. This is sim-

ilar to the approach used by Carr et al. (2017) that used vertical profiles of radar reflectivity factor (Z_H) and differential reflectivity (Z_{DR}) from ground-based S-band radars to diagnose CC and non-CC events in the United States.

Specifically focusing on radar observations in TCs, Houze (2010) analyzed CFADs of reflectivity from the NASA Tropical Rainfall Measurement Mission (TRMM) KuPR in five TCs, and found a mixture of convective and stratiform precipitation elements in the eyewall, inner core region, and outer rainband environment. Further, the eyewall CFAD illustrates a distribution that is clustered around the mode in KuPR, while the outer rainband CFAD shows the greatest range in reflectivity. Using the GPM DPR, Huang and Chen (2019) analyzed four years of TCs in the Northwestern Pacific Ocean and found a positive correlation between high precipitation efficiency and increases in KuPR and mass-weighted mean drop diameter (D_M) towards the surface within the warm cloud layer which is consistent with CC-dominant precipitation (e.g., Carr et al. 2017; Porcacchia et al. 2019; Brauer et al. 2021). Further, both Didlake Jr. and Kumjian (2018) and Laurencin et al. (2020b) investigated S-band polarimetric radar signatures in Hurricanes Matthew (2016) and Irma (2017), and found size-sorting signatures in the left and right front quadrants of the eyewall with large concentrations of smaller drops being advected cyclonically by the vortex. The combination of ground-based and space-borne radar observations has led to an improved understanding of TC dynamics and dominant precipitation processes in various parts of the storm.

Understanding the structure and evolution of precipitation processes in TCs is crucial as they can produce catastrophic flooding in highly populated regions. Thus, an improved understanding of precipitation structure in TCs will allow for more accurate numerical simulations and forecasting of precipitation in these events (Fovell and Su 2007; Hristova-Veleva et al. 2021). This study will offer a novel approach to analyzing TCs before, during, and after landfall on a global scale using the GPM DPR to investigate vertical profiles of KuPR to gain insight into dominant precipitation processes in each event. Thus, it is hypothesized that the aforementioned precipitation processes will vary at different distances in the TC, will vary in each 850-250 hPa shear-relative quadrant, and by TC ocean basin. One potential reason for the global variation in precipitation microphysics in TCs is the spatial and seasonal variability in 850-200 hPa vertical wind shear and total integrated tropospheric moisture (e.g., Kimball 2006; Wingo and Cecil 2010; Wu et al. 2015). Further, in a shear-relative framework, it is hypothesized that the maximum sample size of KuPR profiles in the eyewall will be in the downshear left quadrant, as this area typically experiences a maximum in rainfall reagrdless of the magnitude of environmental vertical wind shear (e.g., Chen et al. 2006; Houze 2010).

4.2 Data and Methods

4.2.1 IBTrACS and SHIPS

To determine the time, location, and intensity of all TCs between 2014-2020 on a global scale, the International Best Track Archive for Climate Stewardship (IBTrACS) database was used (Knapp et al. 2010; Knapp, Kenneth R. and Diamond, Howard J. and Kossin, James P. and Kruck, Michael C. and Schreck, Carl J. III 2018). After each TC has dissipated, IBTrACS uses storm reports from sources such as buoys, aircraft, and ground radar to estimate storm center location and intensity in 3 hour increments (Knapp, Kenneth R. and Diamond, Howard J. and Kossin, James P. and Kruck, Michael C. and Schreck, Carl J. III 2018). The IBTrACS database includes all TCs from 1840-present. More information on the IBTrACS algorithm to estimate storm characteristics can be found at `https://www.ncei.noaa.gov/products/international-best-track-archive?name=bib`. The SHIPS shear vector orientation that was chosen for each event corresponds to the time closest to the GPM DPR overpass and the point closest to the IBTrACS coordinates.

4.2.2 GPM DPR

DPR overpasses were matched with TC track points within 3 hours of each IBTrACS data point from 2014-2020 using PyOrbital (Crew 2018), with points over land and locations poleward of 45° N/S neglected in order to minimize potential extratropical and land interaction characteristics. As some overpasses occurred between IbTrACS

coordinates, the closest time was used in conjunction with the DPR overpass in order to avoid duplicate cases. Only cases where the difference between the DPR overpass time and the IBTrACS storm center time was less than 0.5 hours were retained. The distribution of time differences between the IBTrACS storm center and GPM DPR overpass coordinates are displayed in Figure 29. Vertical profiles of along-track attenuation-corrected KuPR at all 49 angles were collected in each shear-relative quadrant of all TCs when available to gain insight into dominant precipitation processes and how precipitation characteristics vary by TC basin. When shear vector data were unavailable, each storm was partitioned into the eyewall region ($< 15km$), inner core region ($< 60km$) relative to the storm center. Although the radius of maximum wind is known to vary by storm, an objective, non-adaptive method was chosen to partition each storm into each region to minimize subjective biases and potential subtleties in TC structure that the DPR was unable to capture.

CC-dominant precipitation was identified by profiles were KuPR increased towards the surface below the melting layer (e.g., Porcacchia et al. 2019; Brauer et al. 2021). Further non-CC profiles (i.e. drop breakup, size-sorting, and evaporation) were characterized when KuPR decreases towards the surface within the warm cloud layer. In each case, the warm cloud layer was defined as the -1 to -3 km layer that was normalized with respect to the GPM DPR estimated 0^oC isotherm. This layer was chosen to reduce contamination from the bright-band above and the clutter region (due to attenuation) below. To quantify ice-phase microphysical processes, vertical

slopes of KuPR in the normalized altitude layer of 1 to 4 km were computed and plotted as probability density functions (PDFs). To better quantify the dominant precipitation processes in different regions of each TC, a linear regression was performed within the warm cloud layer and the ice-phase precipitation layer to determine the slope of KuPR. Cases were omitted in this analysis when the DPR overpass failed to sample any portion of the inner core. The following number of samples cases from each TC region and shear-relative quadrant are presented in Table 2.

Once all slopes were computed for both types of cases, PDFs were plotted to illustrate the variability of KuPR in different TC annului and shear-relative quadrants and how they vary by TC ocean basin. To quantify the vertical extent of precipitation in each shear-relative quadrant of TCs, PDFs of echo top heights from the GPM DPR algorithm were also illustrated to provide a comparison between each ocean basin. In the DPR algorithm, echo top heights are derived from the highest range bin where KuPR is detected beyond the sensitivity of 18 dBZ.

4.2.3 ERA-5

ECMWF ERA-5 data was used to plot boreal winter (DJF) and summer (JJA) composites of total integrated water vapor and 850-200 mb wind shear from 2014-2020 to quantify the seasonal and global variation in variables that can influence TC structure and evolution. ERA-5 data has 137 vertical levels, a 3 hour temporal resolution, and a horizontal grid spacing of 37 km (Hersbach et al. 2019b).

4.3 Results

4.3.1 Large-Scale Environmental Influences on TC Structure and Precipitation Processes

Figure 30 illustrates the collocation of each GPM DPR overpass with the IBTrACS TC center database for all cases with 850-200 hPa wind shear data provided by the SHIPS database (Fig. 30a) and for all cases where shear data is not available (Fig. 30b), where cases were identified and analyzed based off storm annuli and distance from the TC center. Each DPR overpass was partitioned into 6 ocean basins: East-Central Pacific Ocean (ECPAC), Southern Pacific Ocean (SPAC), Atlantic Ocean (ATL), Northern Indian Ocean (NIND), Southern Indian Ocean (SIND), and Northwest Pacific Ocean (NWPAC). It can be seen that the majority of TC cases sampled by the DPR occurred in the Northwest Pacific (17 cases) and East-Central Pacific (13 cases) ocean basins. This is partially consistent with observations of TCs from the Tropical Rainfall Measurement Mission (TRMM) (Jiang et al. 2011) who investigated the temporal climatology of rainfall in TCs globally. To advance this work and to better understand how TC structure and microphysics vary globally, Figure 31 shows seasonal composites of mean total integrated water vapor (TWV) from 2014-2020 during the boreal winter (Fig. 31a) and boreal summer (Fig. 31b). It is evident that during the boreal winter, the SPAC region generally experiences higher values of TWV (55 $kg\ m^{-2}$) compared to the SIND region that typically sees values of 50 $kg\ m^{-2}$ or lower. During boreal summer, mean TWV is maximized from 55-60 $kg\ m^{-2}$

in eastern portions of the NIND basin, western portions of the NWPAC basin, and in the southeastern ECPAC basin, particularly along the intertropical convergence zone. There is an evident contrast between these regions of relatively high TWV and a region of lower TWV in the ATL ocean basin, ranging from 45-50 $kg\ m^{-2}$ indicating lower values of tropospheric moisture. These drier conditions are known to have an impact on TC development, structure, and evolution as areas of enhanced TWV relative to the storm center are known to produce asymmetries in the inner core region (e.g., Kimball 2006; Wu et al. 2015). For this reason and as it was more broadly stated in the introduction, vertical profiles of KuPR in regions of greater TWV are hypothesized to be more consistent with CC-dominant precipitation, whereas regions of lower TPW are expected to have more profiles reflective of non-CC precipitation (i.e. evaporation and drop breakup). Further, as prior studies have shown, 850-200 hPa vertical wind shear is also known to largely influence TC structure, especially asymmetries in the inner core and ultimately precipitation processes (e.g., Knaff et al. 2004; Wingo and Cecil 2010; Didlake Jr. and Kumjian 2018; Laurencin et al. 2020b).

Figure 32 shows seasonal composites of 850-200 hPa vertical wind shear during boreal winter (Fig. 32a) and boreal summer (Fig. 32b). During boreal winter and Southern Hemisphere TC season (Pillay and Fitchett 2021), mean deep-layer vertical wind shear primarily ranges from 5-25 knots across all ocean basins, particularly between 15^oN and 25^oS. One exception is the eastern portion of the SPAC basin, where 850-200 hPa shear typically exceeds 25 knots, which is unfavorable for TCgenesis

(e.g., Elsberry and Jeffries 1996). This region also typically experiences sea-surface temperatures below the 27^oC threshold necessary for TC formation (e.g., Song and Zhang 2016), which explains why there are no TCs in this portion of the SPAC ocean basin in the GPM DPR dataset. During the boreal summer (Fig. 32b), both the EC-PAC and ATL basins typically experience shear ranging from 10-25 knots, where the region around the Hawaiian Islands and northeast towards California climatologically has higher vertical wind shear in excess of 25 knots.

4.3.2 Annulus Cases

As 850-200 hPa shear data were unavailable for 31 of the 59 total cases, annuli vertical profiles of KuPR in the liquid phase were investigated and partitioned into 4 different regions relative to the TC center: Eyewall ($<$ 15 km), inner core (15 km $<$ 60 km), outer core (60 km $<$ 115 km) and outer rainbands (115 km $<$ 200 km). While these different regions will certainly vary by TC precipitation structure and asymmetries (e.g., Chen et al. 2006; Wingo and Cecil 2010; Didlake Jr. and Kumjian 2018), a fixed objective and automated methodology was chosen for this analysis, thus being one limitation of this work.

PDFs of vertical slopes of attenuation-corrected KuPR (Fig. 33a-33b) and uncorrected KuPR in the liquid phase were plotted to show potential differences of how the DPR attenuation-correction algorithm influences the distributions of vertical slopes of KuPR (Fig. 33c-33d). The mode for CC-dominant precipitation in the eyewall

for the attenuation-corrected profiles of KuPR in the eyewall is -0.35 dBZ km^{-1}. For non-CC dominant precipitation (i.e. drop breakup or evaporation), the mode is 0.4-0.5 dBZ km^{-1}. The ocean basins with the highest density of CC-dominant profiles of KuPR are the NWPAC and ATL ocean basins, whereas the highest density of non-CC dominant profiles fall within the NIND and SIND basins. In the inner core region of all TCs examined, the mode associated with CC-dominant precipitation is -0.30 dBZ km^{-1} in addition to a lower magnitude of mode associated with non-CC dominant precipitation of 0.45 dBZ km^{-1}.

When comparing the attenuation-corrected profiles to the uncorrected profiles (Fig. 33c-33d), the eyewall shows the bimodal distribution being skewed towards positive slopes of KuPR implying non-CC dominant precipitation, with the exception of the ATL and SPAC basins which still tend to have a mode of -0.40 dBZ km^{-1} and -0.05 dBZ km^{-1} respectively. Both the NIND and SIND basins have a mode characterized by positive slopes of KuPR ranging from 0.30-0.35 dBZ km^{-1}, indicating the increased presence of evaporation and drop breakup. In the inner core region (Fig. 33d), the distributions are largely bimodal, with the SIND basin having a mode of -0.20 dBZ km^{-1}. However, the overall distribution suggests that a combination of CC and non-CC processes are prominent at this range from the storm center.

A direct comparison between the eyewall and the inner core region shows a similar bimodal distribution, with the eyewall region containing greater maxima of positive slopes compared to negative slopes, particularly in the NIND and SIND basins. In

the inner core region, all TC ocean basins have a primary mode of -0.25 dBZ km^{-1} with the exception of the NIND basin in the liquid phase which is uniformly distributed with a mode of 0 dBZ km^{-1}.

Figure 34 displays PDFs of the vertical slope of attenuation-corrected KuPR in the ice phase for all annuli cases and TC ocean basins for both the eyewall (Fig. 34a) and inner core (Fig. 34b) regions of all storms. As all annuli show bimodal distributions of KuPR slopes, this implies that each region of the storm experiences a mixture of processes resulting in hydrometeor growth (i.e. aggregation, riming, and deposition) and reduction in hydrometeor size (i.e. ice multiplication or sublimation) (Porcacchia et al. 2019). When examining closely, the mode amongst all distributions in the eyewall (Fig. 34a) occurs at approximately -0.35 dBZ km^{-1}, except for the NIND cases where the mode is around 0.3 dBZ km^{-1}, indicating a decrease in hydrometeor size in the ice phase within this TC basin. For these cases, the ATL and NWPAC basins had the highest density of negative slopes of KuPR in both the eyewall and inner core regions of each storm, but also observed instances of positive slopes of KuPR, indicating a mixture of both ice phase growth processes and means that lead to a decrease in frozen hydrometeor size.

The slopes of uncorrected KuPR in the ice phase in the eyewall exhibit negative slopes across the NWPAC, SPAC, ATL, and SIND basins, implying primarily ice crystal growth through processes such as aggregation and riming. One exception is the NIND ocean basin which has a mode of 0.1 dBZ km^{-1}, indicating a decrease

in hydrometeor size. One potential explanation for this difference may be due to shallower convection in this region resulting in a shallower ice-phase layer, or aggregates being advected radially outward from the eyewall (e.g., Houze 2010). In the inner core region, profiles in all ocean basins are skewed towards negative slopes of KuPR within the warm cloud layer, with the mode of approximately -0.35 dBZ km^{-1} which is indicative of hydrometeor growth. The ECPAC basin experienced a larger mode closer to -0.15 dBZ km^{-1}, potentially indicating the increased presence of ice multiplication.

While investigating vertical profiles of KuPR in both the liquid and ice phase as a function of distance from the storm center show primarily bimodal distributions with both positive and negative slopes of KuPR (aside from some subtle differences), using a shear-relative framework provides additional insight into precipitation processes and structure in TCs (e.g., Didlake Jr. and Kumjian 2018; Laurencin et al. 2020a).

4.3.3 Shear-Relative Analysis

In addition to examining vertical profiles of KuPR as a function of distance from the TC center, vertical profiles in each 850-200 hPa shear-relative quadrant were investigated when these data were available from the SHIPS database. Figure 35 illustrates PDFs of vertical slopes of KuPR in the liquid phase in the eyewall within each shear-relative quadrant for all TC basins that had vertical profiles at this distance from the storm center. In both the downshear left (DL) and downshear right (DR)

quadrants, the ECPAC, NWPAC, and SPAC have modes ranging from -0.45 dBZ km^{-1} (SPAC) and -0.35 dBZ km^{-1} (ECPAC and NWPAC). While these values are similar, the SPAC exhibits the greatest variance in all quadrants implying the greatest variability of warm rain processes (i.e., CC, drop breakup, size-sorting, and evaporation) in all portions of all storms. In the DR quadrant, the NWPAC and ECPAC basins have similar modes of -0.1 to -0.25 dBZ km^{-1}, with the SPAC basin having a more uniform distribution with no evident peaks, implying a mixture of CC and non-CC processes.

Figure 36 displays the slopes of KuPR in the liquid phase within each shear-relative quadrant in the inner core region of all TCs examined. In the DL quadrant, each ocean basin has a mode ranging from -0.45 to -0.20 dBZ km^{-1}, with the ATL basin having the highest degree of CC-dominant profiles, which is also true in the other quadrants. Aside from the ATL basin, all other regions have bimodal distributions with the primary mode being negative indicating CC, with a positive, secondary mode, indicating the presence of additional non-CC processes in the inner core region of the storm in all quadrants. One exception is the distribution of slopes in the upshear left quadrant (UL) (Fig. 36c), where the primary mode in the SIND basin is positive. This implies that non-CC processes such as evaporation and/or drop breakup are the most prominent signatures. Further, in the upshear right (UR) quadrant, the ECPAC, NWPAC, SPAC, and SIND regions all have a large variance in slope ranging from -1.0 to 1.0 dBZ km^{-1}, whereas the ATL basin peaks at 0.20

dBZ km^{-1}.

In the ice phase (Fig. 37), the DL, DR, and UL quadrants have modes associated with negative slopes of KuPR and therefore translating to ice crystal growth in the eyewall. The SPAC basin experiences the largest variance in KuPR slope in the DL and UL quadrants, suggesting a greater variability in precipitation microphysics leading to both hydrometeor growth (i.e. via aggregation) and a decrease in ice crystal size such as ice multiplication whereas the NWPAC and ECPAC regions exhibit modes of -0.35 to -0.30 dBZ km^{-1} in the DL, DR, and UL quadrants, implying ice crystal growth. In the UR quadrant, the ECPAC basin has a mode of 0.00 dBZ km^{-1}, which indicates a balance between ice crystal growth and a reduction in ice hydrometeor size. Further, the SPAC region shows a mode of -0.5 dBZ km^{-1}, implying the prominence of hydrometeor growth in the ice phase.

As shown in Figure 37, Figure 38 shows slopes of KuPR in the ice phase across all shear-relative quadrants in the inner core region of all TCs.

When examining ice-phase precipitation processes in the inner core (Fig. 38), all ocean basins have a mode corresponding to negative slopes of KuPR, with the ECPAC and NWPAC basins being the most prominent. There also exists a smaller secondary peak across each ocean basin with a mode of 0.45 dBZ km^{-1}. While the DR, and UL quadrants also have modes ranging from -0.1 to -0.5 dBZ km^{-1}, with the exception of the SIND basin in the UL quadrant, each secondary peak has a greater density in these three quadrants relative to the DL quadrant. This implies a greater diversity

of ice-phase processes (both resulting in growth and ice crystal fragmentation) in the aforementioned quadrants of all TCs in each basins. Surprisingly, the SIND basin experiences ice crystal breakup in the UL quadrant of the inner core region, which is vastly different that the large positive mode of -0.35 dBZ km^{-1} in the ATL basin indicating a high frequency of ice crystal growth. Last, the largest variance of slopes of KuPR in the ice phase in the inner core region occured in the DR quadrant in the NWPAC basin, indicating a large variability of cold cloud processes translating to both ice phase hydrometeor growth and decrease in ice crystal size.

In order to quantify the depth of precipitating clouds in each quadrant, storm region, and TC ocean basin, echo top heights from the GPM DPR algorithm are illustrated in Figure 39 (eyewall region) and Figure 40 (inner core region). In the eyewall, the ATL basin sees the greatest mode of echo top heights across all quadrants relative to each basin, with typical values of 10.0-11.0 km. In the DL quadrant exhibits the largest variance in echo top height compared to the other regions of the TC with storm tops exceeding 15.0 km in various DPR footprints. The highest mean echo top height occurs in the DL quadrant of all TCs, which is different than the results found in Didlake and Kumjian 2017b which determined that most convective precipitation occurred in the DR quadrant in Hurricane Arthur (2014). The greatest variance of echo top heights was in the SPAC basin, particularly in the UL and UR quadrants which experienced values as high as 20.0 km. The NWPAC basin observed the lowest mean echo top heights, with modes below 10.0 km in all shear-relative quadrants.

The largest consistency in the mode of echo top heights across all regions occurred in the DR quadrant, with peaks ranging from 7.5 km to 11.0 km.

Figure 40 displays echo top heights in the inner core across all TC ocean basins and shows considerable variability in values between quadrants and ocean basins, particularly in the UR quadrant. In the DL quadrant, the mode is clustered between 8.5 and 11.0 km, with the ATL basin experiencing the highest mode. The DR quadrant exhibits similar characteristics, with the overall distribution being shifted towards higher echo top height values, with the ATL basin having the largest mode of 11.5 km. The ATL region also has the largest mode in the UL quadrant of approximately 10.5 km, with the SPAC basin having the lowest mode of 8.0 km. This differs from the UR quadrant where the ATL basin has a mode of 2.5 km, whereas the NWPAC has the largest mode of 11.5 km. This suggests that TCs were asymmetric in the ATL cases, with a lack of convection in the UR quadrant resulting in a lower mean echo top height.

4.4 Discussion

It is important to understand precipitation processes in TCs as numerical models struggle to properly capture the underlying bulk microphysics, which can ultimately affect quantitative precipitation forecasts and proper resolution of TC intensity and structure (Hristova-Veleva et al. 2021). Vertical profiles of KuPR in both the liquid and ice phases displayed large variations in slopes in each shear-relative quadrant

and TC basin, suggesting a mixture of processes leading to both hydrometeor growth and a decrease in hydrometeor size. This is consistent with other TCs that exhibited variability in precipitation processes which were a result of large-scale environmental variables such as 850-200 hPa vertical wind shear, storm motion, and tropospheric moisture (e.g., Didlake and Kumjian 2017b; Didlake Jr. and Kumjian 2018; Laurencin et al. 2020a).

Investigation of vertical slopes of KuPR in the liquid phase by distance from the TC center (Fig 33. and Fig 34.) show bimodal distributions with negative slopes indicative of hydrometeor growth (i.e. collision-coalescence, riming, or aggregation depending on the precipitation phase) or a decrease in hydrometeor size (i.e. evaporation, size-sorting, breakup, and ice multiplication). This implies that a combination of microphysical processes are occurring in different portions of TCs, which has also been noted in prior work from Brauer et al. (2020), Laurencin et al. (2020a), and Homeyer et al. (2021b). When partitioning each annulus of TCs into 850-200 hPa shear-relative quadrants, more information and signatures relating to precipitation microphysics are revealed in both the liquid phase and ice phase, which can then be related to the large-scale environmental variables such as vertical wind shear and tropospheric moisture.

In the liquid phase, the SPAC and ECPAC exhibited negative modes of KuPR slopes in the eyewall, whereas the NWPAC basin observed slopes with a mode closer to 0.0 dBZ km^{-1}, particularly in the DL and DR quadrants (Fig. 35). One potential

explanation for these differences across each TC ocean basin is the larger values of 850-200 hPa wind shear during the JJA months over the NWPAC basin, particularly north of 20°N where shear values exceed 20 knots. The higher values of shear in this region are known to result in TC asymmetries which can result in an increase in evaporation and size-sorting processes (e.g., DeHart and Bell 2020; Laurencin et al. 2020a). The UR quadrant in the eyewall region had negative modes of KuPR slope in the liquid phase corresponding to CC-dominant precipitation across all basins. However some slopes of KuPR were positive, indicating the presence of drop breakup. This is consistent with other observations in TCs which showed a balance between CC and drop breakup in the eyewall region (McFarquhar and Black 2004).

The inner core region of TCs shows a bimodal distribution of slopes in the liquid phase (Fig. 36), indicative of a mixture of CC and non-CC processes, which is likely a reflection of this region containing both convective and stratiform precipitation. The ATL region has negative modes in all quadrants indicating CC-dominant precipitation, whereas the SIND basin has a positive mode in the UL quadrant, with an additional secondary positive mode in the DL and DR quadrants. A potential reason for these differences is a higher magnitude of vertical wind shear in the SIND basin during the DJF months, with values exceeding 25 knots south of 20°, whereas the ATL basin typically observes lower shear values of 10-20 knots during the JJA months. The ATL region also typically sees greater values of tropospheric moisture compared to the SIND region (Fig. 31) especially in the Gulf of Mexico where values

exceed 40 kg m^{-2}. The higher values of tropospheric moisture in this region act to minimize dry air entrainment and evaporation in TCs, resulting in a higher frequency of negative slopes of KuPR in the liquid phase.

When examining slopes of KuPR in the ice phase, the DL, DR, and UL quadrants show negative modes implying hydrometeor growth in the ice phase (Fig. 37). One exception is the ECPAC basin showing a positive mode in the UR quadrant which is indicative of ice multiplication and an overall decrease in ice crystal size. While the majority of the profiles are reflective of ice crystal growth, TCs such as Hurricane Laura (2020) have exhibited positive slopes of KuPR in the ice phase in certain regions of the storm, translating to a decrease in hydrometeor size (Brauer et al. 2022). In the inner core, modes are similar across all basins in the DL quadrant, with a bimodal distribution in both the DR and UL quadrants. This implies that regardless of vertical wind shear and tropospheric moisture, hydrometeor growth in the ice phase occurs across all basins in the DL quadrant, which is consistent with the radar observations discussed in Black and Hallett (1986). Further, the additional growth of precipitation in the ice phase is also known to result in possible further TC intensification through latent heat release (Black and Hallett 1986).

Figure 41 illustrates the spatial distribution of near-surface KuPR (Fig. 41a), echo top height (Fig. 41b), vertical slope of KuPR in the liquid phase (Fig. 41c), and vertical slope of KuPR in the ice phase (Fig. 41d) in a particular case in the ATL basin. The maximum values of KuPR in the eyewall region (55-60 dBZ) were confined

to the eastern half of the TC, and were located upwind from the maximum in echo top height (14 km) in the northeastern eyewall. Assuming a direct relationship between KuPR and rainfall rate at the surface, this is consistent with Hamada et al. (2015) that found a weak correlation between the deepest convection and highest rainfall rate at the surface in the tropics and subtropics. Figure 41c shows a bimodal spatial distribution of both positive and negative slopes of KuPR in the warm cloud layer, with a region of negative slopes encompassing the eastern half of the eyewall which is indicative of CC or a balance between CC and drop breakup, and has been observed in other TCs (e.g., Feng and Bell 2019). Feng and Bell (2019) also determined that the largest median drop size was found in the region of the strongest updrafts. This is consistent with a region of negative slopes of KuPR (-0.5 dBZ km^{-1}), which is collocated with the highest echo tops of 14 km in the northern eyewall. Further, KuPR is lower in the western portion of the storm with values of 30-50 dBZ and are collocated with a region of positive slope of KuPR, implying the prescence of evaporation, size-sorting, or drop breakup. While vertical profiles of KuPR in the ice phase only existed primarily in the eyewall and principal rainband (Fig. 41b), the distribution of slopes were almost entirely negative, indicating ice crystal growth.

An additional analysis of echo top heights can be directly related to precipitation type in TCs (i.e. convective or stratiform) (Homeyer et al. 2021b), and can provide insight into storm asymmetries and precipitation structure. In the eyewall, the highest mean echo top heights in the SIND, ATL, and ECPAC basins occurred in the DL

quadrant, whereas the NWPAC region has a mode of 2.5-3.0 km in this region, and has a highest mean echo top height of approximately 9.0 km in the DR quadrant (Fig. 39). This suggests that larger asymmetries existed in the NWPAC region compared to the SIND, ATL, and ECPAC basins. One explanation for this difference is that the NWPAC region experiences a greater magnitude of vertical wind shear of 25-30 knots north of 30°N, whereas the ECPAC, SIND, and ATL regions typically experience lower values of shear ranging from 15-20 knots. The greater average 850-200 hPa shear values in the NWPAC basin are known to contribute to asymmetries in TC structure (e.g., DeMaria 1996; Black et al. 2002). Further, this suggests that weaker convection and stratiform precipitation were more prominent in the NWPAC basin whereas TCs in other regions contained deep convection in various parts of TCs. Across all quadrants, the SPAC basin experienced the greatest variance in echo top height, with tops as high as 20.0 km observed by the DPR in the DL, UL, and UR quadrants indicating that this ocean basin had the deepest convection for all the cases examined.

4.4.1 Limitations and Future Work

While this work provides a robust and objective method to utilize the GPM DPR to investigate vertical profiles of KuPR to better understand precipitation processes in TCs, there are some limitations of this work to be discussed. Figure 42 shows two TCs in the ECPAC ocean basin that exhibit entirely different structure and corresponding

intensity. Figure 42a has a rather compact eyewall and inner core region, whereas Figure 42b has a broader inner core and an asymmetric structure where most of the precipitation is confined to the eastern half of the storm. The IBTrACS storm center is therefore much further away from most of the precipitation in Figure 42b, resulting in most of the vertical profiles of KuPR to fall in the inner core region rather than the eyewall region due to the aforementioned objective method to partition each storm into various annuli relative to the storm center. Further, there are evident differences in TC intensity between the two cases, which is another factor known to influence TC precipitation structure (Lonfat et al. 2004). There are also obvious differences between the attenuation-corrected KuPR distributions compared to the uncorrected KuPR distributions between the eyewall and inner core regions. The reason for these differences should be investigated in future work in order to improve the DPR attenuation-correction algorithm in TCs.

4.5 Conclusions

The GPM DPR provides a unique opportunity to examine precipitation structure in TCs on a global scale, particularly over the open ocean and other areas where ground radar networks are non-existent. This study matched IBTrACS TC storm centers with corresponding DPR overpasses and vertical slopes of attenuation-corrected KuPR and uncorrected KuPR were examined in both the liquid phase and ice phase in different annuli and shear-relative quadrants of TCs in 6 ocean basins. Vertical slopes of

KuPR in the liquid phase were characterized as CC-dominant (negative slopes) and non-CC dominant precipitation (positive slopes), with a similar framework in the ice phase with negative slopes translating to ice crystal growth and positive slopes corresponding to ice multiplication and a net decrease in hydrometeor size (Porcacchia et al. 2019; Brauer et al. 2021). As hypothesized, precipitation processes varied by TC ocean basin, distance from the storm center, and by shear-relative quadrant, with the DL quadrant exhibiting the greatest frequency of negative slopes of KuPR, indicating CC-dominant precipitation. Further, the ATL basin contained the highest mean echo top height, with modes exceeding 10.0 km in the DL, DR, and Ul quadrants indicating deep convection in these portions of the TCs examined. Differences in the sign of slopes of KuPR by TC ocean basin were attributed to large-scale environmental variables such as climatological 850-200 hPa vertical wind shear and total integrated water vapor, which are known to influence TC structure and precipitation processes (Gray 1968; DeMaria et al. 2001). Specifically, the SIND basin showed positive modes of KuPR slope in the liquid phase, specifically in the UL quadrant which can be translated to the presence of non-CC dominant precipitation such as drop breakup, evaporation, and size-sorting. This is likely due to the presence of mean 850-200 hPa vertical wind shear exceeding 25-30 knots poleward of 20°S, which is known to result in TC asymmetries.

Future work should investigate how vertical slopes of KuPR vary with TC intensity to determine the extent of CC versus non-CC processes in storms of different mag-

nitude. Further, additional work should determine how precipitation processes vary with storm motion and 850-200 hPa shear magnitude, as these variables are known to influence TC structure and eyewall asymmetries (e.g., DeMaria et al. 2001). One additional factor that should be investigated is the seasonal influence on TC structure. This is because large-scale environmental factors such as 850-200 hPa wind shear and tropospheric moisture are known to vary interseasonally (e.g., Gray 1968; DeMaria et al. 2001) as the jet stream and associated vertical wind shear translates poleward during the onset of the TC season, and equatorward towards the end of the period favorable for tropical cyclogenesis.

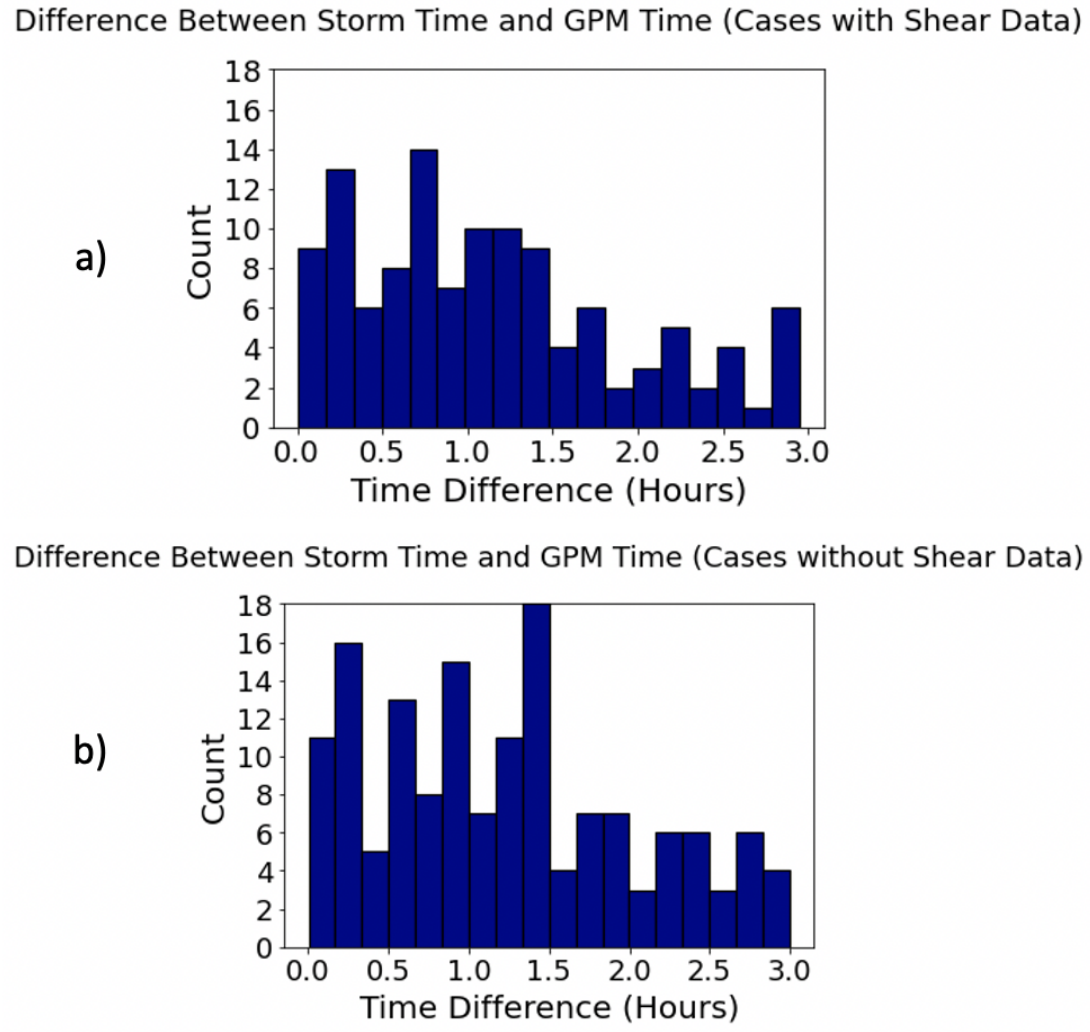

Figure 29: Histograms of time differences between each GPM DPR overpass and the IBTrACS storm center point for cases with wind shear data available (Fig. 29a) and without wind shear data available (Fig. 29b). Only cases where the difference was < 0.5 hours were retained in this analysis.

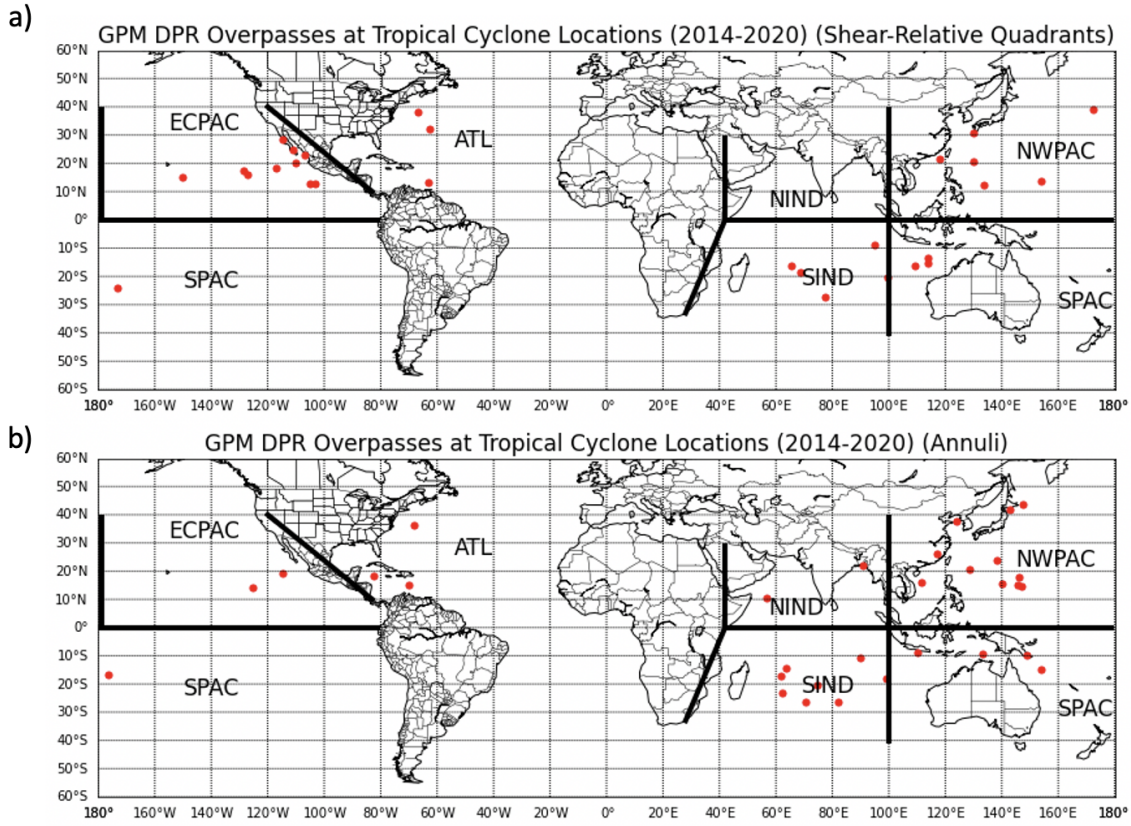

Figure 30: Tropical cyclone locations corresponding to each GPM DPR overpass from 2014-2020. Only overpass match ups between 45^oS and 45^oN were obtained. Points over land were also omitted.

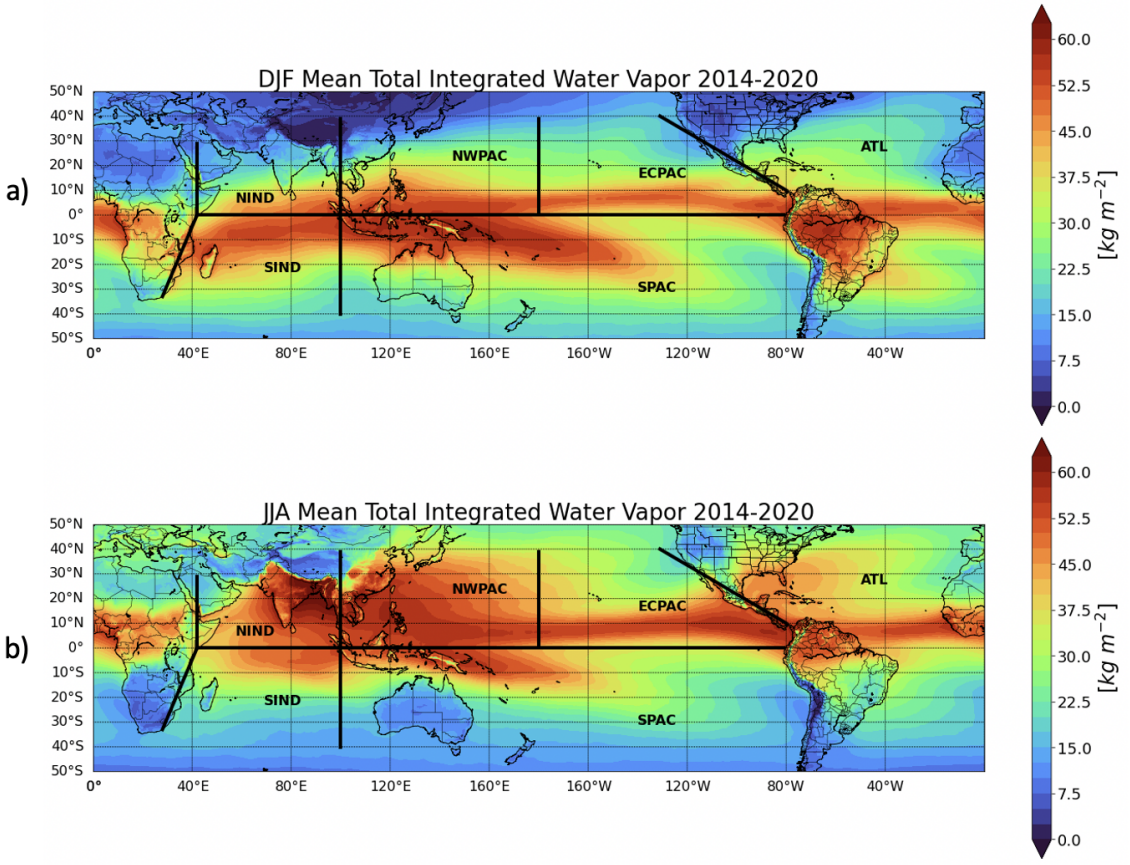

Figure 31: Seasonal composites of mean boreal winter (DJF) total integrated water vapor from 2014-2020 (a), and mean boreal summer (JJA) total integrated water vapor from 2014-2020 (b).

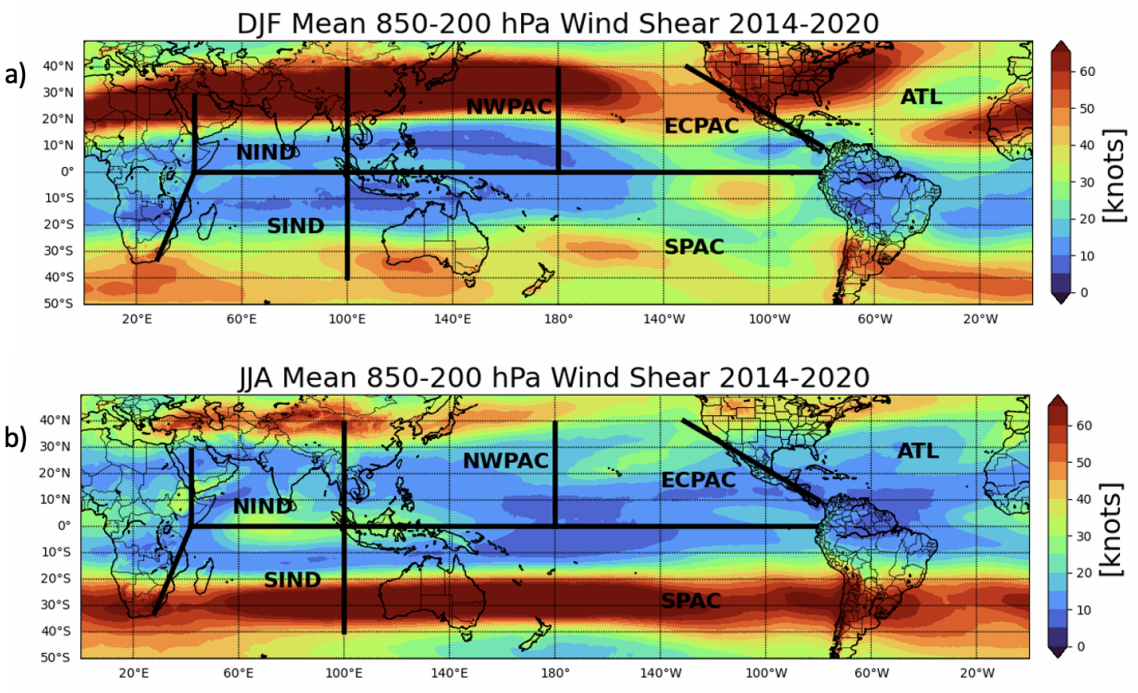

Figure 32: Seasonal composites of mean boreal winter (DJF) 850-200 mb vertical wind shear from 2014-2020 (a), and mean boreal summer (JJA) 850-200 mb vertical wind shear from 2014-2020 (b).

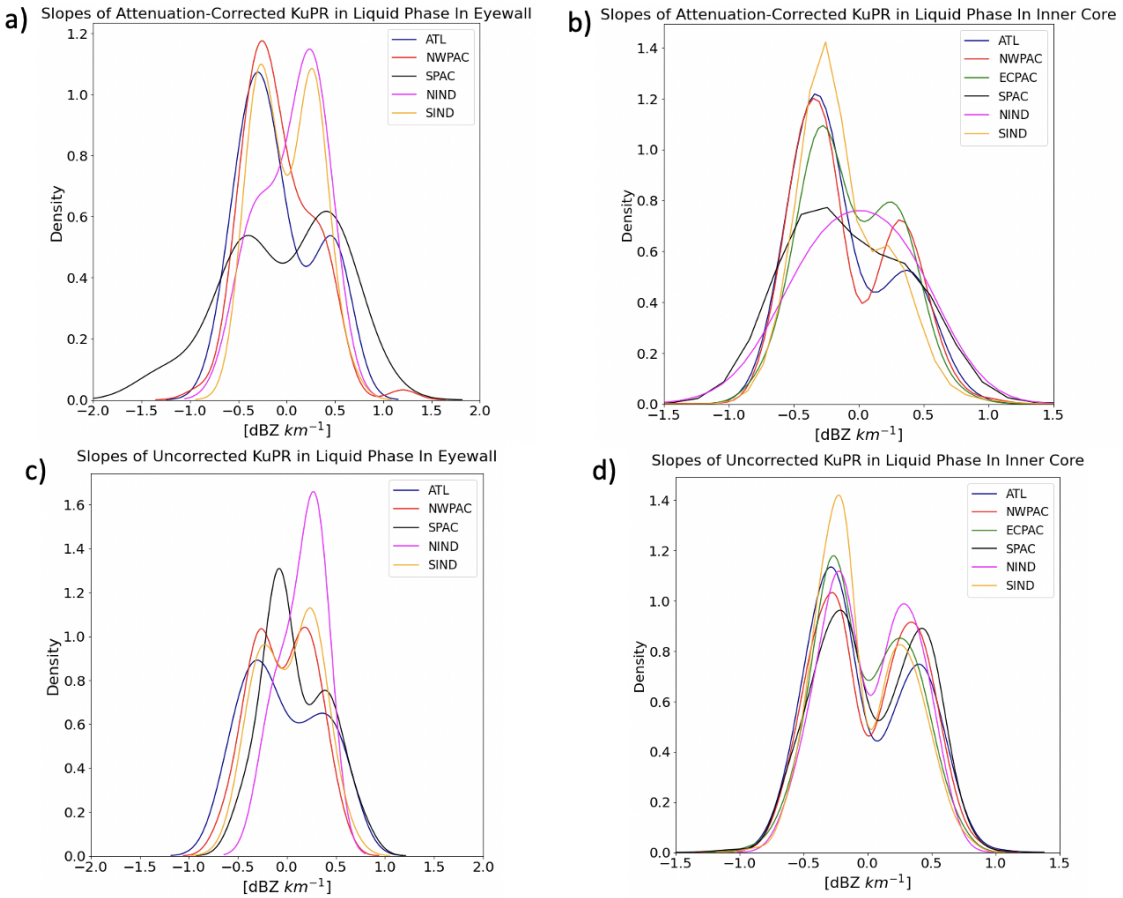

Figure 33: Probability density functions (PDFs) of vertical slopes of attenuation-corrected KuPR in the liquid phase in the eyewall (Fig. 33a) and in the inner core (Fig. 33b), PDFs of vertical slopes of uncorrected KuPR in the liquid phase in the eyewall (Fig. 33c) and in the inner core (Fig. 33d) across all 6 TC ocean basins.

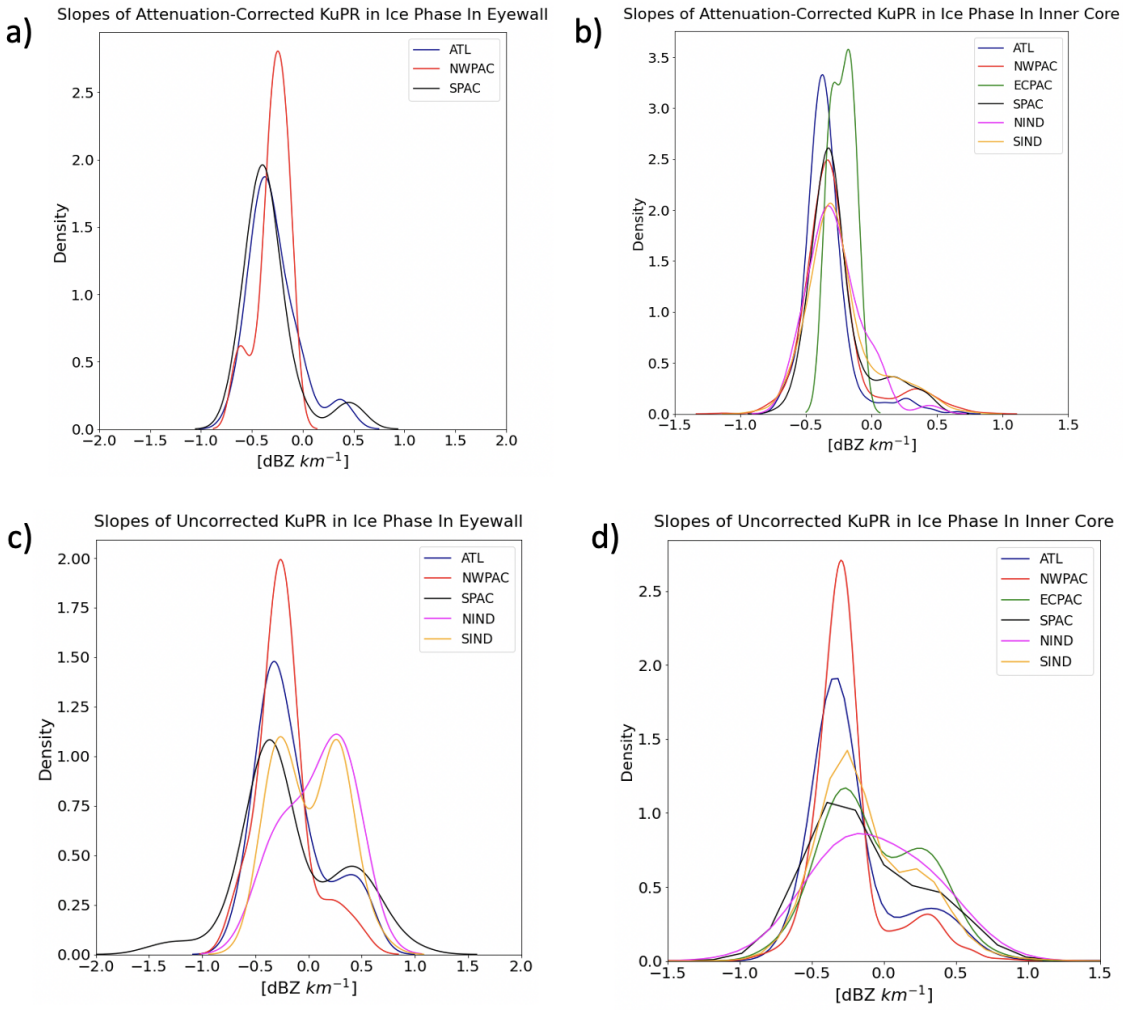

Figure 34: Probability density functions (PDFs) of vertical slopes of attenuation-corrected KuPR in the ice phase in the eyewall (Fig. 34a) and in the inner core (Fig. 34b), PDFs of vertical slopes of uncorrected KuPR in the ice phase in the eyewall (Fig. 34c) and in the inner core (Fig. 34d) across all 6 TC ocean basins.

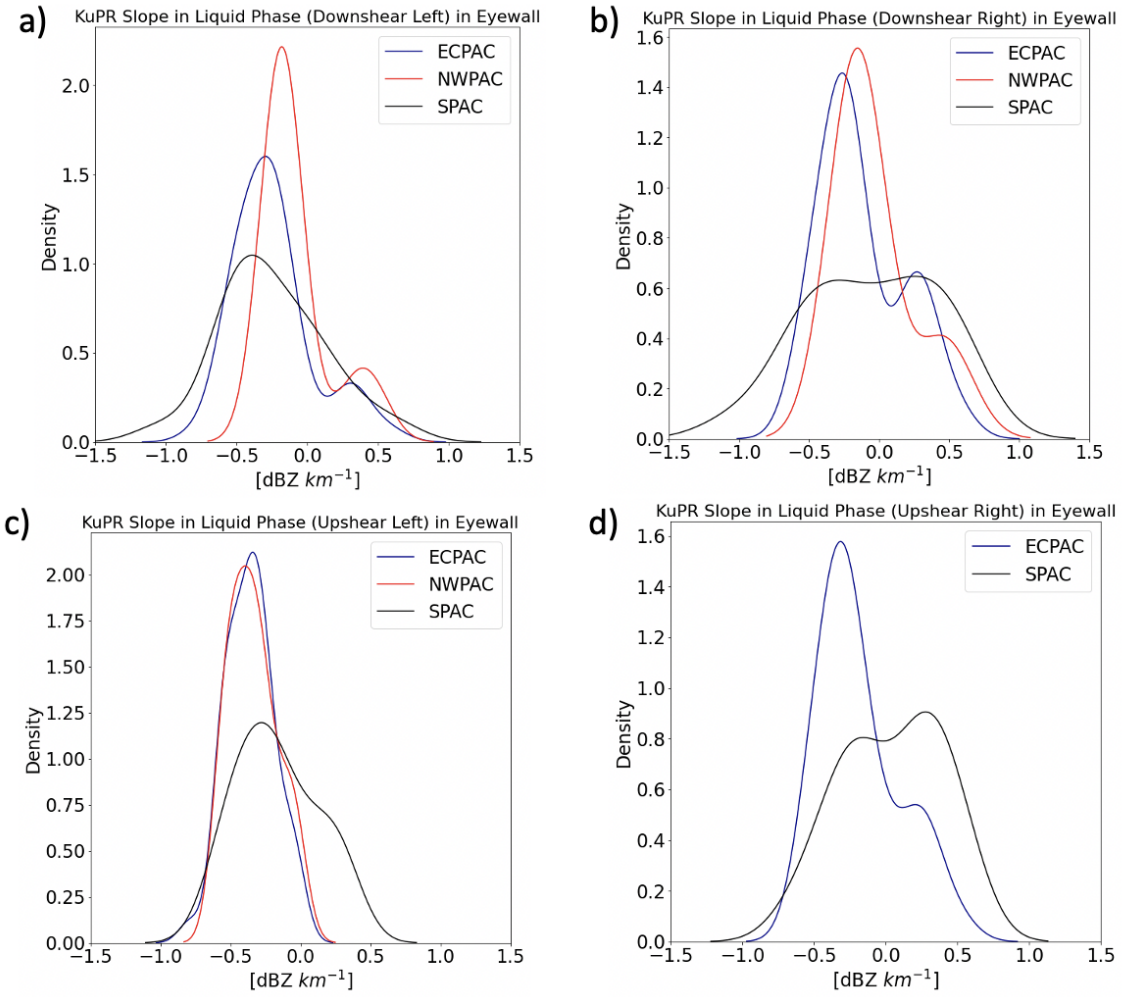

Figure 35: Probability density functions (PDFs) of vertical slopes of attenuation-corrected KuPR in the liquid phase for each shear-relative quadrant across each TC basin that the DPR sampled the eyewall region.

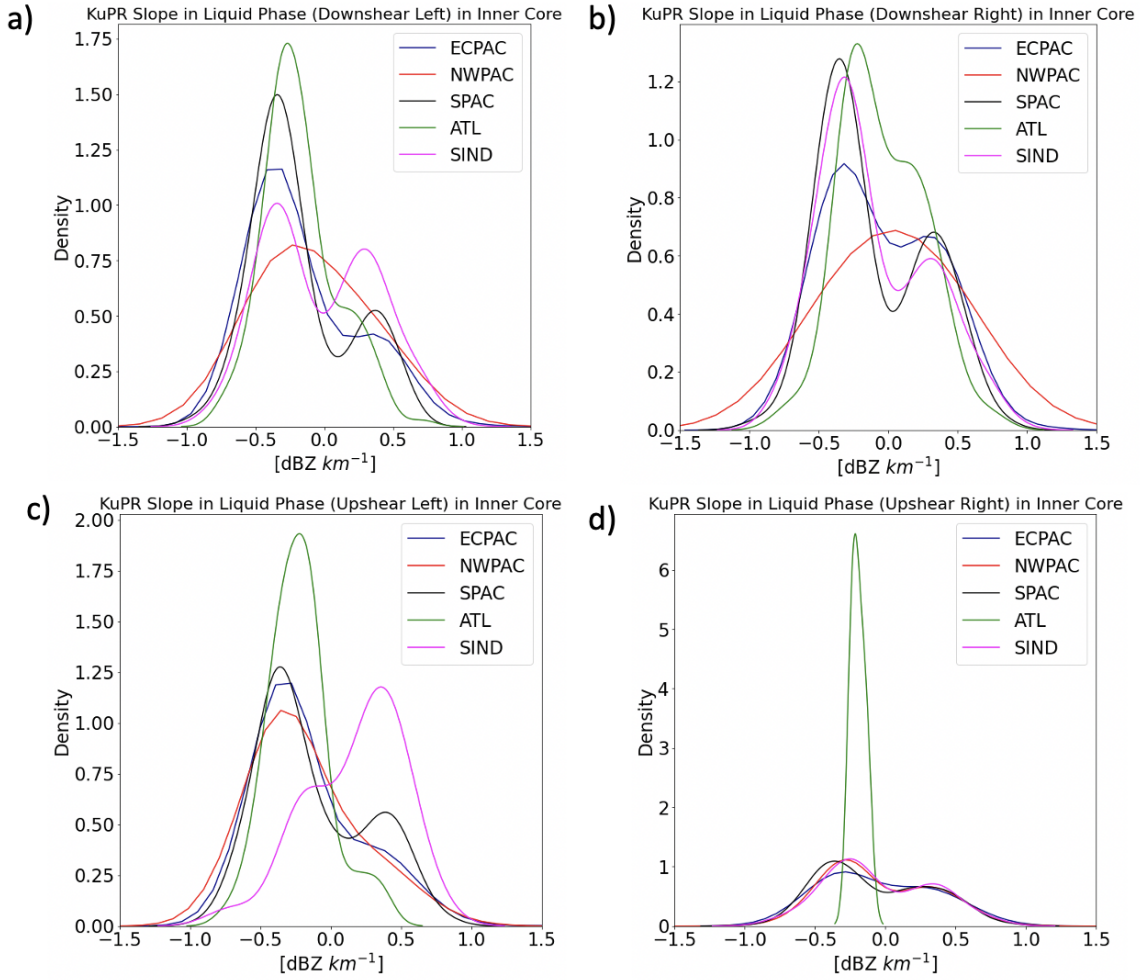

Figure 36: Probability density functions (PDFs) of vertical slopes of attenuation-corrected KuPR in the liquid phase for each shear-relative quadrant across each TC basin that the DPR sampled the inner core region.

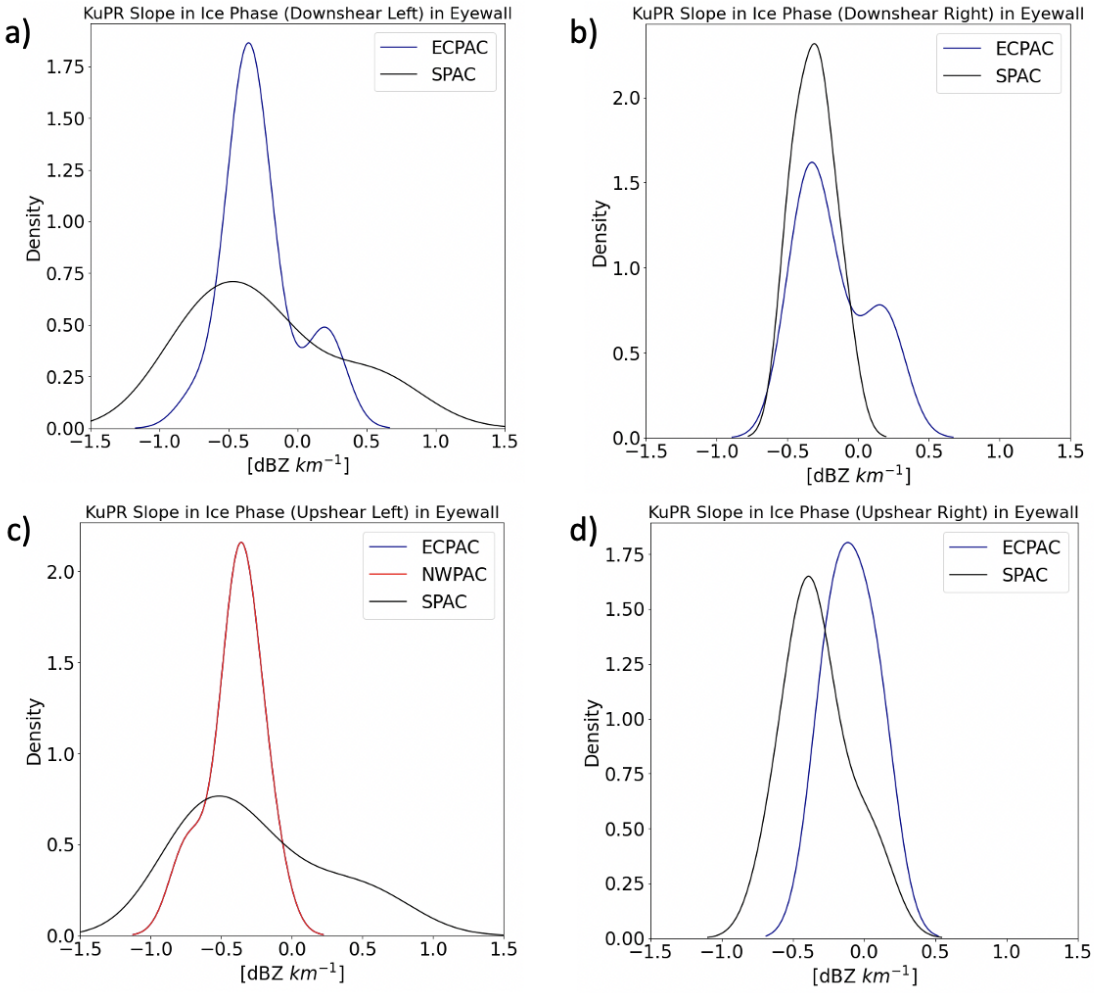

Figure 37: Probability density functions (PDFs) of vertical slopes of attenuation-corrected KuPR in the ice phase for each shear-relative quadrant across each TC basin that the DPR sampled the eyewall region.

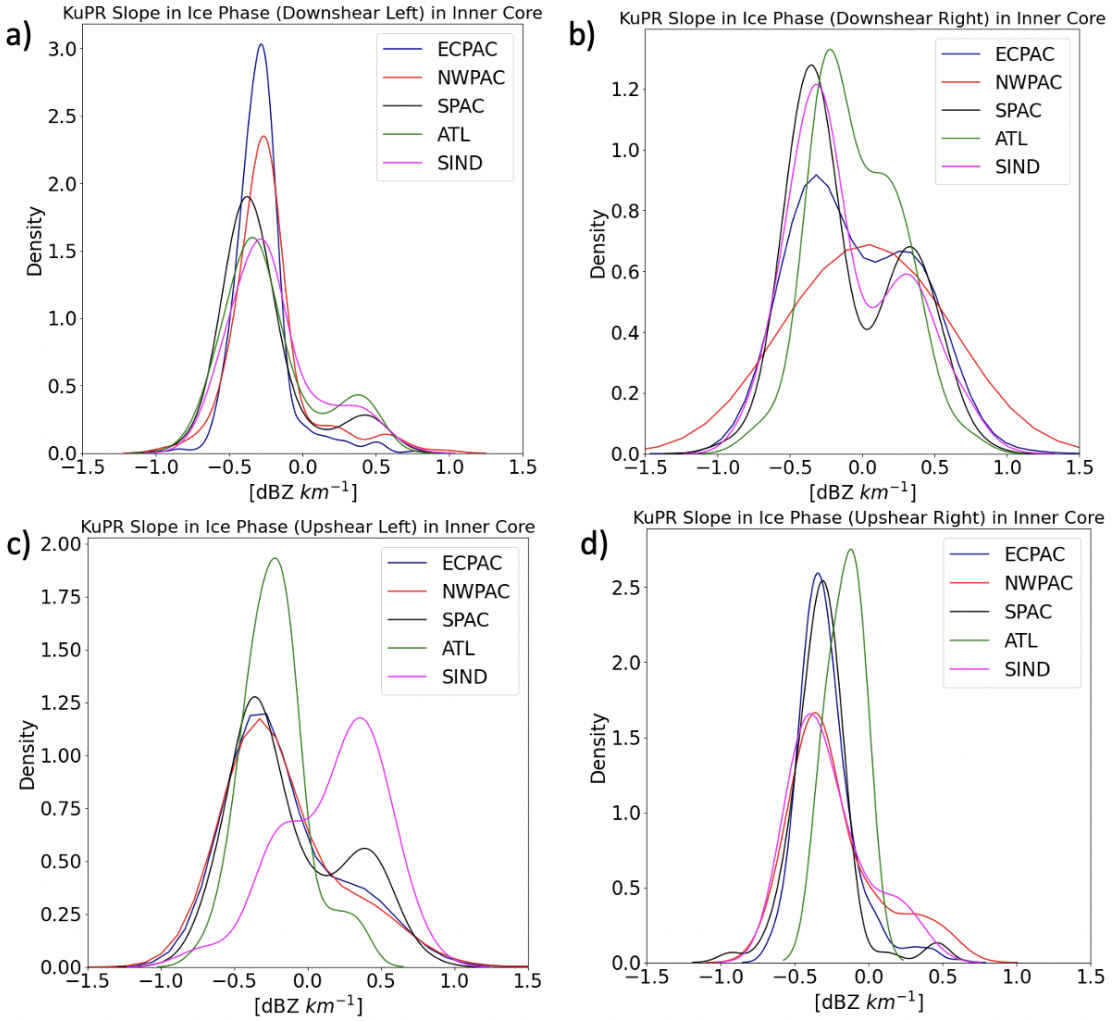

Figure 38: Probability density functions (PDFs) of vertical slopes of attenuation-corrected KuPR in the ice phase for each shear-relative quadrant across each TC basin that the DPR sampled the inner core region.

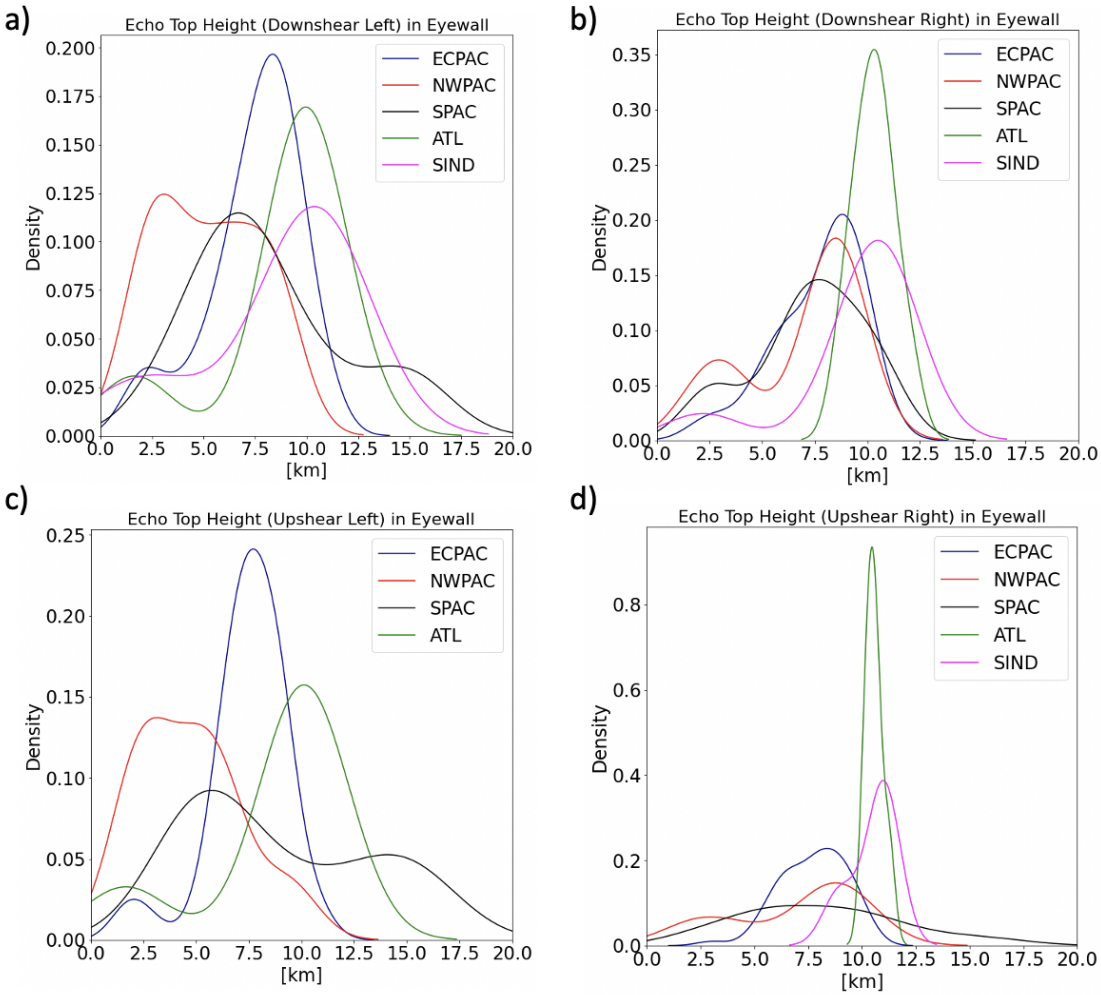

Figure 39: Probability density functions (PDFs) of echo top heights for each shear-relative quadrant across each TC basin that the DPR sampled the inner core region.

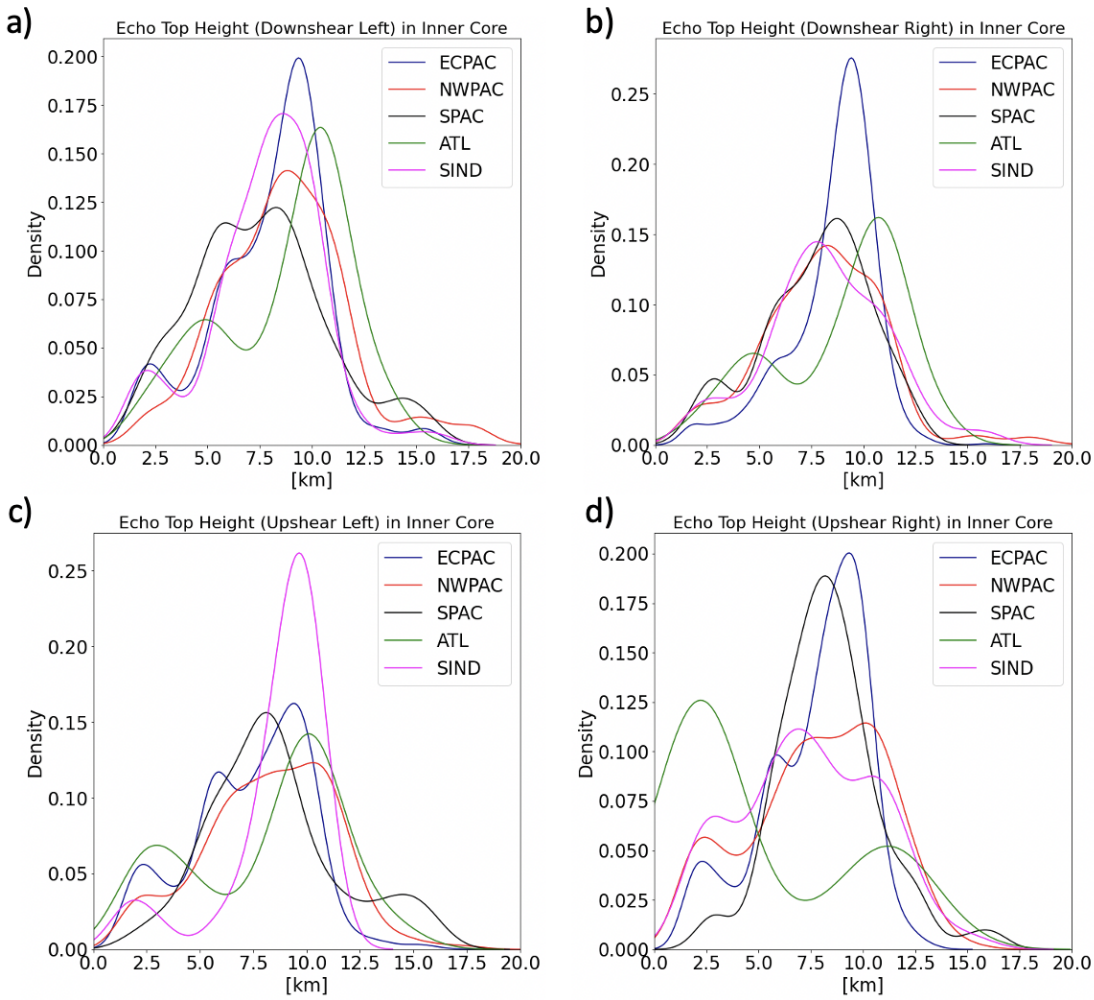

Figure 40: Probability density functions (PDFs) of echo top heights for each shear-relative quadrant across each TC basin that the DPR sampled the eyewall region.

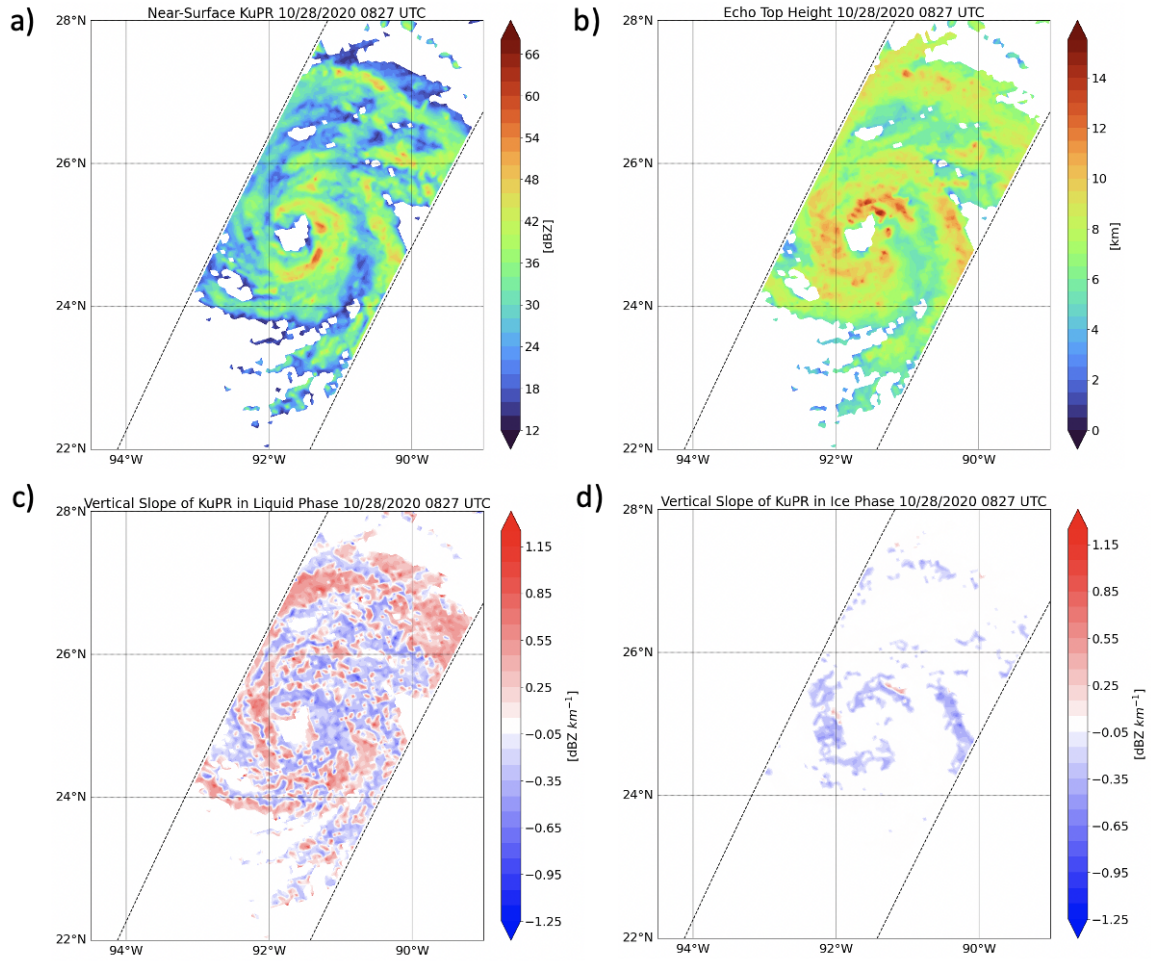

Figure 41: Near-surface attenuation corrected KuPR (Fig. 41a), echo top heights (km) (Fig. 41b), vertical slope of KuPR in the liquid phase (Fig. 41c), and vertical slope of KuPR in the ice phase (Fig. 41d).

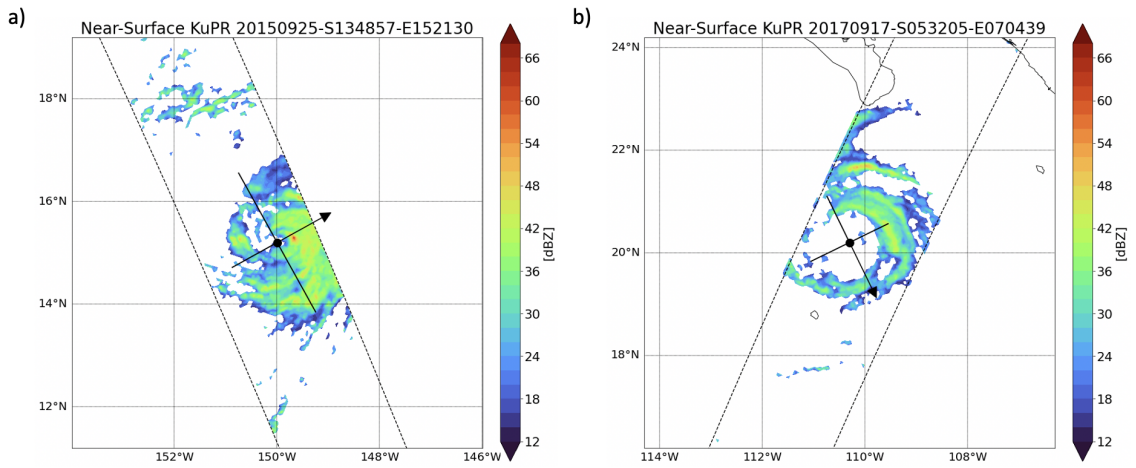

Figure 42: Near-surface attenuation corrected KuPR for a TC with a compact eyewall and inner core region (Fig. 42a) and a TC with a broad eyewall and inner core region (Fig. 42b). The SHIPS 850-200 hPa shear vector is denoted by the arrow whereas the IBTrACS storm center is illustrated by the black dot.

Table 2: Cases for each type of analysis in each TC ocean basin

Region	ATL	ECPAC	SPAC	NWPAC	NIND	SIND	Total
Shear Cases	3	11	4	6	0	4	28
Annulus Cases	3	2	5	11	2	8	31

5 Conclusions

5.1 Summary

This dissertation has investigated precipitation microphysics in TCs using polarimetric ground radar observations, space-borne radar retrievals from the NASA GPM DPR, and disdrometer data. Specifically, vertical slopes of KuPR from the GPM DPR, Z_H, and Z_{DR} to quantify CC and non-CC processes (i.e. drop breakup, size-sorting, and evaporation) in the liquid phase and processes leading to ice crystal growth (i.e. riming and aggregation) in the solid phase. 4 hypotheses served as the basis for Chapters 2-4 and are summarized as follows.

Chapter 2 hypothesized that TC precipitation characteristics (i.e. CC and/or a balance between CC and drop breakup) would be maintained as Tropical Storm Bill (2015) tracked inland over anomalously moist soils, which served to increase latent heat fluxes and contribute to an increasingly moist boundary layer, resulting in a deeper warm cloud depth and more opportunity for warm rain processes to be maintained inland from the landfall point. As Bill progressed north and east over Oklahoma, Missouri and Kentucky, there were two instances of tropical cyclone maintenance and re-intensification (TCMI) that exhibited radar signatures associated with CC or a balance between CC and drop breakup. Further, an analysis of potential vorticity, potential temperature, and vertical velocity demonstrated that Bill maintained warm core signatures during both TCMI events.

Chapter 3 compared ground radar observations from the OU SR1-P, the GPM DPR, and disdrometer retrievals in Hurricane Laura (2020) to quantify and compare PSD moments and associated precipitation processes across all observational platforms. The primary hypothesis surrounding this study is that precipitation processes would vary from pre-landfall to post-landfall, and that differences in PSD values and inferred precipitation processes would exist between each retrieval method. Retrievals of cloud properties from the DPR showed a decrease in the frequency of CC processes from pre-landfall to post-landfall and an increase in stratiform precipitation as Laura progressed inland with an overall weakening in convection and lower mean echo top heights. There were also differences between the disdrometer retrievals and PSD moments extracted by the GPM DPR, allowing for a potential opportunity to apply a correction to the DPR algorithm in TCs.

To broaden the scope of our knowledge of precipitation microphysics in TCs, Chapter 4 analyzed vertical profiles of KuPR and echo top heights from the GPM DPR in TCs on a global scale. It was hypothesized that vertical slopes of KuPR and inferred precipitation processes would vary by TC ocean basin, 850-200 hPa shear-relative quadrant, and distance from the storm center due to global variability in average vertical wind shear and tropospheric moisture. The key findings from this study showed that a bimodal distribution of both negative and positive slopes of KuPR exists across both the eyewall and inner core regions of TCs in all ocean basins when shear-relative quadrants are not considered. This implies a mixture of

processes in different regions of the storm leading to CC, drop breakup, evaporation, and size-sorting. A similar analysis in the ice phase showed a similar bimodal trend, with the distributions being skewed towards negative values indicating ice crystal growth. In the shear-relative framework, the differences in modes between TC ocean basins became more apparent with the left-of-shear portion of TCs exhibiting the greatest frequency of negative modes implying CC or a balance between CC and drop breakup. In the ice phase, the NWPAC and SIND basins showed the greatest variance in slope, suggesting a mixture of processes leading to both ice crystal growth and shrinkage in the inner core region of TCs. In the eyewall region, the SPAC basin had the highest variance, particularly in the left-of-shear quadrants. A brief analysis of echo top heights suggests that precipitating cloud tops can be as high as 20.0 km, with the SPAC basin seeing the greatest heights in the DL, UL, and UR quadrants in the eyewall.

5.2 Final Remarks and Future Work

As numerous landfalling TCs have resulted in catastrophic freshwater flooding leading to loss of life and property, it is important to keep improving our knowledge of precipitation processes in these storms. This should be done in order to improve the representation of microphysics in numerical simulations of TCs. By retrieving cloud properties in which microphysics can be inferred, the results of this dissertation can be used as a benchmark for validation and evaluation of PSD moments and precip-

itation processes in TCs. A more accurate depiction of precipitation structure and microphysics in TCs will allow for more accurate quantitative precipitation forecasts which can be translated to warning operations and water resource management.

Future work can use a similar technique of using vertical slopes of radar variables for quantifying precipitation processes in other impactful weather phenomena such as winter storms and mid-latitude convection to improve representation of microphysics in these events. Further, additional radar platforms such as CloudSat (W-band) can be incorporated into these analyses to provide a more robust quantification of precipitation structure in different cloud systems.

References

Aberson, S., M. Black, R. Black, R. Burpee, J. Cione, C. Landsea, and F. Marks, 2006: Thirty Years of Tropical Cyclone Research with the NOAA P-3 Aircraft. *Bulletin of The American Meteorological Society - BULL AMER METEOROL SOC*, **87**, doi:10.1175/BAMS-87-8-1039.

Andersen, T. K., and J. M. Shepherd, 2014a: A global spatiotemporal analysis of inland tropical cyclone maintenance or intensification. *International Journal of Climatology*, **34 (2)**, 391–402, doi:10.1002/joc.3693.

Andersen, T. K., and J. M. Shepherd, 2014b: A global spatiotemporal analysis of

inland tropical cyclone maintenance or intensification. *International Journal of Climatology*, **34 (2)**, 391–402, doi:10.1002/joc.3693.

Arndt, D. S., J. B. Basara, R. A. McPherson, B. G. Illston, G. D. McManus, and D. B. Demko, 2009: Observations of the overland reintensification of tropical storm erin (2007). *Bulletin of the American Meteorological Society*, **90 (8)**, 1079–1094, doi:10.1175/2009BAMS2644.1.

Atlas, D., R. C. Srivastava, and R. S. Sekhon, 1973: Doppler radar characteristics of precipitation at vertical incidence. *Reviews of Geophysics*, **11 (1)**, 1–35, doi: https://doi.org/10.1029/RG011i001p00001.

Atlas, D., and C. W. Ulbrich, 2000: An observationally based conceptual model of warm oceanic convective rain in the tropics. *Journal of Applied Meteorology*, **39 (12)**, 2165 – 2181, doi:10.1175/1520-0450(2001)040⟨2165:AOBCMO⟩2.0.CO;2.

Austin, P. M., 1987: Relation between measured radar reflectivity and surface rainfall. *Monthly Weather Review*, **115 (5)**, 1053–1070, doi:10.1175/1520-0493(1987)115⟨1053:RBMRRA⟩2.0.CO;2.

Bechini, R., L. Baldini, R. Cremonini, and E. Gorgucci, 2008: Differential reflectivity calibration for operational radars. *Journal of Atmospheric and Oceanic Technology*, **25 (9)**, 1542–1555, doi:10.1175/2008JTECHA1037.1.

Biggerstaff, M. I., A. A. Alford, G. D. Carrie, and J. A. Stevenson, 2021: Hurricane florence (2018): Long duration single- and dual-doppler observations and wind

retrievals during landfall. *Geoscience Data Journal*, **n/a (n/a)**, doi:https://doi.org/10.1002/gdj3.137.

Biggerstaff, M. I., and Coauthors, 2005: The Shared Mobile Atmospheric Research and Teaching Radar: A Collaboration to Enhance Research and Teaching. *Bulletin of the American Meteorological Society*, **86 (9)**, 1263–1274, doi:10.1175/BAMS-86-9-1263.

Black, M. L., J. F. Gamache, F. D. Marks, C. E. Samsury, and H. E. Willoughby, 2002: Eastern Pacific Hurricanes Jimena of 1991 and Olivia of 1994: The Effect of Vertical Shear on Structure and Intensity. *Monthly Weather Review*, **130 (9)**, 2291–2312, doi:10.1175/1520-0493(2002)130⟨2291:EPHJOA⟩2.0.CO;2.

Black, R., and J. Hallett, 1986: Observations of the Distribution of Ice in Hurricanes. *Journal of Atmospheric Sciences*, **43**, 802–822, doi:10.1175/1520-0469(1986)043⟨0802:OOTDOI⟩2.0.CO;2.

Blanchard, D. O., 1998: Assessing the vertical distribution of convective available potential energy. *Weather and Forecasting*, **13 (3)**, 870–877, doi:10.1175/1520-0434(1998)013⟨0870:ATVDOC⟩2.0.CO;2.

Bowman, K. P., and C. R. Homeyer, 2017: GridRad - Three-Dimensional Gridded NEXRAD WSR-88D Radar Data. Research Data Archive at the National Center for Atmospheric Research, Computational and Information Systems Laboratory, Boulder CO.

Brauer, N. S., J. B. Basara, C. R. Homeyer, G. M. McFarquhar, and P. E. Kirstetter, 2020: Quantifying Precipitation Efficiency and Drivers of Excessive Precipitation in Post-Landfall Hurricane Harvey. *Journal of Hydrometeorology*, **21 (3)**, 433–452, doi:10.1175/JHM-D-19-0192.1.

Brauer, N. S., J. B. Basara, P. E. Kirstetter, R. A. Wakefield, C. R. Homeyer, J. Yoo, M. Shepherd, and J. A. Santanello, 2021: The Inland Maintenance and Reintensification of Tropical Storm Bill (2015). Part II: Precipitation Microphysics. *Journal of Hydrometeorology*, **22 (10)**, doi:10.1175/JHM-D-20-0151.1.

Brauer, N. S., and Coauthors, 2022: Hurricane Laura (2020): A Comparison of Drop Size Distribution Moments Using Ground and Radar Remote Sensing Retrieval Methods. *Journal of Geophysical Research: Atmospheres*, Conditionally accepted.

Bringi, V. N., V. Chandrasekar, N. Balakrishnan, and D. S. Zrnić, 1990: An examination of propagation effects in rainfall on radar measurements at microwave frequencies. *Journal of Atmospheric and Oceanic Technology*, **7 (6)**, 829–840, doi:10.1175/1520-0426(1990)007⟨0829:AEOPEI⟩2.0.CO;2.

Brock, F. V., K. C. Crawford, R. L. Elliott, G. W. Cuperus, S. J. Stadler, H. L. Johnson, and M. D. Eilts, 1995: The Oklahoma Mesonet: A Technical Overview. *Journal of Atmospheric and Oceanic Technology*, **12 (1)**, 5–19, doi:10.1175/1520-0426(1995)012⟨0005:TOMATO⟩2.0.CO;2.

Brown, B. R., M. M. Bell, and A. J. Frambach, 2016: Validation of simulated hurri-

cane drop size distributions using polarimetric radar. *Geophysical Research Letters*, **43 (2)**, 910–917, doi:10.1002/2015GL067278.

Cannon, F., F. M. Ralph, A. M. Wilson, and D. P. Lettenmaier, 2017: GPM Satellite Radar Measurements of Precipitation and Freezing Level in Atmospheric Rivers: Comparison With Ground-Based Radars and Reanalyses. *Journal of Geophysical Research: Atmospheres*, **122 (23)**, 12,712–747,764, doi:https://doi.org/10.1002/2017JD027355, URL https://agupubs.onlinelibrary.wiley.com/doi/abs/10.1002/2017JD027355.

Cao, Q., G. Zhang, E. Brandes, T. Schuur, A. Ryzhkov, and K. Ikeda, 2008: Analysis of video disdrometer and polarimetric radar data to characterize rain microphysics in oklahoma. *Journal of Applied Meteorology and Climatology*, **47 (8)**, 2238–2255, doi:10.1175/2008JAMC1732.1.

Carr, N., P. E. Kirstetter, J. J. Gourley, and Y. Hong, 2017: Polarimetric Signatures of Midlatitude Warm-Rain Precipitation Events. *Journal of Applied Meteorology and Climatology*, **56 (3)**, 697–711, doi:10.1175/JAMC-D-16-0164.1, URL https://journals.ametsoc.org/view/journals/apme/56/3/jamc-d-16-0164.1.xml.

Cecil, D. J., E. J. Zipser, and S. W. Nesbitt, 2002: Reflectivity, ice scattering, and lightning characteristics of hurricane eyewalls and rainbands. part i: Quantitative description. *Monthly Weather Review*, **130 (4)**, 769 – 784, doi:10.1175/1520-0493(2002)130⟨0769:RISALC⟩2.0.CO;2.

Chen, H., and S. Gopalakrishnan, 2014: A Study on the Asymmetric Rapid Intensification of Hurricane Earl (2010) Using the HWRF System. *Journal of the Atmospheric Sciences*, **72**, doi:10.1175/JAS-D-14-0097.1.

Chen, S. S., J. A. Knaff, and F. D. Marks, 2006: Effects of Vertical Wind Shear and Storm Motion on Tropical Cyclone Rainfall Asymmetries Deduced from TRMM. *Monthly Weather Review*, **134 (11)**, 3190–3208, doi:10.1175/MWR3245.1.

Cifelli, R., V. Chandrasekar, S. Lim, P. C. Kennedy, Y. Wang, and S. A. Rutledge, 2011: A new dual-polarization radar rainfall algorithm: Application in colorado precipitation events. *Journal of Atmospheric and Oceanic Technology*, **28 (3)**, 352–364, doi:10.1175/2010JTECHA1488.1.

Clark, C. A., and P. W. Arritt, 1995: Numerical simulations of the effect of soil moisture and vegetation cover on the development of deep convection. *Journal of Applied Meteorology*, **34 (9)**, 2029–2045, doi:10.1175/1520-0450(1995)034⟨2029:NSOTEO⟩2.0.CO;2.

Corbosiero, K. L., and J. Molinari, 2002: The Effects of Vertical Wind Shear on the Distribution of Convection in Tropical Cyclones. *Monthly Weather Review*, **130 (8)**, 2110–2123, doi:10.1175/1520-0493(2002)130⟨2110:TEOVWS⟩2.0.CO;2.

Cressman, G. P., 1959: An Operational Objective Analysis System. *Monthly Weather Review*, **87 (10)**, 367–374, doi:10.1175/1520-0493(1959)087⟨0367:AOOAS⟩2.0.CO;2.

Crew, P., 2018: URL https://pyorbital.readthedocs.io/en/latest/.

Crum, T. D., and R. L. Alberty, 1993: The WSR-88D and the WSR-88D Operational Support Facility. *Bulletin of the American Meteorological Society*, **74 (9)**, 1669–1688, doi:10.1175/1520-0477(1993)074⟨1669:TWATWO⟩2.0.CO;2.

Cunha, L. K., J. A. Smith, M. L. Baeck, and W. F. Krajewski, 2013: An early performance evaluation of the nexrad dual-polarization radar rainfall estimates for urban flood applications. *Weather and Forecasting*, **28 (6)**, 1478 – 1497, doi:10.1175/WAF-D-13-00046.1, URL https://journals.ametsoc.org/view/journals/wefo/28/6/waf-d-13-00046_1.xml.

Daly, C., R. P. Neilson, and D. L. Phillips, 1994: A statistical-topographic model for mapping climatological precipitation over mountainous terrain. *Journal of Applied Meteorology*, **33 (2)**, 140–158, doi:10.1175/1520-0450(1994)033⟨0140:ASTMFM⟩2.0.CO;2.

Davis, R. S., 2001: Flash flood forecast and detection methods. *Meteorological Monographs*, **50**, 481–526, doi:10.1175/0065-9401-28.50.481.

Dawson, D., M. Biggerstaff, and S. Waugh, 2017: Purdue university portable in situ precipitation stations (pips) data. UCAR/NCAR - Earth Observing Laboratory, doi:https://doi.org/10.5065/D6GB22R5.

DeHart, J. C., and M. M. Bell, 2020: A comparison of the polarimetric radar characteristics of heavy rainfall from hurricanes harvey (2017) and florence (2018).

Journal of Geophysical Research: Atmospheres, **125 (11)**, e2019JD032 212, doi: 10.1029/2019JD032212.

DeMaria, M., 1996: The Effect of Vertical Shear on Tropical Cyclone Intensity Change. *Journal of Atmospheric Sciences*, **53 (14)**, 2076–2088, doi:10.1175/1520-0469(1996)053⟨2076:TEOVSO⟩2.0.CO;2.

DeMaria, M., J. A. Knaff, and B. H. Connell, 2001: A Tropical Cyclone Genesis Parameter for the Tropical Atlantic. *Weather and Forecasting*, **16 (2)**, 219–233, doi:10.1175/1520-0434(2001)016⟨0219:ATCGPF⟩2.0.CO;2, URL https://journals.ametsoc.org/view/journals/wefo/16/2/1520-0434_2001_016_0219_atcgpf_2_0_co_2.xml.

Didlake, A. C., and M. R. Kumjian, 2017a: Examining polarimetric radar observations of bulk microphysical structures and their relation to vortex kinematics in hurricane arthur (2014). *Monthly Weather Review*, **145 (11)**, 4521 – 4541, doi: 10.1175/MWR-D-17-0035.1.

Didlake, A. C., and M. R. Kumjian, 2017b: Examining polarimetric radar observations of bulk microphysical structures and their relation to vortex kinematics in hurricane arthur (2014). *Monthly Weather Review*, **145 (11)**, 4521–4541, doi: 10.1175/MWR-D-17-0035.1.

Didlake Jr., A. C., and M. R. Kumjian, 2018: Examining Storm Asymmetries in Hur-

ricane Irma (2017) Using Polarimetric Radar Observations. *Geophysical Research Letters*, **45 (24)**, 13,513–13,522, doi:10.1029/2018GL080739.

Duchon, C. E., C. A. Fiebrich, and B. G. Illston, 2017: Observing the May 2015 Record Rainfall at Norman, Oklahoma, Using Various Methods. *Journal of Hydrometeorology*, **18 (11)**, 3043–3049, doi:10.1175/JHM-D-17-0137.1.

Elsberry, R. L., and R. A. Jeffries, 1996: Vertical Wind Shear Influences on Tropical Cyclone Formation and Intensification during TCM-92 and TCM-93. *Monthly Weather Review*, **124 (7)**, 1374–1387, doi:10.1175/1520-0493(1996)124⟨1374:VWSIOT⟩2.0.CO;2.

Emanuel, K., J. Callaghan, and P. Otto, 2008: A hypothesis for the redevelopment of warm-core cyclones over northern australia. *Monthly Weather Review*, **136 (10)**, 3863–3872, doi:10.1175/2008MWR2409.1.

Evans, C., R. S. Schumacher, and T. J. Galarneau, 2011: Sensitivity in the overland reintensification of tropical cyclone erin (2007) to near-surface soil moisture characteristics. *Monthly Weather Review*, **139 (12)**, 3848–3870, doi:10.1175/2011MWR3593.1.

Feng, Y.-C., and M. M. Bell, 2019: Microphysical characteristics of an asymmetric eyewall in major hurricane harvey (2017). *Geophysical Research Letters*, **46 (1)**, 461–471, doi:10.1029/2018GL080770.

Fierro, A. O., E. J. Zipser, M. A. LeMone, J. M. Straka, and J. M. Simpson, 2012: Tropical oceanic hot towers: Need they be undilute to transport energy from the boundary layer to the upper troposphere effectively? an answer based on trajectory analysis of a simulation of a toga coare convective system. *Journal of the Atmospheric Sciences*, **69 (1)**, 195 – 213, doi:10.1175/JAS-D-11-0147.1.

Fovell, R. G., and H. Su, 2007: Impact of cloud microphysics on hurricane track forecasts. *Geophysical Research Letters*, **34 (24)**, doi:https://doi.org/10.1029/2007GL031723.

Franco-Díaz, A., N. Klingaman, P. Vidale, L. Guo, and M.-E. Demory, 2019: The contribution of tropical cyclones to the atmospheric branch of middle america's hydrological cycle using observed and reanalysis tracks. *Climate Dynamics*, **53**, doi:10.1007/s00382-019-04920-z.

Friedrich, K., S. Higgins, F. J. Masters, and C. R. Lopez, 2013: Articulating and Stationary PARSIVEL Disdrometer Measurements in Conditions with Strong Winds and Heavy Rainfall. *Journal of Atmospheric and Oceanic Technology*, **30 (9)**, 2063–2080, doi:10.1175/JTECH-D-12-00254.1, URL https://journals.ametsoc.org/view/journals/atot/30/9/jtech-d-12-00254_1.xml.

Giangrande, S. E., J. M. Krause, and A. Ryzhkov, 2008: Automatic designation of the melting layer with a polarimetric prototype of the wsr-88d radar. *Journal of Applied Meteorology and Climatology*, **47 (5)**, 1354 – 1364, doi:10.1175/2007JAMC1634.1.

Giangrande, S. E., and A. Ryzhkov, 2008: Estimation of rainfall based on the results of polarimetric echo classification. *Journal of Applied Meteorology and Climatology*, **47 (9)**, 2445–2462, doi:10.1175/2008JAMC1753.1.

Gorgucci, E., V. Chandrasekar, V. N. Bringi, and G. Scarchilli, 2002: Estimation of raindrop size distribution parameters from polarimetric radar measurements. *Journal of the Atmospheric Sciences*, **59 (15)**, 2373–2384, doi:10.1175/1520-0469(2002)059⟨2373:EORSDP⟩2.0.CO;2.

Gorgucci, E., G. Scarchilli, and V. Chandrasekar, 1992: Calibration of radars using polarimetric techniques. *Geoscience and Remote Sensing, IEEE Transactions on*, **30**, 853 – 858, doi:10.1109/36.175319.

Grams, H. M., J. Zhang, and K. L. Elmore, 2014: Automated identification of enhanced rainfall rates using the near-storm environment for radar precipitation estimates. *Journal of Hydrometeorology*, **15 (3)**, 1238–1254, doi:10.1175/JHM-D-13-042.1.

Gray, W., I. Cluckie, and R. Griffith, 2006: Aspects of melting and the radar bright band. *Meteorological Applications*, **8**, 371 – 379, doi:10.1017/S1350482701003139.

Gray, W. M., 1968: Global view of the origin of tropical disturbances and storms. *Monthly Weather Review*, **96 (10)**, 669 – 700, doi:10.1175/1520-0493(1968)096⟨0669:GVOTOO⟩2.0.CO;2, URL https://journals.ametsoc.org/view/journals/mwre/96/10/1520-0493_1968_096_0669_gvotoo_2_0_co_2.xml.

Griffin, E. M., T. J. Schuur, D. R. MacGorman, M. R. Kumjian, and A. O. Fierro, 2014: An electrical and polarimetric analysis of the overland reintensification of tropical storm erin (2007). *Monthly Weather Review*, **142 (6)**, 2321–2344, doi: 10.1175/MWR-D-13-00360.1.

Guo, Z., and Coauthors, 2006: Glace: The global land–atmosphere coupling experiment. part ii: Analysis. *Journal of Hydrometeorology*, **7 (4)**, 611–625, doi: 10.1175/JHM511.1.

Hamada, A., Y. N. Takayabu, C. Liu, and E. J. Zipser, 2015: Weak linkage between the heaviest rainfall and tallest storms. *Nature Communications*, **6 (1)**, 6213, doi: 10.1038/ncomms7213.

Hanley, D., J. Molinari, and D. Keyser, 2001: A Composite Study of the Interactions between Tropical Cyclones and Upper-Tropospheric Troughs. *Monthly Weather Review*, **129 (10)**, 2570–2584, doi:10.1175/1520-0493(2001)129⟨2570:ACSOTI⟩2.0.CO;2.

Hersbach, H., and Coauthors, 2019a: Global reanalysis: goodbye ERA-Interim, hello ERA5. 17–24, doi:10.21957/vf291hehd7, URL https://www.ecmwf.int/node/19027.

Hersbach, H., and Coauthors, 2019b: Global reanalysis: goodbye ERA-Interim, hello ERA5. **(159)**, 17–24, doi:10.21957/vf291hehd7, URL https://www.ecmwf.int/node/19027.

Herzegh, P. H., and A. R. Jameson, 1992: Observing precipitation through dual-polarization radar measurements. *Bulletin of the American Meteorological Society*, **73 (9)**, 1365–1376, doi:10.1175/1520-0477(1992)073⟨1365:OPTDPR⟩2.0.CO;2.

Hisham Mohd Anip, M., and P. Market, 2007: Dominant factors influencing precipitation efficiency in a continental mid-latitude location. *Tellus A*, doi:{10.3402/tellusa.v59i1.14853}.

Homeyer, C. R., and M. R. Kumjian, 2015: Microphysical characteristics of overshooting convection from polarimetric radar observations. *Journal of the Atmospheric Sciences*, **72 (2)**, 870–891, doi:10.1175/JAS-D-13-0388.1.

Homeyer, C. R., and Coauthors, 2021a: Polarimetric signatures in landfalling tropical cyclones. *Monthly Weather Review*, **149 (1)**, 131 – 154, doi:10.1175/MWR-D-20-0111.1.

Homeyer, C. R., and Coauthors, 2021b: Polarimetric Signatures in Landfalling Tropical Cyclones. *Monthly Weather Review*, **149 (1)**, 131–154, doi:10.1175/MWR-D-20-0111.1.

Hoskins, B., 2006: A potential vorticity view of synoptic development. *Meteorological Applications*, **4**, 325 – 334, doi:10.1017/S1350482797000716.

Hoskins, B. J., M. E. McIntyre, and A. W. Robertson, 1985: On the use and significance of isentropic potential vorticity maps. *Quarterly Journal of the Royal Meteorological Society*, **111 (470)**, 877–946, doi:10.1002/qj.49711147002.

Hou, A. Y., and Coauthors, 2014: The Global Precipitation Measurement Mission. *Bulletin of the American Meteorological Society*, **95 (5)**, 701–722, doi:10.1175/BAMS-D-13-00164.1.

Houze, R., 2010: Clouds in Tropical Cyclones. *Monthly Weather Review*, **138**, 293–344, doi:10.1175/2009MWR2989a.1.

Hristova-Veleva, S., and Coauthors, 2021: Impact of microphysical parameterizations on simulated hurricanes—using multi-parameter satellite data to determine the particle size distributions that produce most realistic storms. *Atmosphere*, **12 (2)**.

Huang, S. Chen, A. Zhang, and Y. Pang, 2021: Statistical Characteristics of Raindrop Size Distribution in Monsoon Season over South China Sea. *Remote Sensing*, **13 (15)**, doi:10.3390/rs13152878.

Huang, H., and F. Chen, 2019: Precipitation microphysics of tropical cyclones over the western north pacific based on gpm dpr observations: A preliminary analysis. *Journal of Geophysical Research: Atmospheres*, **124 (6)**, 3124–3142, doi:https://doi.org/10.1029/2018JD029454.

Islam Fahim, M., C. Lee, K. Mandli, and H. Takagi, 2021: A new tropical cyclone surge index incorporating the effects of coastal geometry, bathymetry and storm information. doi:10.31223/X53C85.

Jameson, A. R., 1985: Microphysical Interpretation of Multiparameter Radar Measurements in Rain. Part III: Interpretation and Measurement of Propagation Dif-

ferential Phase Shift between Orthogonal Linear Polarizations. *Journal of the Atmospheric Sciences*, **42 (6)**, 607–614, doi:10.1175/1520-0469(1985)042⟨0607:MIOMRM⟩2.0.CO;2.

Jarrell, J. D., M. Mayfield, E. N. Rappaport, and C. Landsea, 2001: The deadliest, costliest, and most intense united states hurricanes from 1900 to 2000. *NOAA Technical Memorandum*, doi:https://www.nhc.noaa.gov/pdf/NWS-TPC-2001-3.pdf.

Jessup, S. M., and A. T. DeGaetano, 2008: A Statistical Comparison of the Properties of Flash Flooding and Nonflooding Precipitation Events in Portions of New York and Pennsylvania. *Weather and Forecasting*, **23 (1)**, 114–130, doi:10.1175/2007WAF2006066.1.

Jiang, H., C. Liu, and E. Zipser, 2011: A trmm-based tropical cyclone cloud and precipitation feature database. *Journal of Applied Meteorology and Climatology*, **50**, doi:10.1175/2010JAMC2662.1.

Jorgensen, D. F., 1984: Mesoscale and Convective-Scale Characteristics of Mature Hurricanes. Part I: General Observations by Research Aircraft. *Journal of Atmospheric Sciences*, **41 (8)**, 1268–1286, doi:10.1175/1520-0469(1984)041⟨1268:MACSCO⟩2.0.CO;2.

Jorgensen, D. P., and P. T. Willis, 1982: A Z-R Relationship for Hurricanes. *Journal of Applied Meteorology and Climatology*, **21 (3)**, 356–366, doi:10.1175/1520-0450(1982)021⟨0356:AZRRFH⟩2.0.CO;2.

Kalina, E. A., K. Friedrich, S. M. Ellis, and D. W. Burgess, 2014: Comparison of disdrometer and x-band mobile radar observations in convective precipitation. *Monthly Weather Review*, **142 (7)**, 2414 – 2435, doi:10.1175/MWR-D-14-00039.1.

Kellner, O., D. Niyogi, M. Lei, and A. Kumar, 2011: The role of anomalous soil moisture on the inland reintensification of tropical storm erin (2007). *Natural Hazards*, **63**, doi:10.1007/s11069-011-9966-6.

Kimball, S. K., 2006: A Modeling Study of Hurricane Landfall in a Dry Environment. *Monthly Weather Review*, **134 (7)**, 1901–1918, doi:10.1175/MWR3155.1.

Kirstetter, P.-E., H. Andrieu, B. Boudevillain, and G. Delrieu, 2013: A physically based identification of vertical profiles of reflectivity from volume scan radar data. *Journal of Applied Meteorology and Climatology*, **52 (7)**, 1645–1663, doi:10.1175/JAMC-D-12-0228.1.

Knaff, J. A., S. A. Seseske, M. DeMaria, and J. L. Demuth, 2004: On the Influences of Vertical Wind Shear on Symmetric Tropical Cyclone Structure Derived from AMSU. *Monthly Weather Review*, **132 (10)**, 2503–2510, doi:10.1175/1520-0493(2004)132⟨2503:OTIOVW⟩2.0.CO;2.

Knapp, K. R., M. C. Kruk, D. H. Levinson, H. J. Diamond, and C. J. Neumann, 2010: The International Best Track Archive for Climate Stewardship (IBTrACS): Unifying Tropical Cyclone Data. *Bulletin of the American Meteorological Society*,

91 (3), 363–376, doi:10.1175/2009BAMS2755.1, URL https://journals.ametsoc.org/view/journals/bams/91/3/2009bams2755_1.xml.

Knapp, Kenneth R. and Diamond, Howard J. and Kossin, James P. and Kruck, Michael C. and Schreck, Carl J. III, 2018: International Best Track Archive for Climate Stewardship (IBTrACS) Project, Version 4. NOAA National Centers for Environmental Information, URL https://doi.org/10.25921/82ty-9e16.

Koster, R. D., and Coauthors, 2006: Glace: The global land–atmosphere coupling experiment. part i: Overview. *Journal of Hydrometeorology*, **7 (4)**, 590–610, doi:10.1175/JHM510.1.

Koster, R. D., and Coauthors, 2011: The second phase of the global land–atmosphere coupling experiment: Soil moisture contributions to subseasonal forecast skill. *Journal of Hydrometeorology*, **12 (5)**, 805–822, doi:10.1175/2011JHM1365.1.

Kozu, T., and Coauthors, 2001: Development of precipitation radar onboard the tropical rainfall measuring mission (trmm) satellite. *Geoscience and Remote Sensing, IEEE Transactions on*, **39**, 102 – 116, doi:10.1109/36.898669.

Kumjian, M., 2013a: Principles and Applications of Dual-Polarization Weather Radar. Part I: Description of the Polarimetric Radar Variables. *Journal of Operational Meteorology*, **1**, 226–242, doi:10.15191/nwajom.2013.0119.

Kumjian, M., 2013b: Principles and applications of dual-polarization weather radar.

part ii: Warm- and cold-season applications. *Journal of Operational Meteorology*, **1**, 243–264, doi:10.15191/nwajom.2013.0120.

Kumjian, M., and A. Ryzhkov, 2012: The impact of size sorting on the polarimetric radar variables. *Journal of the Atmospheric Sciences*.

Kumjian, M. R., and O. P. Prat, 2014: The impact of raindrop collisional processes on the polarimetric radar variables. *Journal of the Atmospheric Sciences*, **71 (8)**, 3052–3067, doi:10.1175/JAS-D-13-0357.1.

Kummerow, C., W. Barnes, T. Kozu, J. Shiue, and J. Simpson, 1998: The tropical rainfall measuring mission (trmm) sensor package. *Journal of Atmospheric and Oceanic Technology*, **15 (3)**, 809 – 817, doi:10.1175/1520-0426(1998)015⟨0809:TTRMMT⟩2.0.CO;2.

Kuo, H. L., 1965: On formation and intensification of tropical cyclones through latent heat release by cumulus convection. *Journal of Atmospheric Sciences*, **22 (1)**, 40 – 63, doi:10.1175/1520-0469(1965)022⟨0040:OFAIOT⟩2.0.CO;2, URL https://journals.ametsoc.org/view/journals/atsc/22/1/1520-0469_1965_022_0040_ofaiot_2_0_co_2.xml.

Laurencin, C. N., A. C. Didlake Jr., S. D. Loeffler, M. R. Kumjian, and G. M. Heymsfield, 2020a: Hydrometeor size sorting in the asymmetric eyewall of hurricane matthew (2016). *Journal of Geophysical Research: Atmospheres*, **125 (17)**, e2020JD032 671, doi:https://doi.org/10.1029/2020JD032671.

Laurencin, C. N., A. C. Didlake Jr., S. D. Loeffler, M. R. Kumjian, and G. M. Heymsfield, 2020b: Hydrometeor Size Sorting in the Asymmetric Eyewall of Hurricane Matthew (2016). *Journal of Geophysical Research: Atmospheres*, **125 (17)**, e2020JD032 671, doi:https://doi.org/10.1029/2020JD032671.

Lee, G., and I. Zawadzki, 2006: Radar calibration by gage, disdrometer, and polarimetry: Theoretical limit caused by the variability of drop size distribution and application to fast scanning operational radar data. *Journal of Hydrology*, **328**, 83–97, doi:10.1016/j.jhydrol.2005.11.046.

Liao, L., and R. Meneghini, 2019: Physical Evaluation of GPM DPR Single- and Dual-Wavelength Algorithms. *Journal of Atmospheric and Oceanic Technology*, **36 (5)**, 883–902, doi:10.1175/JTECH-D-18-0210.1.

Liao, L., R. Meneghini, and A. Tokay, 2014: Uncertainties of gpm dpr rain estimates caused by dsd parameterizations. *Journal of Applied Meteorology and Climatology*, **53 (11)**, 2524 – 2537, doi:10.1175/JAMC-D-14-0003.1.

List, R., N. R. Donaldson, and R. E. Stewart, 1987: Temporal evolution of drop spectra to collisional equilibrium in steady and pulsating rain. *Journal of Atmospheric Sciences*, **44 (2)**, 362 – 372, doi:10.1175/1520-0469(1987)044⟨0362:TEODST⟩2.0.CO;2.

List, R., and E. P. Lozowski, 1970: Pressure perturbations and buoyancy in

convective clouds. *Journal of the Atmospheric Sciences*, **27 (1)**, 168–170, doi: 10.1175/1520-0469(1970)027⟨0168:PPABIC⟩2.0.CO;2.

Loney, M. L., D. S. Zrnić, J. M. Straka, and A. V. Ryzhkov, 2002: Enhanced polarimetric radar signatures above the melting level in a supercell storm. *Journal of Applied Meteorology*, **41 (12)**, 1179–1194, doi:10.1175/1520-0450(2002)041⟨1179: EPRSAT⟩2.0.CO;2.

Lonfat, M., F. D. Marks, and S. S. Chen, 2004: Precipitation Distribution in Tropical Cyclones Using the Tropical Rainfall Measuring Mission (TRMM) Microwave Imager: A Global Perspective. *Monthly Weather Review*, **132 (7)**, 1645–1660, doi: 10.1175/1520-0493(2004)132⟨1645:PDITCU⟩2.0.CO;2.

Lynn, B. H., W.-K. Tao, and P. J. Wetzel, 1998: A study of landscape-generated deep moist convection. *Monthly Weather Review*, **126 (4)**, 928–942, doi:10.1175/ 1520-0493(1998)126⟨0928:ASOLGD⟩2.0.CO;2.

Marks, F., and R. Houze, 1987: Inner Core Structure of Hurricane Alicia from Airborne Doppler Radar Observations. *Journal of The Atmospheric Sciences - J ATMOS SCI*, **44**, 1296–1317, doi:10.1175/1520-0469(1987)044⟨1296:ICSOHA⟩2.0.CO; 2.

Marks, F. D., and R. A. Houze, 1984: Airborne Doppler Radar Observations in Hurricane Debby. *Bulletin of the American Meteorological Society*, **65 (6)**, 569–582, doi:10.1175/1520-0477(1984)065⟨0569:ADROIH⟩2.0.CO;2.

Marra, A. C., and Coauthors, 2019: The precipitation structure of the mediterranean tropical-like cyclone numa: Analysis of gpm observations and numerical weather prediction model simulations. *Remote Sensing*, **11 (14)**, doi:10.3390/rs11141690.

Martinaitis, S. M., S. B. Cocks, A. P. Osborne, M. J. Simpson, L. Tang, J. Zhang, and K. W. Howard, 2021: The Historic Rainfalls of Hurricanes Harvey and Florence: A Perspective from the Multi-Radar Multi-Sensor System. *Journal of Hydrometeorology*, **22 (3)**, 721–738, doi:10.1175/JHM-D-20-0199.1.

Martner, B. E., 1977: A field experiment on the calibration of radars with raindrop disdrometers. *Journal of Applied Meteorology (1962-1982)*, **16 (4)**, 451–454.

May, R., S. Arms, P. Marsh, E. Bruning, and J. Leeman, 2008 - 2017: Metpy: A Python package for meteorological data. Boulder, Colorado, doi:10.5065/D6WW7G29.

McFarquhar, G. M., and R. A. Black, 2004: Observations of particle size and phase in tropical cyclones: Implications for mesoscale modeling of microphysical processes. *Journal of the Atmospheric Sciences*, **61 (4)**, 422 – 439, doi:10.1175/1520-0469(2004)061⟨0422:OOPSAP⟩2.0.CO;2.

McFarquhar, G. M., H. Zhang, G. Heymsfield, J. B. Halverson, R. Hood, J. Dudhia, and F. Marks, 2006: Factors Affecting the Evolution of Hurricane Erin (2001) and the Distributions of Hydrometeors: Role of Microphysical Processes. *Journal of*

the Atmospheric Sciences, **63 (1)**, 127–150, doi:10.1175/JAS3590.1, URL https://journals.ametsoc.org/view/journals/atsc/63/1/jas3590.1.xml.

McGee, C. J., and S. C. van den Heever, 2014: Latent heating and mixing due to entrainment in tropical deep convection. *Journal of the Atmospheric Sciences*, **71 (2)**, 816 – 832, doi:10.1175/JAS-D-13-0140.1.

McPherson, R. A., and Coauthors, 2007: Statewide Monitoring of the Mesoscale Environment: A Technical Update on the Oklahoma Mesonet. *Journal of Atmospheric and Oceanic Technology*, **24 (3)**, 301–321, doi:10.1175/JTECH1976.1.

Medlin, J. M., S. K. Kimball, and K. G. Blackwell, 2007: Radar and rain gauge analysis of the extreme rainfall during hurricane danny's (1997) landfall. *Monthly Weather Review*, **135 (5)**, 1869–1888, doi:10.1175/MWR3368.1.

Meneghini, R., H. Kim, L. Liao, J. A. Jones, and J. M. Kwiatkowski, 2015: An Initial Assessment of the Surface Reference Technique Applied to Data from the Dual-Frequency Precipitation Radar (DPR) on the GPM Satellite. *Journal of Atmospheric and Oceanic Technology*, **32 (12)**, 2281–2296, doi:10.1175/JTECH-D-15-0044.1.

Merceret, F. J., 1974: On the size distribution of raindrops in hurricane ginger. *Monthly Weather Review*, **102 (10)**, 714 – 716, doi:10.1175/1520-0493(1974)102⟨0714:OTSDOR⟩2.0.CO;2.

Monteverdi, J., and R. Edwards, 2010: The redevelopment of a warm core structure in erin: A case of inland tropical storm formation. *Electronic Journal of Severe Storms Meteorology*, **5**, 1–18.

Mori, N., M. Kato, S. Kim, H. Mase, Y. Shibutani, T. Takemi, K. Tsuboki, and T. Yasuda, 2014: Local amplification of storm surge by super typhoon haiyan in leyte gulf. *Geophysical Research Letters*, **41 (14)**, 5106–5113, doi:https://doi.org/10.1002/2014GL060689.

Murphy, A. M., A. Ryzhkov, and P. Zhang, 2020: Columnar Vertical Profile (CVP) Methodology for Validating Polarimetric Radar Retrievals in Ice Using In Situ Aircraft Measurements. *Journal of Atmospheric and Oceanic Technology*, **37 (9)**, 1623–1642, doi:10.1175/JTECH-D-20-0011.1.

Möller, J. D., and M. T. Montgomery, 2000: Tropical cyclone evolution via potential vorticity anomalies in a three-dimensional balance model. *Journal of the Atmospheric Sciences*, **57 (20)**, 3366–3387, doi:10.1175/1520-0469(2000)057⟨3366:TCEVPV⟩2.0.CO;2.

Möller, J. D., and R. K. Smith, 1994: The development of potential vorticity in a hurricane-like vortex. *Quarterly Journal of the Royal Meteorological Society*, **120 (519)**, 1255–1265, doi:10.1002/qj.49712051907.

Nair, U., and Coauthors, 2019: Influence of land cover and soil moisture based brown

ocean effect on an extreme rainfall event from a louisiana gulf coast tropical system. *Scientific Reports*, **9**, 17 136, doi:10.1038/s41598-019-53031-6.

National Hurricane Center, 2021: National Hurricane Center Tropical Cyclone Report: Hurricane Laura. National Hurricane Center, URL https://www.nhc.noaa.gov/data/tcr/AL132020_Laura.pdf.

NOAA National Weather Service (NWS) Radar Operations Center, 1991: NOAA Next Generation Radar (NEXRAD) Level 2 Base Data. NOAA National Centers for Environmental Information, doi:doi:10.7289/V5W9574V.

Park, S.-G., H.-L. Kim, Y.-W. Ham, and S.-H. Jung, 2017: Comparative evaluation of the ott parsivel2 using a collocated two-dimensional video disdrometer. *Journal of Atmospheric and Oceanic Technology*, **34 (9)**, 2059 – 2082, doi:10.1175/JTECH-D-16-0256.1.

Pillay, M. T., and J. M. Fitchett, 2021: Southern hemisphere tropical cyclones: A critical analysis of regional characteristics. *International Journal of Climatology*, **41 (1)**, 146–161, doi:https://doi.org/10.1002/joc.6613.

Porcacchia, L., P.-E. Kirstetter, V. Maggioni, and S. Tanelli, 2019: Investigating the gpm dual-frequency precipitation radar signatures of low-level precipitation enhancement. *Quarterly Journal of the Royal Meteorological Society*, **145 (724)**, 3161–3174, doi:https://doi.org/10.1002/qj.3611.

Radhakrishna, B., S. K. Satheesh, T. Narayana Rao, K. Saikranthi, and K. Sunilkumar, 2016: Assessment of dsds of gpm-dpr with ground-based disdrometer at seasonal scale over gadanki, india. *Journal of Geophysical Research: Atmospheres*, **121 (19)**, 11,792–11,802, doi:https://doi.org/10.1002/2015JD024628.

Rappaport, E., 2014: Fatalities in the united states from atlantic tropical cyclones: New data and interpretation. *Bulletin of the American Meteorological Society*, **95**, 341–346, doi:10.1175/BAMS-D-12-00074.1.

Rappaport, E. N., 2000: Loss of life in the united states associated with recent atlantic tropical cyclones. *Bulletin of the American Meteorological Society*, **81 (9)**, 2065–2074, doi:10.1175/1520-0477(2000)081⟨2065:LOLITU⟩2.3.CO;2.

Ryzhkov, A., 2007: The impact of beam broadening on the quality of radar polarimetric data. *Journal of Atmospheric and Oceanic Technology*, **24 (5)**, 729–744, doi:10.1175/JTECH2003.1.

Ryzhkov, A., S. E. Giangrande, V. M. Melnikov, and T. J. Schuur, 2005a: Calibration Issues of Dual-Polarization Radar Measurements. *Journal of Atmospheric and Oceanic Technology*, **22 (8)**, 1138–1155, doi:10.1175/JTECH1772.1, URL https://journals.ametsoc.org/view/journals/atot/22/8/jtech1772_1.xml.

Ryzhkov, A., S. E. Giangrande, and T. J. Schuur, 2005b: Rainfall estimation with a polarimetric prototype of wsr-88d. *Journal of Applied Meteorology*, **44 (4)**, 502–515, doi:10.1175/JAM2213.1.

Ryzhkov, A., T. J. Schuur, D. W. Burgess, P. L. Heinselman, S. E. Giangrande, and D. S. Zrnic, 2005c: The joint polarization experiment: Polarimetric rainfall measurements and hydrometeor classification. *Bulletin of the American Meteorological Society*, **86 (6)**, 809–824, doi:10.1175/BAMS-86-6-809.

Ryzhkov, A., P. Zhang, H. Reeves, M. Kumjian, T. Tschallener, S. Trömel, and C. Simmer, 2016: Quasi-vertical profiles—a new way to look at polarimetric radar data. *Journal of Atmospheric and Oceanic Technology*, **33 (3)**, 551–562, doi:10.1175/JTECH-D-15-0020.1.

Sanchez-Rivas, D., and M. Rico-Ramirez, 2021: Calibration of radar differential reflectivity using quasi-vertical profiles. *Atmospheric Measurement Techniques*, doi:10.5194/amt-2021-194.

Schroeder, A., J. Basara, J. M. Shepherd, and S. Nelson, 2016: Insights into Atmospheric Contributors to Urban Flash Flooding across the United States Using an Analysis of Rawinsonde Data and Associated Calculated Parameters. *Journal of Applied Meteorology and Climatology*, **55 (2)**, 313–323, doi:10.1175/JAMC-D-14-0232.1.

Science Applications International Corporation and National Hurricane Center, 1993: Global Tropical Cyclone "Best Track" Position and Intensity Data. Research Data Archive at the National Center for Atmospheric Research, Computational and In-

formation Systems Laboratory, Boulder CO, URL http://rda.ucar.edu/datasets/ds824.1/.

Seliga, T. A., and V. N. Bringi, 1976: Potential use of radar differential reflectivity measurements at orthogonal polarizations for measuring precipitation. *Journal of Applied Meteorology*, **15 (1)**, 69–76, doi:10.1175/1520-0450(1976)015⟨0069:PUORDR⟩2.0.CO;2.

Seliga, T. A., and V. N. Bringi, 1978: Differential reflectivity and differential phase shift: Applications in radar meteorology. *Radio Science*, **13 (2)**, 271–275, doi:10.1029/RS013i002p00271.

Sheppard, B. E., and P. I. Joe, 1994: Comparison of raindrop size distribution measurements by a joss-waldvogel disdrometer, a pms 2dg spectrometer, and a poss doppler radar. *Journal of Atmospheric and Oceanic Technology*, **11 (4)**, 874 – 887, doi:10.1175/1520-0426(1994)011⟨0874:CORSDM⟩2.0.CO;2.

Simpson, J., C. Kummerow, W. K. Tao, and R. F. Adler, 1996: On the Tropical Rainfall Measuring Mission (TRMM). *Meteorology and Atmospheric Physics*, **60 (1)**, 19–36, doi:10.1007/BF01029783.

Skofronick-Jackson, G., and Coauthors, 2017: The Global Precipitation Measurement (GPM) Mission for Science and Society. *Bulletin of the American Meteorological Society*, **98 (8)**, 1679–1695, doi:10.1175/BAMS-D-15-00306.1.

Smalley, M., P.-E. Kirstetter, and T. L'Ecuyer, 2017: How frequent is precipitation over the contiguous united states? perspectives from ground-based and spaceborne radars. *Journal of Hydrometeorology*, **18 (6)**, 1657–1672, doi:10.1175/JHM-D-16-0242.1.

Smith, M., and R. Toumi, 2020: A dipole of tropical cyclone outgoing long-wave radiation. *Quarterly Journal of the Royal Meteorological Society*, **147 (734)**, 166–180, doi:https://doi.org/10.1002/qj.3912.

Smith, P. L., 2003: Raindrop size distributions: Exponential or gamma—does the difference matter? *Journal of Applied Meteorology*, **42 (7)**, 1031 – 1034, doi:10.1175/1520-0450(2003)042⟨1031:RSDEOG⟩2.0.CO;2.

Song, F., and G. J. Zhang, 2016: Effects of Southeastern Pacific Sea Surface Temperature on the Double-ITCZ Bias in NCAR CESM1. *Journal of Climate*, **29 (20)**, 7417–7433, doi:10.1175/JCLI-D-15-0852.1, URL https://journals.ametsoc.org/view/journals/clim/29/20/jcli-d-15-0852.1.xml.

Speirs, P., M. Gabella, and A. Berne, 2017: A Comparison between the GPM Dual-Frequency Precipitation Radar and Ground-Based Radar Precipitation Rate Estimates in the Swiss Alps and Plateau. *Journal of Hydrometeorology*, **18 (5)**, 1247–1269, doi:10.1175/JHM-D-16-0085.1.

Squires, P., 1956: The Micro-Structure of Cumuli in Maritime and Continental Air. *Tellus*, **8 (4)**, 443.

Straka, J. M., D. S. Zrnić, and A. Ryzhkov, 2000: Bulk hydrometeor classification and quantification using polarimetric radar data: Synthesis of relations. *Journal of Applied Meteorology*, **39 (8)**, 1341 – 1372, doi:10.1175/1520-0450(2000)039⟨1341:BHCAQU⟩2.0.CO;2, URL https://journals.ametsoc.org/view/journals/apme/39/8/1520-0450_2000_039_1341_bhcaqu_2.0.co_2.xml.

Testud, J., E. Le Bouar, E. Obligis, and M. Ali-Mehenni, 2000: The rain profiling algorithm applied to polarimetric weather radar. *Journal of Atmospheric and Oceanic Technology*, **17 (3)**, 332–356, doi:10.1175/1520-0426(2000)017⟨0332:TRPAAT⟩2.0.CO;2.

Tokay, A., P. G. Bashor, E. Habib, and T. Kasparis, 2008: Raindrop size distribution measurements in tropical cyclones. *Monthly Weather Review*, **136 (5)**, 1669 – 1685, doi:10.1175/2007MWR2122.1.

Tokay, A., W. A. Petersen, P. Gatlin, and M. Wingo, 2013: Comparison of raindrop size distribution measurements by collocated disdrometers. *Journal of Atmospheric and Oceanic Technology*, **30 (8)**, 1672 – 1690, doi:10.1175/JTECH-D-12-00163.1.

Tokay, A., and D. A. Short, 1996: Evidence from Tropical Raindrop Spectra of the Origin of Rain from Stratiform versus Convective Clouds. *Journal of Applied Meteorology and Climatology*, **35 (3)**, 355–371, doi:10.1175/1520-0450(1996)035⟨0355:EFTRSO⟩2.0.CO;2, URL https://journals.ametsoc.org/view/journals/apme/35/3/1520-0450_1996_035_0355_eftrso_2_0_co_2.xml.

Trenberth, K. E., and J. Fasullo, 2007: Water and energy budgets of hurricanes and implications for climate change. *Journal of Geophysical Research: Atmospheres*, **112 (D23)**, doi:10.1029/2006JD008304.

Ulbrich, C., and D. Atlas, 2007: Microphysics of raindrop size spectra: Tropical continental and maritime storms. *Journal of Applied Meteorology and Climatology - J APPL METEOROL CLIMATOL*, **46**, 1777–1791, doi:10.1175/2007JAMC1649.1.

Ulbrich, C. W., and L. G. Lee, 2002: Rainfall characteristics associated with the remnants of tropical storm helene in upstate south carolina. *Weather and Forecasting*, **17 (6)**, 1257 – 1267, doi:10.1175/1520-0434(2002)017⟨1257:RCAWTR⟩2.0.CO;2.

Vitale, J., and T. Ryan, 2013: Operational recognition of high precipitation efficiency and low-echo-centroid convection. *Journal of Operational Meteorology*, **1**, 128–143, doi:10.15191/nwajom.2013.0112.

Vivekanandan, J., W. M. Adams, and V. N. Bringi, 1991: Rigorous Approach to Polarimetric Radar Modeling of Hydrometeor Orientation Distributions. *Journal of Applied Meteorology and Climatology*, **30 (8)**, 1053–1063, doi:10.1175/1520-0450(1991)030⟨1053:RATPRM⟩2.0.CO;2.

Wakefield, R. A., J. B. Basara, J. M. Shepherd, N. Brauer, J. C. Furtado, J. A. S. Jr., and R. Edwards, 2021: The Inland Maintenance and Reintensification of Tropical Storm Bill (2015). Part I: Contributions of the Brown Ocean Effect. *Journal of Hydrometeorology*, **22 (10)**, 2675–2693, doi:10.1175/JHM-D-20-0150.1.

Wang, Y., and V. Chandrasekar, 2009: Algorithm for Estimation of the Specific Differential Phase. *Journal of Atmospheric and Oceanic Technology*, **26 (12)**, 2565–2578, doi:10.1175/2009JTECHA1358.1.

Warren, R. A., A. Protat, S. T. Siems, H. A. Ramsay, V. Louf, M. J. Manton, and T. A. Kane, 2018: Calibrating ground-based radars against trmm and gpm. *Journal of Atmospheric and Oceanic Technology*.

Weatherford, C. L., and W. M. Gray, 1988: Typhoon Structure as Revealed by Aircraft Reconnaissance. Part I: Data Analysis and Climatology. *Monthly Weather Review*, **116 (5)**, 1032–1043, doi:10.1175/1520-0493(1988)116⟨1032:TSARBA⟩2.0.CO;2.

Wei, J., H. Su, and Z.-L. Yang, 2015: Impact of moisture flux convergence and soil moisture on precipitation: A case study for the southern united states with implications for the globe. *Climate Dynamics*, **46**, doi:10.1007/s00382-015-2593-2.

Wilson, J. W., and D. M. Pollock, 1974: Rainfall measurements during hurricane agnes by three overlapping radars. *Journal of Applied Meteorology and Climatology*, **13 (8)**, 835 – 844, doi:10.1175/1520-0450(1974)013⟨0835:RMDHAB⟩2.0.CO;2.

Wingo, M. T., and D. J. Cecil, 2010: Effects of Vertical Wind Shear on Tropical Cyclone Precipitation. *Monthly Weather Review*, **138 (3)**, 645–662, doi:10.1175/2009MWR2921.1.

Wu, L., H. Su, R. G. Fovell, T. J. Dunkerton, Z. Wang, and B. H. Kahn, 2015: Impact of environmental moisture on tropical cyclone intensification. *Atmospheric Chemistry and Physics*, **15 (24)**, 14 041–14 053, doi:10.5194/acp-15-14041-2015.

Wu, Z., Y. Zhang, L. Zhang, X. Hao, H. Lei, and H. Zheng, 2019: Validation of gpm precipitation products by comparison with ground-based parsivel disdrometers over jianghuai region. *Water*, **11 (6)**, doi:10.3390/w11061260.

Xu, X., K. Howard, and J. Zhang, 2008: An automated radar technique for the identification of tropical precipitation. *Journal of Hydrometeorology*, **9 (5)**, 885–902, doi:10.1175/2007JHM954.1.

Yoo, J., J. A. Santanello, M. Shepherd, S. Kumar, P. Lawston, and A. M. Thomas, 2020: Quantification of the land surface and brown ocean influence on tropical cyclone intensification over land. *Journal of Hydrometeorology*, **21 (6)**, 1171–1192, doi:10.1175/JHM-D-19-0214.1.

You, C., M. Kang, and D.-I. Lee, 2019: Rainfall estimates with respect to rainfall types using s-band polarimetric radar in korea. *Atmosphere*, **10 (12)**, doi:10.3390/atmos10120773.

Zhang, P., D. Zrnić, and A. Ryzhkov, 2013: Partial beam blockage correction using polarimetric radar measurements. *Journal of Atmospheric and Oceanic Technology*, **30 (5)**, 861–872, doi:10.1175/JTECH-D-12-00075.1.

Zheng, H., Y. Zhang, L. Zhang, H. Lei, and Z. Wu, 2021: Precipitation Microphysical Processes in the Inner Rainband of Tropical Cyclone Kajiki (2019) over the South China Sea Revealed by Polarimetric Radar. *Advances in Atmospheric Sciences*, **38 (1)**, 65–80, doi:10.1007/s00376-020-0179-3, URL https://doi.org/10.1007/s00376-020-0179-3.

Zrnic, D. S., and A. Ryzhkov, 1999: Polarimetry for weather surveillance radars. *Bulletin of the American Meteorological Society*, **80 (3)**, 389–406, doi:10.1175/1520-0477(1999)080⟨0389:PFWSR⟩2.0.CO;2.

Zrnić, D. S., and A. Ryzhkov, 1996: Advantages of rain measurements using specific differential phase. *Journal of Atmospheric and Oceanic Technology*, **13 (2)**, 454–464, doi:10.1175/1520-0426(1996)013⟨0454:AORMUS⟩2.0.CO;2.